

Low-Energy Photoemission Study on the Effects of Electron Doping on the Kondo Insulator YbB_{12}

A. Rousuli¹, H. Sato², M. Arita², F. Iga³, K. Shimada² and H. Namatame²

¹Graduate School of Science, Hiroshima University, Higashi-Hiroshima 739-8526, Japan

²Hiroshima Synchrotron Radiation Center, Hiroshima University, Higashi-Hiroshima 739-0046, Japan

³Faculty of Science, Ibaraki University, Mito 310-8512, Japan

Keywords: Kondo insulator, energy gap

The Kondo insulators of f -electron compounds have attracted considerable attention in recent years. They behave as metallic systems at high temperatures and non-magnetic insulators at low temperatures. The origin of the insulating gap is still controversial. YbB_{12} is well known as the Kondo insulator with a narrow gap of ~ 10 meV and many theoretical and experimental studies are performed on its electronic structure. Recently, Hayashi *et al.* have successfully synthesized $\text{Yb}_{1-x}\text{Zr}_x\text{B}_{12}$ compounds whose electronic structure is significantly changed by the Zr substitution [1]. Magnetic susceptibility measurement of $\text{Yb}_{1-x}\text{Zr}_x\text{B}_{12}$ shows a typical valence fluctuation behavior with the Pauli paramagnetic ground state. A broad maximum of magnetic susceptibility of YbB_{12} is observed around 80 K and it moves up to about 220 K by $x = 0.875$ of Zr concentration. Recently, we have investigated the electronic structure of $\text{Yb}_{1-x}\text{Zr}_x\text{B}_{12}$ by means of hard x-ray photoemission spectroscopy with $h\nu = 5.95$ keV [2]. With increasing the Zr concentration, the Yb valence gets close to divalent state and the B $1s$ and Zr $3d$ peaks are shifted to the deeper binding energy. These results suggest that supplied electrons from Zr^{4+} go both into the Yb $4f$ and conduction bands. In this study, we have examined the electronic structure in the vicinity of the Fermi energy (E_F) of $\text{Yb}_{1-x}\text{Zr}_x\text{B}_{12}$ by means of low-energy photoemission spectroscopy (LEPES) using the Xe discharge lamp ($h\nu = 8.44$ eV) at BL-9A at HiSOR.

Figure 1 (a) shows the LEPES spectra near E_F of YbB_{12} measured between 6 and 210 K. The crossing point is not located at below E_F , which is a signature of the gap formation. With decreasing temperature, three characteristic structures shows up at 15 (peak "A"), 30 (peak "B") and 45 meV (peak "C"). The spectral feature is consistent with the previous result of laser PES [3]. According to Ref. 3, the sharp peak "A" and the broad peak "C" are ascribed to the renormalized hybridization band between Yb $4f$ and conduction electrons ($c-f$ hybridization band) and the Yb $4f_{7/2}$ states, so called the Kondo peak, respectively. The peak "B" would appear as a result of the crystal splitting effect [4].

Figure 1 (b) shows the LEPES spectra near E_F of $\text{Yb}_{1-x}\text{Zr}_x\text{B}_{12}$ ($x = 0.25$). The basic spectral feature is similar to that of YbB_{12} in Fig. 1 (a) with respect to the three structures. However, the intensities become weak in whole. In addition, the peak "A" is shifted toward E_F and the peak "C" is shifted to opposite side. With increasing the Zr concentration, the intensities of the three peaks gradually become weak and the peak "C" continues to be shifted to the deeper binding energy. Since the energy position of the peak "C" reflects the Kondo temperature (T_K), the energy shift of the peak "C" suggests the increase of the $c-f$ hybridization with the Zr concentration. This result is consistent with the magnetic susceptibility measurements [1], where the maximal temperature of the susceptibility increase with the Zr concentration and it is scaled with T_K . The spectral features are almost metallic for $x > 0.625$ with the weak and broad peak "C".

Figure 2 (a) shows the spectral density of states (DOS) of YbB_{12} derived by dividing the LEPES spectra in Fig. 1 by the Fermi-Dirac distribution function. With decreasing temperature, DOS around E_F is reduced, which shows that the energy gap develops. The DOS curve crosses around 10 meV (indicated with " Δ " in the figure) and we tentatively assume that the energy position reflects the energy gap size. We found that the " Δ " is shifted to the binding energy side with the Zr concentration up to $x = 0.5$ (see Fig. 2 (b) in case of $x = 0.25$). That is, the gap size becomes larger with the Zr concentration, which seems to be consistent with the result of the specific heat measurements for $x = 0.1$ [1]. The signature of " Δ " disappears for $x > 0.5$ and the system is metallic.

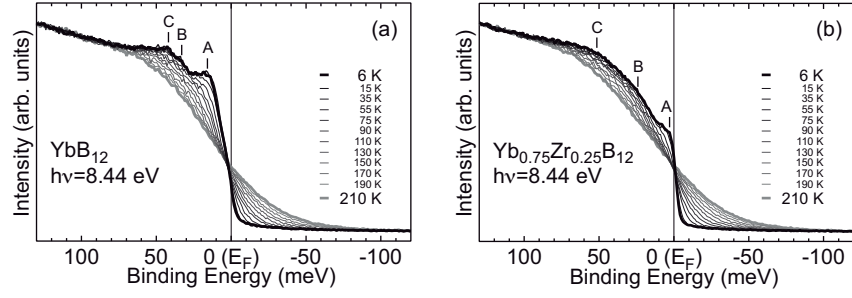


FIGURE 1. Temperature dependences of LEPES spectra near E_F of (a) YbB_{12} and (b) $\text{Yb}_{0.75}\text{Zr}_{0.25}\text{B}_{12}$ measured between 6 and 210 K.

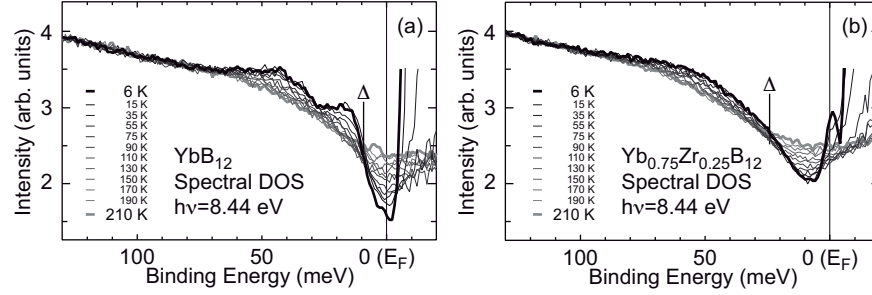


FIGURE 2. Temperature dependences of spectral DOS's near E_F of (a) YbB_{12} and (b) $\text{Yb}_{0.75}\text{Zr}_{0.25}\text{B}_{12}$ derived from the LEPES spectra in Fig. 1.

REFERENCES

1. K. Hayashi *et al.*, JPS Conf. Proc. **3**, 011050 (2014).
2. A. Rousuli *et al.*, J. Phys.: Condens. Matter **29**, 265601 (2017).
3. M. Okawa *et al.*, Phys. Rev. B **92**, 161108(R) (2015).
4. P. A. Alekzееv, *et al.*, J. Phys.: Condens. Matter **16**, 2631 (2004).

Discovery of 2D Anisotropic Dirac cones in borophene

B. Feng^a, J. Zhang^b, S. Ito^c, M. Arita^a, C. Cheng^b, L. Chen^b, K. Wu^b, F. Komori^c,
O. Sugino^c, K. Miyamoto^a, T. Okuda^a, S. Meng^b, and I. Matsuda^a

^a Hiroshima Synchrotron Radiation Center, Hiroshima University, 2-313 Kagamiyama, Higashi-Hiroshima
739-0046, Japan

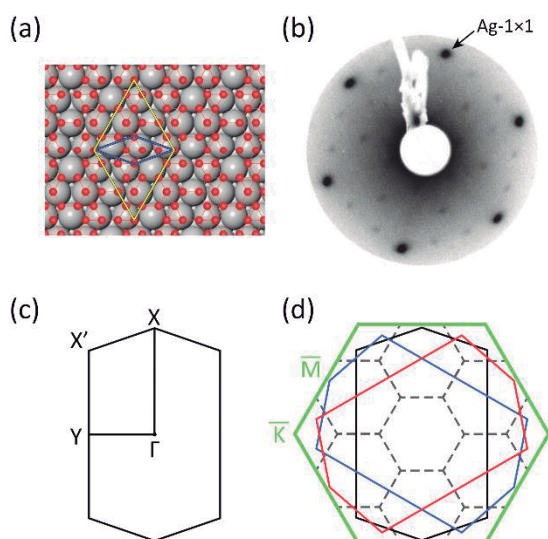
^b Institute of Physics, Chinese Academy of Sciences, Beijing, 100190, China

^c Institute for Solid State Physics, The University of Tokyo, Kashiwa, Chiba, 277-8581, Japan

Keywords: Borophene, Anisotropic, Dirac cone, ARPES

Low energy electronic excitations in some quantum materials can behave as fundamental fermions in nature: i.e., Dirac, Majorana, and Weyl fermions. In Dirac materials, such as graphene and Dirac semimetals, there exist gapless Dirac cones near the Fermi level with linear energy momentum dispersion near the Dirac points. Although Dirac cones are typically isotropic, anisotropic Dirac cones have been recently discovered in several materials, such as BaFe₂As₂ and Sr(Ca)MnBi₂. The anisotropy of the Dirac cones could result in anisotropic carrier mobility, making it possible to realize direction-dependent quantum devices. To date, most of the experimentally discovered Dirac materials are 3D, while 2D Dirac materials remain quite rare. Among the hundreds of 2D materials that have been discovered, only graphene, silicene, and β_{12} borophene have been experimentally confirmed to host Dirac cones. Although 2D anisotropic Dirac cones have attracted great theoretical attention, experimental discoveries of such materials have been limited.

As the fifth element in the periodic table, boron is known to have a rich chemistry and is able to form numerous bulk allotropes. Boron 2D sheets, namely, borophene, also have an enormous number of polymorphs, which can be considered to be triangular lattices with periodic vacancies. Recently, several borophene phases have been synthesized on Ag(111) and Ag(110), such as β_{12} sheets ($\eta = 1/6$), χ_3 sheets ($\eta = 1/5$), and α ($\eta = 1/9$) sheets. Moreover, a possible free-standing borophene structure has been synthesized by deintercalation of Mg in MgB₂ single crystals, which enables the possibility of boron-based devices. Further theoretical works have revealed numerous novel properties of these borophene phases, such as phonon-mediated superconductivity, excellent mechanical properties, and high-performance in capacitive energy storage. However, despite the rapid progress on the synthesis of borophene, experimental studies of their electronic structures are still lacking.



Here, we report the observation of 2D anisotropic Dirac cones in χ_3 borophene using combined angle-resolved photoemission spectroscopy (ARPES) measurements and first-principles calculations. The Dirac cones are centered at the X and X' points of the Brillouin zone (BZ). Along some directions, the Fermi velocity is as high as that in graphene. Our results also reveal that these Dirac cones are mainly derived from the p_z orbitals of boron, with negligible contributions from the silver orbitals. Compared with the β_{12} phase, the χ_3 phase has a weaker substrate-overlayer hybridization, and thus represents a quasi-freestanding borophene sheet. Our results validate χ_3 borophene as the first 2D material that hosts anisotropic Dirac cones, which may stimulate further research interest and enable the realization of high-performance boron devices.

FIGURE 1. (a) Structure model of χ_3 borophene on Ag(111). Red and gray balls represent boron and silver atoms, respectively. Blue and yellow rhombuses indicate unit cells of borophene and the superstructure. (b) A LEED pattern of the χ_3 borophene on Ag(111), which shows a 3×3 superstructure with respect to Ag(111)- 1×1 . The beam energy during the measurement was 116 eV. (c) Schematic drawing of the BZ of the χ_3 borophene. (d) BZs of the χ_3 borophene (black, blue, and red lines), Ag(111) (green lines), and the superstructure (black dashed lines).

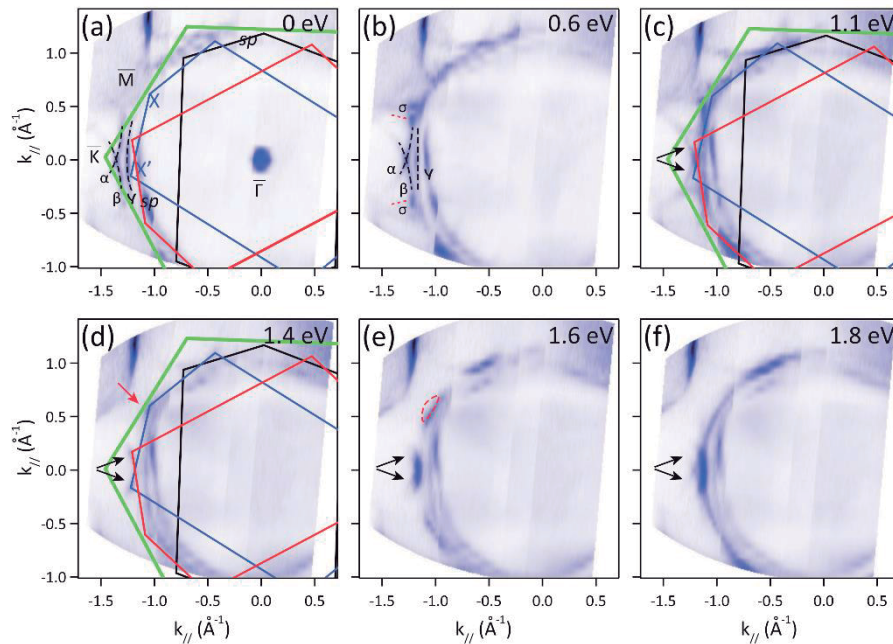


FIGURE 2. Constant energy contours of borophene on Ag(111) measured with 21 eV photons. (a–f) The binding energies are 0, 0.6, 1.1, 1.4, 1.6, and 1.8 eV, respectively. Black and red dashed lines in (a) and (b) indicate the surface bands near the K point of Ag(111). The black and red arrows indicate the Dirac cones at the X' and X points of borophene.

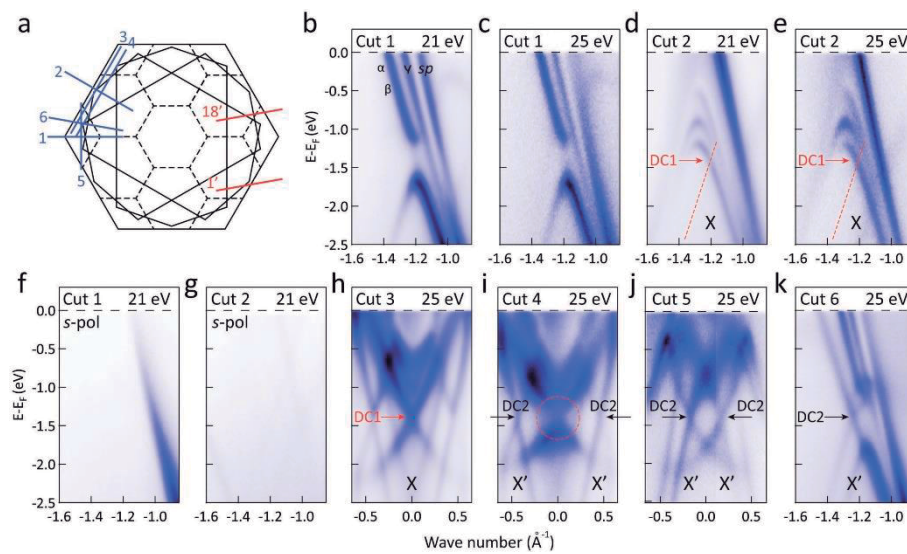


FIGURE 3. (a) Schematic drawing of the momentum cuts measured in this figure. (b,c) ARPES intensity plots measured along cut 1 with 21 and 25 eV p polarized photons, respectively. (d,e) ARPES intensity plots measured along cut 2 with 21 and 25 eV p polarized photons, respectively. (f,g) ARPES intensity plots measured along cut 1 and cut 2 with s polarized light. (h–k) ARPES intensity plots measured along cuts 3–6 with p polarized light. Red and black arrows indicate the Dirac cones at the X and X' points (DC1 and DC2).

REFERENCES

1. B. Feng, *et al.* Discovery of 2D anisotropic Dirac cones. *Adv. Mater.* **30**, 1704025 (2018).
2. B. Feng, *et al.* Experimental realization of two-dimensional boron sheets. *Chem.* **8**, 563 (2016).
3. B. Feng, *et al.* Dirac fermions in borophene. *Phys. Rev. Lett.* **118**, 096401 (2017).

SARPES study on IrTe₂

T. Mizokawa^a, Y. Okamoto^a, S. Iwasaki^a, K. Takubo^b,
H. Ishii^c, K. Kudo^c, M. Nohara^c, K. Miyamoto^d, T. Okuda^d

^a *Department of Applied Physics, Waseda University, Shinjuku-ku, Tokyo 169-8555, Japan*

^b *Institute for Solid State Physics, University of Tokyo, Chiba 277-8581, Japan*

^c *Department of Physics, Tokyo Metropolitan University, Hachioji 192-0397, Japan*

^d *HiSOR, Hiroshima University, Higashihiroshima, Hiroshima 739-0046, Japan*

Keywords: IrTe₂, spin-orbit interaction, orbital order

After the discovery of IrTe₂-based superconductor by Pyon, Kudo, Nohara [1] and Yang et al. [2], extensive experimental and theoretical studies have been performed for IrTe₂ and related materials [3-10]. In order to understand the relationship between the charge-orbital order and the strong spin-orbit coupling in IrTe₂, we have performed SARPES study on IrTe₂ at BL-9B, HiSOR. The crystals were cleaved at 300K (above the charge-orbital ordering temperature of 270 K) under the ultrahigh vacuum and then cooled to 20 K for the SARPES measurements. The total energy resolutions were set to about 50 meV for excitation energy of 23 eV.

Figure 1 shows SARPES spectra of IrTe₂ for in-plane spin polarization taken at 20 K with linearly polarized light along the horizontal cut (along the Γ K direction of the hexagonal Brillouin zone). In addition to the strong spin polarization near the Fermi level, spin polarizations with opposite signs are seen around -1.0 eV and -2.0 eV. In these energy regions, energy gaps are formed in the Te 5p/Ir 5d bands due to the strong spin-orbit interaction. Therefore, the in-plane spin polarizations of the bulk bands with spin-momentum locking can be assigned to possible inversion symmetry breaking in the charge-orbital ordered phase. As for the out-of-plane polarization, the strong spin polarization is observed near the Fermi level which corresponds to the surface band with quasi-one-dimensional character [8] and suggests non-trivial spin texture of the surface band in the charge-orbital ordered phase. The present SARPES results [11] show that the surface band corresponds to the edge state of quasi two-dimensional bulk band created by the charge-orbital order in IrTe₂ [9,10].

REFERENCES

1. S. Pyon, K. Kudo, and M. Nohara, *J. Phys. Soc. Jpn.* **81**, 053701 (2012).
2. J. J. Yang, Y. J. Choi, Y. S. Oh, A. Hogan, Y. Horibe, K. Kim, B. I. Min, and S.-W. Cheong, *Phys. Rev. Lett.* **108**, 116402 (2012).
3. M. Kamitani, M. S. Bahramy, R. Arita, S. Seki, T. Arima, Y. Tokura, and S. Ishiwata, *Phys. Rev. B* **87**, 180501 (2013).
4. Yoon Seok Oh, J. J. Yang, Y. Horibe, and S.-W. Cheong, *Phys. Rev. Lett.* **110**, 127209 (2013).
5. D. Ootsuki, Y. Wakisaka, S. Pyon, K. Kudo, M. Nohara, M. Arita, H. Anzai, H. Namatame, M. Taniguchi, N. L. Saini, and T. Mizokawa, *Phys. Rev. B* **86**, 014519 (2012).
6. A. F. Fang, G. Xu, T. Dong, P. Zheng, and N. L. Wang, *Sci. Rep.* **3**, 1153 (2013).
7. D. Ootsuki, S. Pyon, K. Kudo, M. Nohara, M. Horio, T. Yoshida, A. Fujimori, M. Arita, H. Anzai, H. Namatame, M. Taniguchi, N. L. Saini, and T. Mizokawa, *J. Phys. Soc. Jpn.* **82**, 093704 (2013).
8. D. Ootsuki, H. Ishii, K. Kudo, M. Nohara, M. Takahashi, M. Horio, A. Fujimori, T. Yoshida, M. Arita, H. Anzai, H. Namatame, M. Taniguchi, N. L. Saini, and T. Mizokawa, *J. Phys. Soc. Jpn.* **86**, 123704 (2017).
9. T. Toriyama, M. Kobori, Y. Ohta, T. Konishi, S. Pyon, K. Kudo, M. Nohara, K. Sugimoto, T. Kim, and A. Fujiwara, *J. Phys. Soc. Jpn.* **83**, 033701 (2014).
10. G. L. Pascut, K. Haule, M. J. Gutmann, S. A. Barnett, A. Bombardi, S. Artyukhin, D. Vanderbilt, J. J. Yang, S.-W. Cheong, and V. Kiryukhin, *Phys. Rev. Lett.* **112**, 86402 (2014).
11. Y. Okamoto, S. Iwasaki, H. Ishii, K. Kudo, M. Nohara, K. Miyamoto, T. Okuda, and T. Mizokawa, submitted.

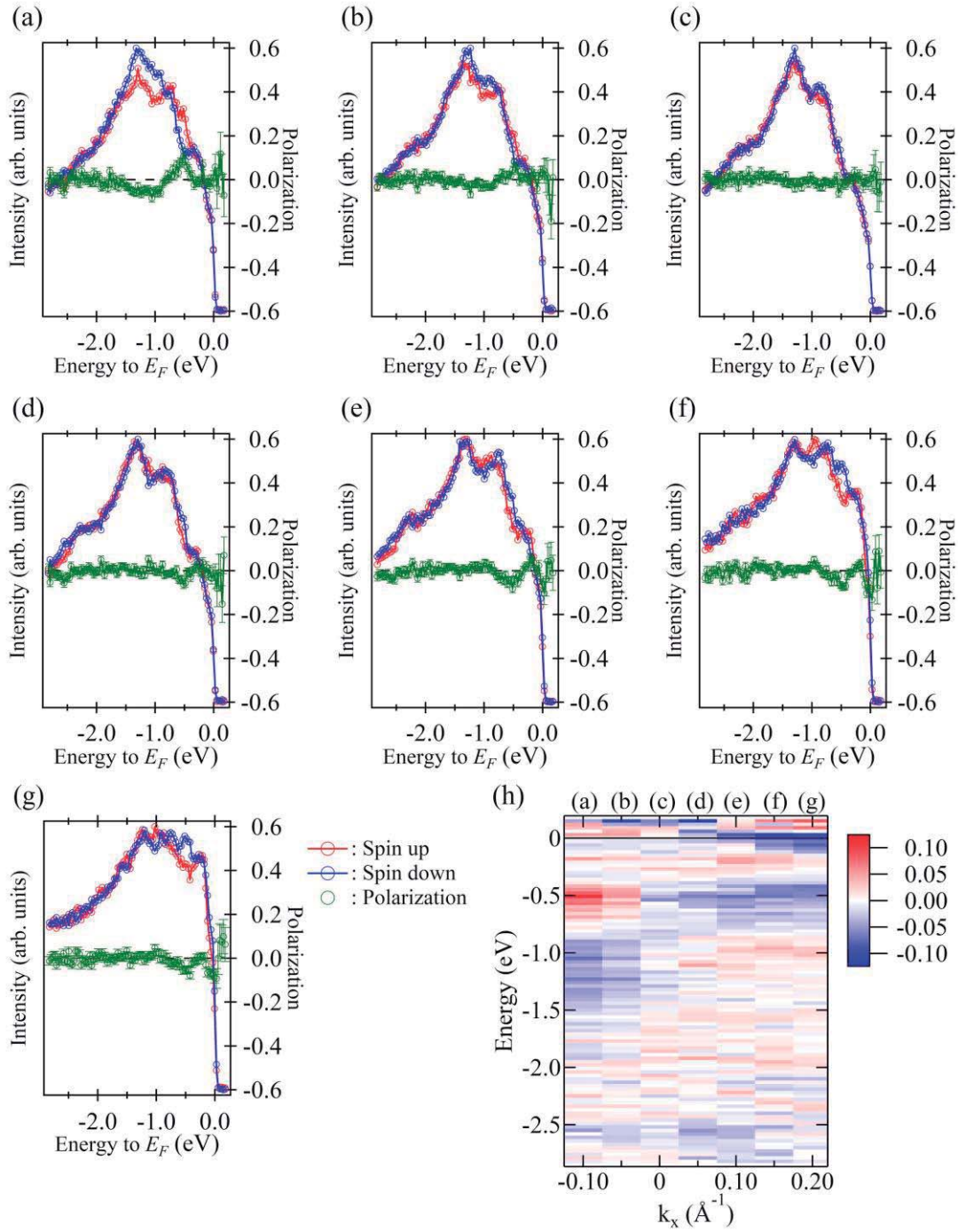


FIGURE 1. (a)-(g) SARPES spectra of IrTe₂ at 20 K along the horizontal cut taken by linearly polarized light with 23 eV. Spin polarization direction is parallel to the surface. (h) Spin polarization map. Positive and negative spin polarizations are indicated by red and blue colors.

Spin-resolved ARPES experiment on chiral semiconductor Tellurium

M. Mulazzi^a

^aHumboldt-Universität zu Berlin, Institut für Physik, Newtonstr. 15, D12489 Berlin, Germany

Keywords: Electronic structure, Spin-resolved ARPES, Tellurium.

The aim of the experiment was the determination of the spin texture of Tellurium, which is deemed by us to be interesting because, contrary to most materials, it is hedgehog-like [1] in the vicinity of the H point of the Brillouin zone.

Previously, the spin-integrated band structure was obtained on cleaved and sputter/annealed surfaces of Tellurium, namely the (10-10). Also in the present experiment we opted for sputtering and annealing (at 500 eV ion energy and annealing at progressively higher temperatures up to 350°C) as method to clean the surface. LEED measurements showed that the surface is indeed well-ordered and not reconstructed.

Due to the high resolution of the spin-resolved experiment and the relatively low photoemission cross sections for Tellurium, we limited the k-space region that we investigated to two lines crossing at the H point and perpendicular to each other.

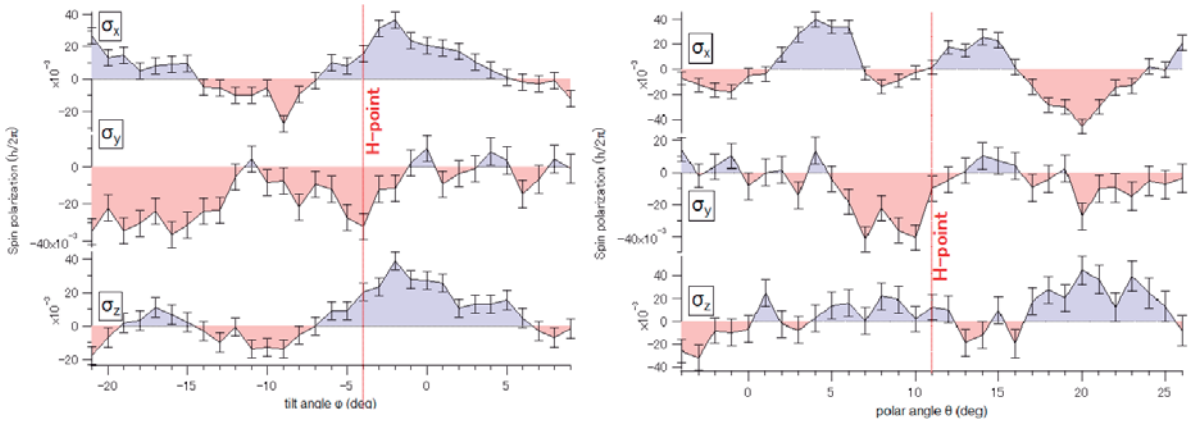


FIGURE 1. Spin-resolved ARPES spectra taken about the H point of the Brillouin zone. In the left panel the spin polarization is plotted as a function of the tilt angle, while in the right one as a function of the polar angle, perpendicular to the previous one. All the three components of the spin polarization have been measured at a binding energy of about 0.4 eV.

The measurement clearly indicate that the spin polarization is non-zero and it shows a dependence on the photoemission angle, i.e. momentum. However, only in two cases, i.e. σ_x and σ_y measured along the polar angle, it is clear that there are four peaks, whose spin polarizations have alternating signs. It is hard to distinguish four peaks in the other four cases and also the magnitude of the spin polarization is very low compared to the theoretical value that we expected. If this is an intrinsic feature of Tellurium is not clear, because other extrinsic phenomena might be present, like those reported in Ref. [2].

Further experiments are needed to clarify, for each electronic state, the real magnitude of the spin polarization and its direction.

REFERENCES

1. *Weyl Node and Spin Texture in Trigonal Tellurium and Selenium*, Phys. Rev. Lett. 114, 206401 (2015)
2. *Widespread spin polarization effects in photoemission from topological insulators*, Phys. Rev. B 84 165113 (2011)

Local Rashba effect in PtSe₂ thin film grown by molecular beam epitaxy

Mingzhe Yan¹, Kenan Zhang¹, Wei Yao¹, Shilong Wu³, Tomoki Yoshikawa³, Koji Miyamoto³, Taichi Okuda³, Shuyun Zhou^{1,2}

1. *State Key Laboratory of Low-Dimensional Quantum Physics and Department of Physics, Tsinghua University, Beijing 100084, China*
2. *Collaborative Innovation Center of Quantum Matter, Beijing 100084, China*
3. *Hiroshima Synchrotron Radiation Center, Hiroshima University, Kagamiyama 2-313, Higashi-Hiroshima 739-0046, Japan*

Keywords: PtSe₂, molecular beam epitaxy, Spin-ARPES, local Rashba effect

Layered transition metal dichalcogenides (TMDCs) have attracted extensive interest for applications in electronics, optoelectronics and valleytronics due to the strong spin-orbit coupling, sizable band gap and tunability of the electronic structure by quantum confinement effect. Platinum diselenide (PtSe₂) has emerged as an interesting compound with highest charge-carrier mobility expected in TMDCs and much improved stability. Moreover, the hidden helical spin texture with spin-layer locking in monolayer PtSe₂ has great potential for electric field tunable spintronic devices [1]. Therefore, PtSe₂ is an attractive candidate for a variety of applications. Obtaining high quality PtSe₂ films is a critical step toward this goal. Among various growth methods for thin film, molecular beam epitaxy (MBE) can provide a better control in terms of growth dynamics and realization of large size, high quality single crystalline films on various substrates with controlled film thickness. In this work, we have successfully grown the PtSe₂ thin films and by using Spin-ARPES, we systematically investigated the helical spin texture with spin-layer locking in monolayer, bilayer and bulk PtSe₂ in detail. Such MBE growth method can be further extended to other insulating substrates.

Figure 2(a)–(d) shows spin-ARPES measurements along the Γ -K and Γ -K' high symmetry directions of both 1 ML and 2 ML films. Large spin contrast is observed along the tangential direction at emission angles of -4° and 4° , respectively (dashed line in figure 2(f)). The radial and out-of-plane directions show negligible spin contrast. This is consistent with the helical spin texture as previously reported in 1 ML PtSe₂ films on Pt(111) substrate [2], confirming that it is an intrinsic effect of the PtSe₂ film rather than the influence from Pt substrate. Similar helical spin texture is also observed in centrosymmetric bulk PtSe₂ crystals (figure 2(e)), supporting the spin-layer locking mechanism induced by local Rashba effect [1]. Such helical spin texture induced by local Rashba effect makes it potentially useful for electric field tunable spintronics.

In summary, we have successfully achieved epitaxial growth of high quality PtSe₂ thin films with controlled thickness using MBE. By Spin-ARPES, we reveal the hidden local Rashba spin polarizations in our samples. Combined with its unique high charge carrier mobility and air stability, PtSe₂ is a promising candidate for applications in new-generation electronic devices.

REFERENCE

1. Zhang X, Liu Q, Luo J-W, Freeman A J and Zunger A. Hidden spin polarization in inversion-symmetric bulk crystals *Nat. Phys.* **10** 387–93 (2014)
2. Yao W *et al.* Direct observation of local Rashba spin polarization and spin-layer locking in centrosymmetric monolayer PtSe₂ *Nat. Commun.* **8** 14216–21 (2017)
3. Yan Mingzhe *et al.* High quality atomically thin PtSe₂ films grown by molecular beam epitaxy *2D Mater.* **4** 045015 (2017)

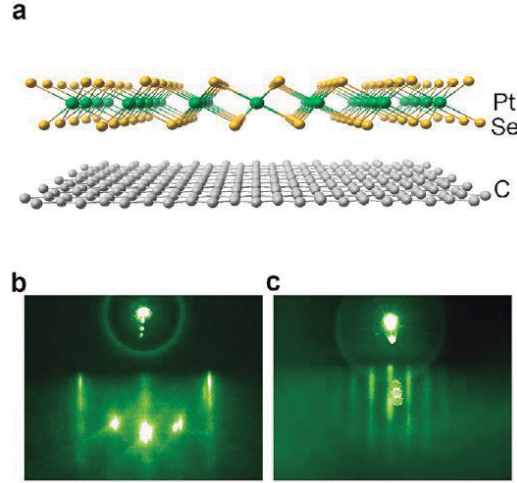


FIGURE 1: (a) Schematic view of PtSe₂ grown on graphene substrate. (b) and (c) RHEED patterns of epitaxial bilayer graphene over a 6H-SiC (0001) substrate (b) and after growing 0.8 ML PtSe₂ thin film (c).

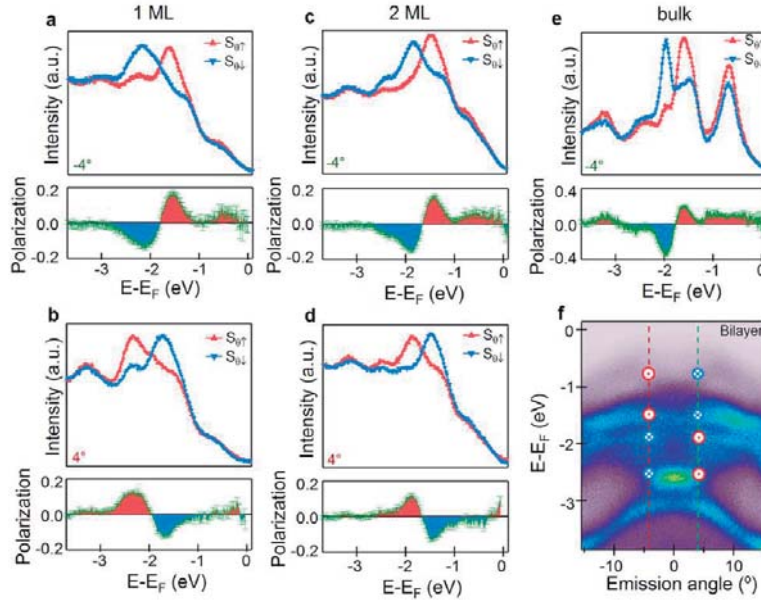


FIGURE 2: (a) and (b) Spin-resolved energy distribution curves (EDCs) for the 1 ML PtSe₂ in-plane tangential direction at emission angles of -4° and 4° , respectively. (c) and (d) Spin-resolved EDCs for bilayer PtSe₂ in-plane tangential direction at emission angles of -4° and 4° , respectively. (e) Spin-resolved EDCs for the bulk PtSe₂ in-plane tangential direction at emission angles of -4° . (f) ARPES data of 2 ML PtSe₂ film measured at different emission angles.

Rich Surface Electronic Structure of Group-X Transition-Metal Dichalcogenides

O. J. Clark¹, J. M. Riley^{1,2}, J. Feng¹, P. D. C. King¹

¹ School of Physics & Astronomy, University of St Andrews, St Andrews KY1 69SS, United Kingdom

² Diamond Light Source, Harwell Campus, Didcot OX11 0DE, United Kingdom

Keywords: Transition-metal dichalcogenides, topological surface states, bulk Dirac fermions, spin-ARPES

Transition metal dichalcogenides (TMDs) are layered compounds renowned for their wide array of bulk electronic phases, from charge-density wave phases [1] to ‘hidden’ spin polarizations [2]. These properties arise largely from electrons occupying the transition-metal d-orbital manifold and vary extensively when substituting the transition metal for another. In contrast, ladders of bulk Dirac points (BDPs) and topological surface states (TSS) have been recently discovered across the full material family of TMDs, owing to their origin being solely within the chalcogen p-orbital manifold [3,4].

The group-X TMDs (Pt, Pd) have a particularly rich surface electronic structure. A series of band inversions along the k_z axis of their Brillouin zone induces up to three topological states (labeled 0, 1 and 2 in Fig. 1). There are numerous other surface states (labeled 3, 4 and 5) within these compounds of unknown origin. The extensive three-dimensionality of the bulk electronic structure results in only narrow k_z projected band gaps in which these surface states can occupy, often resulting in complicated and occasionally ‘flat’ band dispersions. The reduction of spin-orbit strength from PdTe₂ to PtSe₂ reduces the sizes of the projected band gaps further still, most obvious when comparing TSS2 and SS3 between the two compounds show in Fig. 1.

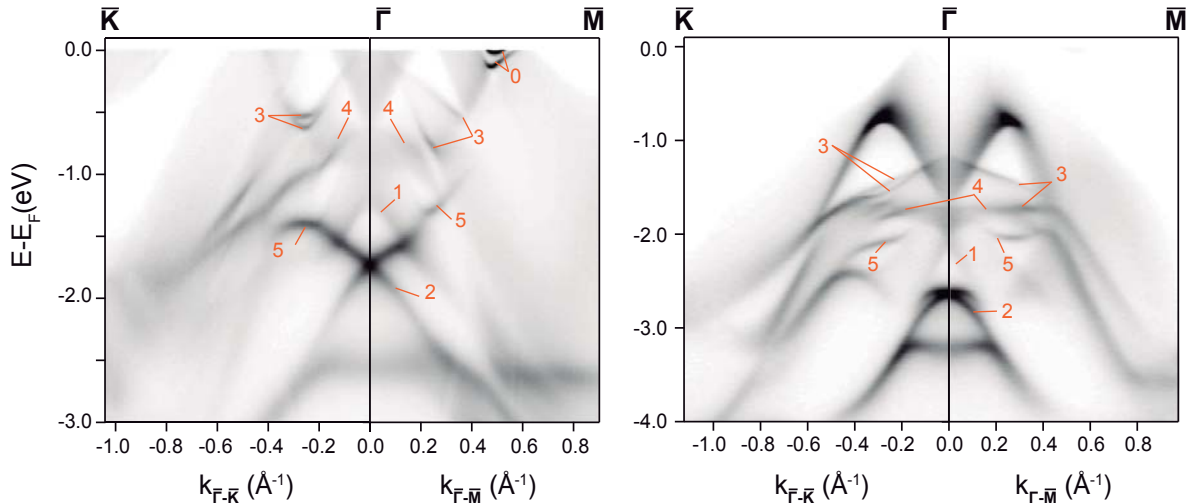


FIGURE 1. Full K– Γ –M paths for PdTe₂ (left) and PtSe₂ (right). The photon energy used in both compounds corresponds to a bulk A-plane. Surface states are labeled. Data is from the i05 beamline of Diamond Light Source, U.K.

For a conventional surface state of Rashba or topological origin, the chiral component of spin should be dominant, with both the radial and out-of-plane components negligible. Here, the surface states deviate substantially away from circular geometry, opening the possibility of far more complex spin textures. Figure 2 shows three component spin-resolved energy distribution curves for PdTe₂, along both the Γ -K and Γ -M directions as well as an intermediate line Γ -T, where T is midway between M and K azimuthally.

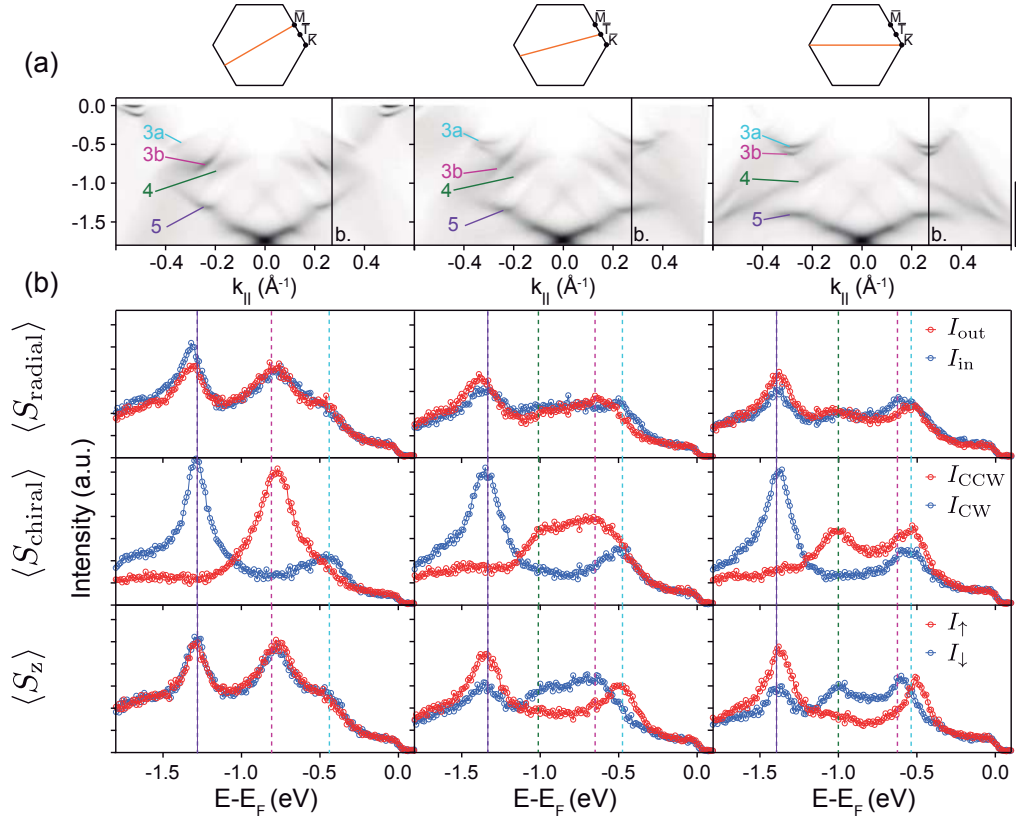


FIGURE 2. Three component spin-EDCs taken at a photon energy of 27eV shown in (b) are taken at the momenta indicated in (a). Lines indicating the position of surface states in the spin-integrated spectra are shown. Spin-EDCs are corrected for the Sherman function.

Along the Γ -M direction, where only the chiral component is permitted to be non-zero for symmetry reasons, all surface states give a strong signal with the top branch of SS3 and SS5 having an opposite direction of chirality to the lower branch of SS3. When rotating azimuthally, a clear out-of-plane (S_z) polarization starts to develop for all states probed, becoming maximal along the Γ -K direction. Additional data collected at BL9B (not shown) demonstrates how this out-of-plane component persists along the full momentum range of the surface states, and each obeys time-reversal symmetry. An equivalent dataset for PtSe₂, shows how significant radial warping of these states develops in addition to the out-of-plane component. This results from the reduced spin-orbit coupling strength of the selenium containing compound enforcing flatter dispersions. The origins and full spin textures of each of these surface states will be discussed in an upcoming publication [5].

Band inversions formed within a single-orbital manifold of the TMDs rely on large bandwidths along k_z of each of the bulk bands contained within, and is therefore inherently associated with small k_z projected band gaps in the surface zone. The diversity in the states that make up the non-trivial surface electronic structure of the group-X TMDs is testament to this, and demonstrates how interlinked, complex surface electronic structures are likely common to all compounds contain topological phases within a single-orbital manifold.

REFERENCES

1. K. Rossnagel *et al.*, Fermi surface, charge-density-wave gap, and kinks in 2H-TaSe₂, *Physical Review B* **72**, 121103(R) (2005)
2. J. M. Riley *et al.*, Direct observation of spin-polarized bulk bands in an inversion-symmetric semiconductor *Nature Physics* **10**, 835–839 (2014)
3. M. S. Bahramy, O. J. Clark *et al.* Ubiquitous formation of bulk Dirac cones and topological surface states from a single orbital manifold in transition-metal dichalcogenides. *Nature Materials* **17**, 23–27 (2018)
4. O. J. Clark *et al.* Fermiology and Superconductivity of Topological Surface States in PdTe₂. *Physical Review Letters* **120**, 156401 (2018)
5. O. J. Clark *et al.*, Effect of small k_z projected band gaps on the topologically non-trivial surface electronic structure in group-X transition metal dichalcogenides, *in preparation* (2018)

Experimental observation of node-line-like surface states in LaBi

Baojie Feng^a, Jin Cao^b, Meng Yang^c, Ya Feng^{a,d}, Shilong Wu^e, Botao Fu^b, Masashi Arita^a, Koji Miyamoto^a, Shaolong He^d, Kenya Shimada^a, Youguo Shi^c, Taichi Okuda^a and Yugui Yao^b

^a*Hiroshima Synchrotron Radiation Center, Hiroshima University, 2-313 Kagamiyama, Higashi-Hiroshima 739-0046, Japan*

^b*Beijing Key Laboratory of Nanophotonics and Ultrafine Optoelectronic Systems, School of Physics, Beijing Institute of Technology, Beijing 100081, China*

^c*Institute of Physics, Chinese Academy of Sciences, Beijing 100190, China*

^d*Ningbo Institute of Materials Technology and Engineering, Chinese Academy of Sciences, Ningbo 315201, China*

^e*Graduate School of Science, Hiroshima University, 1-3-1 Kagamiyama, Higashi-Hiroshima 739-8526, Japan*

Keywords: node line, magnetoresistance, surface states, topological, ARPES, first-principles calculations.

Topological semimetals represent a novel class of quantum materials whose conduction and valence bands touch at discrete points or extended lines. Until now, three types of topological semimetals have been discovered: Dirac, Weyl and nodal line. In Dirac/Weyl semimetals, the energy-momentum dispersion is linear along all momentum directions, forming Dirac/Weyl cones in the proximity of the Fermi level. In nodal line semimetals, the crossing points form extended lines in the momentum space, *i.e.*, the nodal lines. While the Dirac cones or nodal lines discovered in topological semimetals typically derive from the bulk bands, an interesting question is that whether they can exist as surface states of three-dimensional crystals. The nodal line surface states could manifest extraordinary properties that are distinct from other two-dimensional Dirac materials. To date, the surface Dirac cones have already been extensively studied in topological insulators, such as the Bi₂Se₃ family materials, while theoretical and experimental studies on the surface nodal lines are still rare.

Recently, rare-earth monpnictide LaBi has been predicted to be a topological insulator based on first-principles calculations. Moreover, magneto-transport measurements showed that LaBi hosts extremely large magnetoresistance (XMR), in analogy to some topological semimetals, such as Cd₃As₂, TaAs, and ZrSiS. These results have stimulated great research interest to search for the Dirac bands in LaBi. Recent angle-resolved photoemission spectroscopy (ARPES) measurements revealed that there are multiple surface Dirac cones on the (001) surface of LaBi. However, the details of the band structures are still controversial. J. Nayak *et al.* and X. H. Liu *et al.* reported two surface Dirac cones at the \bar{X} point with an energy separation of 75 meV and 80 meV, respectively [1,2]. In contrast, R. Lou *et al.* reported only one Dirac cone at the \bar{X} point. Therefore, clarifying these controversies, which is essential to understand the extraordinary transport properties in LaBi, calls for further experimental and theoretical efforts.

In this Letter, we present the results of high-resolution ARPES measurements and first-principles calculations on the electronic structures of LaBi. We find that the surface states near the \bar{X} points resemble Dirac nodal lines, bridging the band gap opened by spin-orbit coupling (SOC) and band inversion. In addition, our calculation results show that these node-line-like bands originate from the topological surface states (TSSs) of LaBi. These results may provide important information to understand the extraordinary physical properties in LaBi and could stimulate further research interest to search for the exotic physical properties associated with nodal line fermions

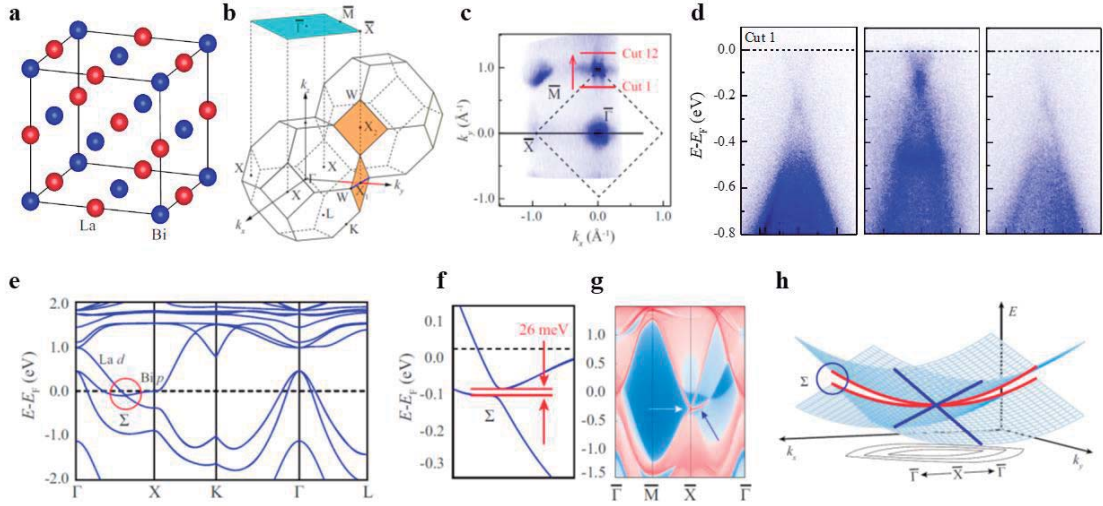


FIGURE 1. (a) Crystal structure of LaBi. Red and blue balls represent La and Bi atoms, respectively. (b) Bulk Brillouin zone and the (001)-projected surface Brillouin zone. (c) Photoemission intensity at the Fermi level of LaBi measured with 31-eV photons. Red lines indicate the momentum cuts along which the ARPES intensity plots in (d) were taken. (d) ARPES intensity plots along the red lines in (c). (e) Calculated bulk bands of LaBi. (f) Zoom-in band structures in the red circles of (e). (g) Surface band structures of the (001) surface of LaBi. The white arrow indicates the linear band crossing. (h) Schematic drawing of the surface state from one of the bulk X point. For clarity, the C_4 -related surface state from an inequivalent bulk X point is not shown here. The band dispersions along perpendicular directions are indicated by red (linear) and blue lines (quadratic). The constant energy contours are shown in the bottom.

REFERENCES

1. J. Nayak, S.-C. Wu, N. Kumar, C. Shekhar, S. Singh, J. Fink, E. E.D. Rienks, G. H. Fecher, S. S.P. Parkin, B. Yan, and C. Felser. *Nat. Commun.* **8**, 13942 (2016).
2. X. H. Niu, D. F. Xu, Y. H. Bai, Q. Song, X. P. Shen, B. P. Xie, Z. Sun, Y. B. Huang, D. C. Peets, and D. L. Feng. *Phys. Rev. B* **94**, 165163 (2016).
3. R. Lou, *et al.* *Phys. Rev. B* **95**, 115140 (2017).

Spin Texture of Topological Surface States on the Kondo Insulator $\text{SmB}_6(111)$

Yoshiyuki Ohtsubo^{a, b}, Yuki Yamashita^b, Koji Miyamoto^c, Taichi Okuda^c,
Wataru Hirano^d, Fumitoshi Iga^d and Shin-ichi Kimura^{a, b}

^aGraduate School of Frontier Biosciences, Osaka University, Suita 565-0871, Japan

^bDepartment of Physics, Graduate School of Science, Osaka University, Toyonaka 560-0043, Japan

^cHiroshima Synchrotron Radiation Center, Hiroshima University, Higashi-Hiroshima 739-0046, Japan

^dCollege of Science, Ibaraki University, Mito 310-8512, Japan

Keywords: Topological Kondo Insulator, spin-resolved ARPES, SmB_6

Topological surface states (TSS) with typical spin texture are one of hot topics in solid-state physics in this decade [1]. Among them, TSS and its spin texture realized in the non-conventional bulk insulators such as Kondo insulators whose bandgap opens due to the strong electron correlations, namely Kondo effect, is gathering much attention in these days (Topological Kondo Insulator: TKI) [2]. It is because they are regarded as a promising playground to search for new, exotic electronic phenomena driven by concerted effects between strong electron correlation and topological order.

Samarium hexaboride (SmB_6) is a typical and long-known Kondo insulator. Moreover, SmB_6 is one of the 1st materials proposed as a candidate of TKI [2]. Since one of the most evident electronic phenomena due to the topological order is the metallic surface states dispersing across the bulk bandgap, the surface electronic structure of SmB_6 has been extensively studied [3-4]. Although some angle-resolved photoelectron spectroscopy (ARPES) studies have reported metallic surface states as expected for TSS [3], the other report has claimed its origin as topologically trivial and accidental surface states [4]. One of the reason why the discussion is still controversial is that most of earlier ARPES studies are performed on the cleaved (001) surface of SmB_6 single crystals; the SmB_6 single crystal can be cleaved only along (001). Since the cleaved surface can contain multiple atom-truncation planes (surfaces terminated by Sm or B_6 , for example) and the (001) surface even forms surface superstructures, it was quite difficult to make an unambiguous assignment of the surface states and its topology.

In this work, we performed high-resolution spin-resolved ARPES measurements at BL-9B of HiSOR on $\text{SmB}_6(111)$, which is the new surface orientation obtained this time. The (111) surface cannot be obtained by cleaving. Instead, we heated the mechanically-polished single crystal surface up to 1600 K in an ultra-high vacuum chamber, so that most of the contaminants as well as the damages to the surface by polishing are removed.

Figure 1 (a) shows the Fermi contour of the $\text{SmB}_6(111)$ clean surface taken at the temperature of 20 K. Three-fold oval contours, obeying the C_{3v} symmetry group of the (111) surface, are clearly observed. At 20 K, the bulk electronic structure of SmB_6 is insulating. Therefore, the observed electronic states at the Fermi level here are from the surface electronic structure. Due to the time-reversal symmetry, the Fermi-contour shape of the initial states should be six-fold, as depicted in Fig. 1 (c). The lack of the photoelectron intensity for the other three-fold contours would be due to the ARPES experimental geometry and the lack of the mirror plane on (-110). Actually, the other three-fold Fermi contour was observed by the other ARPES experiments with different experimental geometries (not shown).

In order to obtain further insight into this metallic surface states, especially about its topological character, spin texture of these states are observed as shown in Fig. 1 (b) by the spin-resolved momentum distribution curves at the Fermi level. It clearly shows the spin-resolved peak at $k_y \sim 0.25 \text{ \AA}^{-1}$

corresponding to the Fermi contour observed by the spin-integrated ARPES (Fig. 1 (a)). In addition, a small but finite peak with the opposite spin polarization was also observed at $k_y \sim -0.25 \text{ \AA}^{-1}$. This peak would correspond to the other three-fold Fermi contour discussed above, which is observed as a weak but finite peak thanks to the spin resolution.

Based on these results, we could obtain the whole spin texture of the metallic surface states at the Fermi level, as depicted in Fig. 1 (c). It indicates the single Fermi contour enclosing each \bar{M} point on the surface Brillouin zone, which is the time-reversal invariant momenta (TRIM). Such situation is the typical topologically non-trivial surface electronic structure and therefore we can conclude that SmB_6 is the topological Kondo insulator without any ambiguity.

Further studies and analysis for this peculiar surface electronic structure realized by the concerted effect between topology and strong electron correlation is in progress.

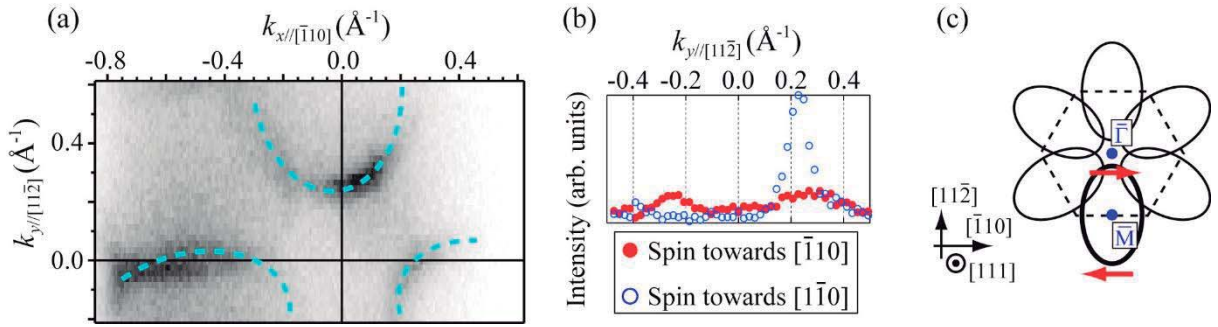


FIGURE 1. (a) Fermi contour of the $\text{SmB}_6(111)$ clean surface measured by ARPES ($h\nu = 26 \text{ eV}$, $T = 20 \text{ K}$). Dashed lines are guides to the eye. (b) Spin-resolved ARPES MDCs taken along $[112]$ ($h\nu = 26 \text{ eV}$, $T = 20 \text{ K}$). (c) A schematic drawing of the Fermi contour and the observed spin orientations.

REFERENCES

1. M. Z. Hasan and C. L. Kane, *Rev. Mod. Phys.* **82**, 3045 (2010).
2. M. Dzero *et al.*, *Phys. Rev. Lett.* **104**, 106408 (2010).
3. N. Xu *et al.*, *J. Phys.: Condens. Matt.* **28**, 363001 (2016) and references therein.
4. P. Hlawenka *et al.*, *arXiv*: 1502.01542 (2015).

Spin polarized surface state derived from d-electrons on W(100)

K. Miyamoto^a, T. Matsuda^b, T. Okuda^a, H. Sato^a and J. Henk^c

^a*Hiroshima Synchrotron Radiation Center, Hiroshima Univ.*

^b*Graduated School of Science, Hiroshima Univ.*

^c*Institut für Physik, Martin-Luther-Universität*

Keywords: Topological crystalline metal, Spin-ARPES

Topological materials and topological crystalline material possess edge state with spin polarization called as topological surface state (TSS). The spin polarization is caused by spin-orbit interaction in a combination with a broken space inversion symmetry. We have discovered spin-polarized Dirac-cone-like surface state formed by d-electrons on W(110), which is reminiscent of TSS[1]. By recently detail band calculation of W, it suggests that the artificial strained in top, second and third layer of W open semimetal band gap, which lead to non-zero mirror Chern number i.e., our discovered surface state of W(110) is classified as edge state of topological crystalline transition metal. According to this theory, it is interesting which the various surfaces such as (100) and (110) of tungsten have topologically spin-polarized Dirac-cone surface states or not. In this report, we will clarify a spin-polarized surface state on clean W(100) around $\bar{\Gamma}$ using spin- and angle-resolved photoemission spectroscopy (Spin-ARPES) at BL-9B (HiSOR).

Figure 1 shows angle-resolved photoemission spectra without and with spin-resolution along $\bar{\Gamma}\bar{M}$, taken at photon energy of 43 eV with s-polarized light. In spin-integrated ARPES result (left figure), a band dispersion (S_1) crossing at $\bar{\Gamma}$ at binding energy of 1.1 eV is shown. Because the band dispersion and energy position of the observed crossing band is independent on photon energy from 20 to 43 eV, it is concluded that S_1 is derived from surface. Furthermore, in order to confirm the spin feature of S_1 , we have performed spin-ARPES measurement as shown in middle and right panels of Fig.1. Here, the observed spin component is aligned along in-plane spin component normal to $\bar{\Gamma}\bar{M}$. In the spin-up spectra, there is one branch of S_1 up-ward dispersion from -3 to 1.5 deg. On the other hand, counterpart branch of S_1 is observed in spin-down state. Consequently, we have clarified that the S_1 is the spin-polarized surface-derived state caused by spin-orbit interaction. In detail, we introduce you in my presentation.

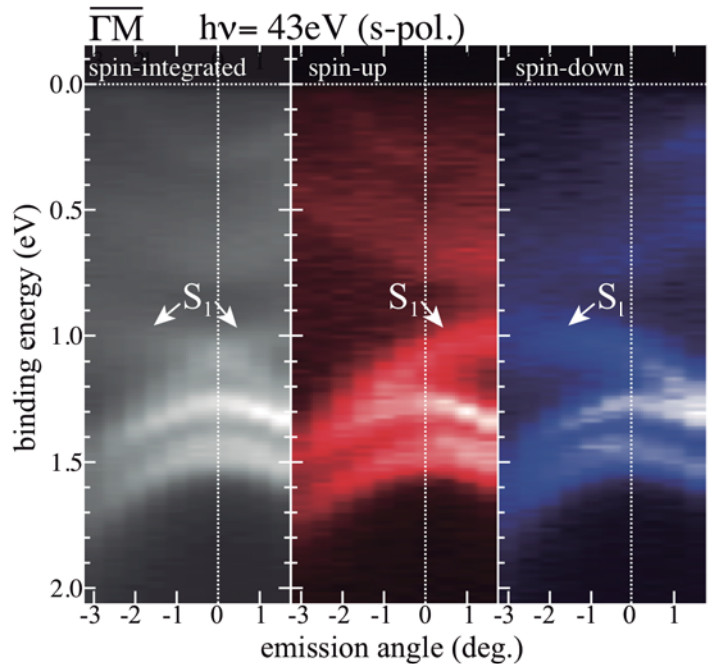


Fig.1 Spin-integrated (left) and spin-resolved ARPES intensity (middle: spin-up, right:spin-down) for W(100) along $\bar{\Gamma}\bar{M}$. The observed spin orientation is aligned along the in-plane spin component normal to $\bar{\Gamma}\bar{M}$.

REFERENCES

1. K. Miyamoto et al., Phys. Rev. Lett. 108, 0066808 (2012).
2. D. Thonig et al., Phys. Rev. B **94**, 155132.

Signature of hidden order in spin resolved photoemission spectra of Sr_2IrO_4

S. H. Kim^a, Y. K. Kim^a and B. J. Kim^{b,c,d}

^a*Department of Physics, Korea Advanced Institute of Science and Technology, Daejeon 34141, Republic of Korea*

^b*Max Planck Institute for Solid State Research, Heisenbergstrasse 1, 70569 Stuttgart, Germany*

^c*Department of Physics, Pohang University of Science and Technology, Pohang 790-784, South Korea*

^d*Center for Artificial Low Dimensional Electronic Systems, Institute for Basic Science (IBS), 77 Cheongam-Ro, Pohang 790-784,*

Keywords: iridate, spin-resolved photoemission spectroscopy

We have performed spin- and angle-resolved photoemission spectroscopy on 5d transition metal oxide compound called iridates. Spin polarized spectra were successfully accumulated in momentum dependent manner which reveal unexpected 2-fold symmetry.

Single layer iridate compound Sr_2IrO_4 becomes spin-orbit coupling assisted antiferromagnetic Mott insulator below T_N [1]. Due to the octahedral rotation, it additionally shows finite canted magnetic moment [2] which could introduce finite spin polarization in their electronic structure. Obtained spin polarized spectra prove such possible spin polarization. Furthermore, spin polarizations in different momentum position show distinct signs which follows 2-fold symmetry rather than 4-fold symmetry of tetragonal crystal structure. As shown in figure 1, spin polarization spectra taken at the momentum position 1 and 2 have finite negative value (binding energy 0.3~0.1 eV) while that in position 3 and 4 return positive value.

This reduced rotational symmetry of spin suggests formation of additional phase that obeys 2-fold rotational symmetry. Indeed, recent experimental and theoretical works reveal that there could be hidden order of 2-fold symmetry in pristine and electron doped Sr_2IrO_4 [3,4]. Our spin polarization spectra thus may provide additional information on the genuineness of that hidden order which should be extracted out in detail and careful consideration

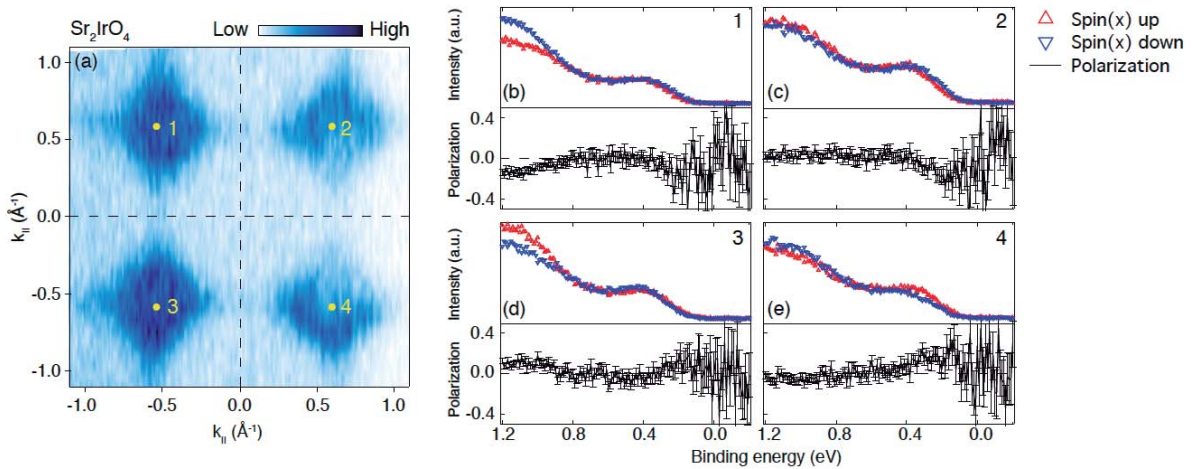


FIGURE 1. (a) Constant energy map of ARPES spectra at the top of low Hubbard band. (b)-(e) Energy distribution curves of spin up (red triangle) and down (blue inverse triangle) obtained from different momentum positions 1-4 indicated in (a). Black lines under each panel show spin polarization as a function of binding energy.

REFERENCES

1. B. J. Kim et al., *Phys. Rev. Lett.* **101**, 076401 (2006).
2. J. H. Kim et al, *Phys. Rev. Lett.* **108**, 177003 (2012).
3. A. de la Torre et al., *Phys. Rev. Lett.* **115**, 176402 (2015).
4. Sen Zhou, Kun Jiang, Hua Chen, and Ziqiang Wang, *Phys. Rev. X* **7**, 041018 (2017).

Direct Experimental Verification on spin-resolved Valley Structure in two-dimensional MX_2 ($\text{M}=\text{Mo},\text{W};\text{X}=\text{S},\text{Se}$) Semiconductors

Wenjuan Zhao¹, Yuan Huang¹, Shilong Wu², K. Miyamoto², T.Okuda²,
Guodong Liu^{1*} and Xingjiang Zhou^{1*}

¹National Laboratory for Superconductivity, Beijing National Laboratory for Condensed Matter Physics, Institute of Physics, Chinese Academy of Sciences, Beijing 100190, China

²Hiroshima Synchrotron Radiation Center, Hiroshima University, 2-313 Kagamiyama, Higashi-Hiroshima, Hiroshima 739-0046, Japan

Keywords: 2D material, transition metal dichalcogenides (TMDCs), Spin and Angle Resolved Photoemission Spectroscopy (SARPES or spin-ARPES)

Spin-valley locking in monolayer transition metal dichalcogenides is not fully understood yet. Basically, it is believed that the spin polarization at K valley is 100%, and it reverses sign at K' [1, 2]. But, there has no direct observation on this prediction in theory. What's more, it is also an interesting point whether incident beam or other factors in ARPES measurements can control the spin polarization and spin-valley locking or not. Up to now, there are only few works of spin-resolved ARPES on monolayer TMDCs [3-5]. It calls for a systematic research on the involved spin electronic states and an in-depth understanding on this issue. The investigation is also significant to the possible application in spintronics and valleytronics. The approved beam time in HiSOR was used to do Spin and Angle Resolved Photoemission Spectroscopy (SARPES) measurements on the typical monolayer TMDC material WSe_2 .

In Fig.1(a)[2], it shows the typical unit cell of 2H stacking WSe_2 . Fig.1(b) shows the schematic drawing of spin-valley locking[1].The hexagon Brillouin zone (BZ) is given in green guide line. And the momentum position of ARPES measurement used to focus on the K point is marked as blue line in Fig.1(c). Fig.1(d) shows the corresponding dispersion where the spin-resolved EDCs was taken along the dashed black line.

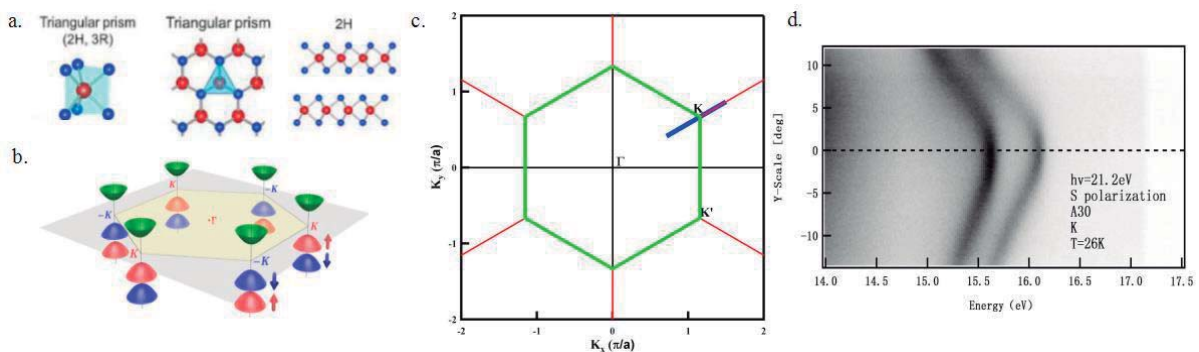


FIGURE 1. Electronic structure of monolayer WSe_2 . (a) The crystal structure of 2H- WSe_2 . The red and blue balls stand for W and Se [2], respectively. (b) The schematic drawing of spin-valley locking [1]. (c) The WSe_2 Brillouin zone (BZ). Green line is the hexagon BZ of monolayer WSe_2 . (d) The measured band dispersion to find K position. The momentum position of this spectrum is shown in (c) using blue line.

Fig.2 demonstrates the spin-resolved photoemission spectra at K or K' under different photon energy and polarization. In Fig.2(a), it shows the spin polarization at adjacent two K points. Both P_x and P_z (spin polarization along x and z direction) are reversed from K to K' , which is consistent with theory. To see if different photon parameters can change spin polarization or not, we tried different photon polarization and photon energy in Fig.2.(b) and (c). It's obvious that spin polarization in magnitude change under different

photon polarization and photon energy. Among these data, we got the highest spin polarization at 21.2eV and under circular left (CL) polarization.

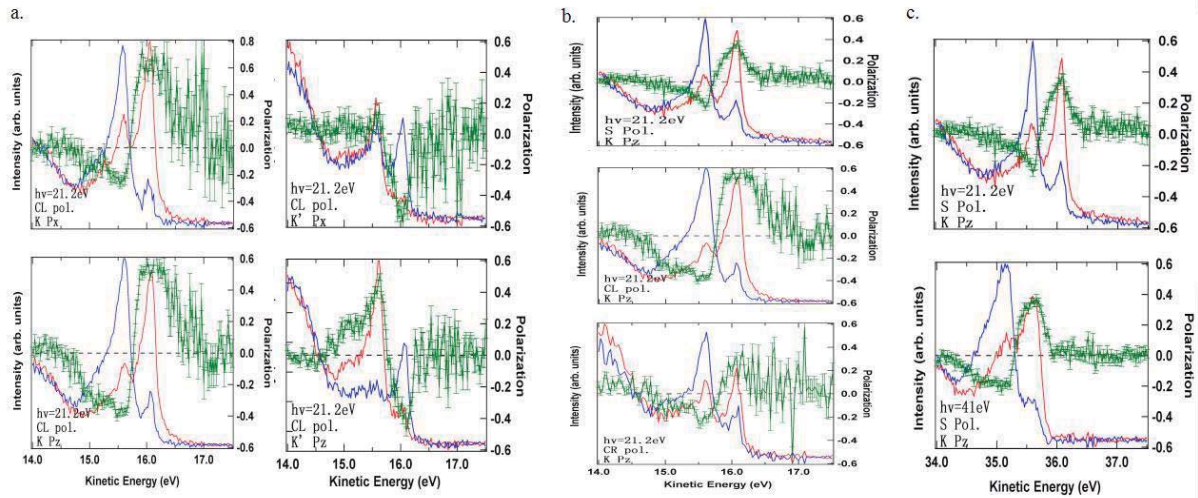


FIGURE 2. Spin polarization of monolayer WSe2. (a) A comparison between K and K'. Red line and blue line stand for spin-up and spin-down. Green line represents spin polarization. The up row corresponds to Px while down row Pz. Left column and right column is for K and K' ($h\nu=21.2\text{eV}$, photon polarization CL), respectively. (b) Spin polarization under different photon polarization. From up to down, it shows S, CL and CR photon polarization, respectively. (c) Spin polarization at different photon energy. The upper panel shows Pz spin polarization at 21.2eV photon energy. While the lower one displays that measured at 41eV photon energy (S photon polarization).

TABLE 1. The summary of spin polarization. The blue number means the spin polarization of the lower band in K splitting. The signs * identify the cases with very high polarization. The signs '-' stand for spin down.

$h\nu(\text{eV})$	Polarization	Momentum	Pz(%)	Px(%)	Ptotal(%)
21.2	S	K	37	41	55
			-25	-21	-33
	CL	K	-62	-56	-84*
			46	48	67
		K'	65	72	97*
			-40	-27	-48
CR	K	-49	-58	-76*	
		50	16	52	
	K	37	46	59	
41	S	K	-26	-47	-54
			38	32	50
	CL	K	-25	-5	-26
			68	57	89*
		K'	-42	-15	-45

Table 1. is a summary of spin polarization on various measurement conditions. We did SARPES study on adjacent K points using different photon polarization and photon energy, and got some systematic results. We directly show the nearly 100% spin polarization at K and K' in experiment. The spin polarization shows opposite sign from K to K'. However, we do not see spin polarization reverse its sign with photon polarization changing from CL to CR. But it is clear that the large modulation of spin polarization appears with changed photon polarization and photon energy. Based on these results, a paper writing is now in progress.

REFERENCES

1. D. Xiao et al., *Phys. Rev. Lett.* **108**,196802 (2012) .
2. YJ. Zhang et al., *2D Mater.* **2** , 044004 (2015) .
3. K. Sugawara et al. *Appl. Phys. Lett.* **107**, 071601 (2015).
4. S.K. Mo et al., *J. Phys.: Condens. Matter* **28** 454001 (2016).
5. H. Bana et al., *arXiv*:1802.02220 (2018)

Sulfur Compound formed at surface of Granulated Coal Ash Capped in Organically Enriched Sediment

Kyunghoi Kim^a, Tamiji Yamamoto^b and Shinjiro Hayakawa^c

^a*Department of Ocean Engineering, Pukyong National University, 45, Yongso-ro, Nam-Gu, Busan 48513, Republic of Korea*

^b*Department of Biosphere Science, Hiroshima University, 1-4-4, Kagamiyama 1 chome, Higashi-Hiroshima 739-8528, Japan*

^c*Graduate School of Engineering, Hiroshima University, 1-4-1, Kagamiyama 1 chome, Higashi-Hiroshima 739-8527, Japan*

Keywords: Granulated coal ash, Capping, Hydrogen sulfide, Sulfur compound

Deterioration of sediment quality in coastal inner bay is a serious problem due to the inflow of organic load. In such organically enriched sediment, hydrogen sulfide is produced by sulfate reduction (Richard, 2005). Hydrogen sulfide is highly toxic and fatal to living organisms. Hydrogen sulfide also consumes oxygen in the seawater when it is oxidized. It is important to remediate deteriorated sediments and preserving healthy ecosystems. Several articles have tried to develop techniques for remediating deteriorated sediments using recycled materials such as iron slags (Yamada et al., 1987; Johansson and Gustafsson, 2000) and clam shells (Kwon et al., 2003; Asaoka et al., 2009; Yamamoto et al., 2012).

Fukuyama inner harbor is an enclosed bay located in the western Seto Inland Sea of Japan. This area has many serious problems, such as outbreak of malodorous gas, raw scum, eutrophication and blue tide. Granulated Coal Ash(GCA) was applied for the remediation of Fukuyama inner harbor (Nakamoto et al., 2017). In order to investigate mechanism of hydrogen sulfide removal with GCA in Fukuyama inner harbor, XAFS analysis was carried out.

XAFS analysis (beamline BL-11 of the Hiroshima Synchrotron Research Center, HiSOR) of the K-edge of sulfur was performed for the components contained in the sampled GCA in Fukuyama bay (Hayakawa et al., 2008). The standard spectra of FeS and humic acid are shown in Figure 1, and normalization was carried out using software REX2000.

The sulfur K-edge peak of the initial GCA was 2482 eV, indicating sulfate. On the other hand, sulfur K-edge curve of the Fukuyama GCA shell has an inflection point at approximately 2469, 2473.5, 2476 and 2482 eV, which corresponds to FeS and humic acid. These results on XAFS analysis suggested that formation of FeS play an important role in the removal of hydrogen sulfide in Fukuyama inner harbor (Hayashi et al., 2014).



REFERENCES

1. Asaoka, S., Yamamoto, T., Kondo, S., Hayakawa, S., 2009. Removal of hydrogen sulfide using crushed oyster shell from pore water to remediate organically enriched coastal marine sediments. *Bioresource Technology* 100, 4127-4132.
2. Johansson, L., Gustafsson, J. P., 2000. Phosphate removal using blast furnace slags and opoka-mechanisms. *Water Research* 34, 259-265.
3. Hayashi, A., Asaoka, S., Watanabe, T., Kaneko, R., Takahashi, K., Miyata, Y., Kim, K., Yamamoto, T., Inoue, R., Ariyama, T., 2014. Mechanism of Suppression of Sulfide Ion in Seawater Using Steelmaking Slag. *ISIJ International* 54, 1741-1748.
4. Kwon, H. B., Lee, C. W., Jun, B. S., Yun, J. D., Weon, S. Y., Koopman, B., 2004. Recycling waste oyster shells for eutrophication control. *Resources Conservation & recycling* 41, 75-82.
5. Nakamoto, K., Hibino, T., Hino, K., Touch, N., 2015. Granulated coal ash – used method for remediation

- of organic matter enriched coastal sediments. *Procedia Engineering* 116, 326-333.
6. Richard, D., Morse, J.W., 2005. Acid volatile sulfide (AVS). *Mar. Chem.* 97, 141-197.
 7. Yamada, H., Kayama, M., Saito, K., Hara, M., 1987. Suppression of phosphate liberation from sediment by using iron slag. *Water Research* 21, 325-333.
 8. Yamamoto, T., Kondo, S., Kim, K. H., Asaoka, S., Yamamoto, H., Tokuoka, M., Hibino, T., 2012. Remediation of muddy tidal flat sediments using hot air-dried crushed oyster shells. *Marine Pollution Bulletin* 64, 2428-2434.

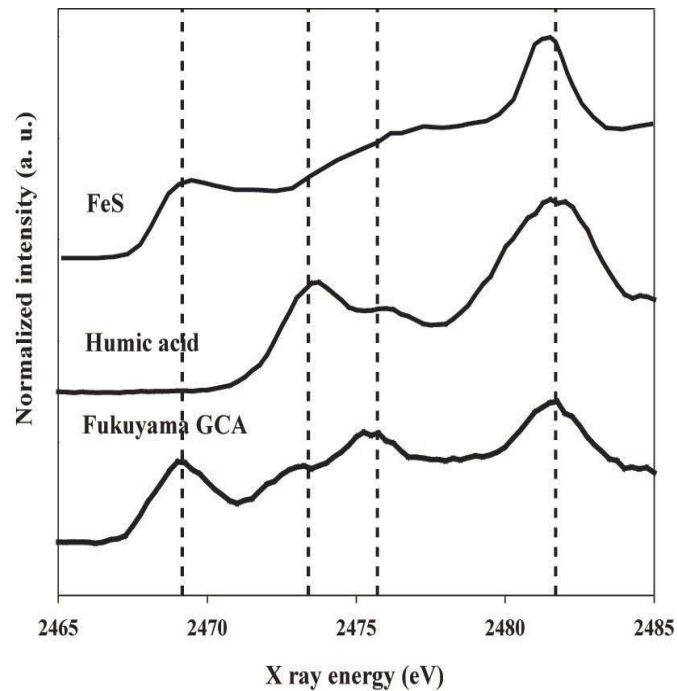


FIGURE 1. Sulfur K edge XAFS spectra of Granulated Coal Ash sampled at Fukuyama inner harbor.

Identifying sulfur species in marine sediments collected from Seto Inland Sea, Japan using XAFS

Satoshi ASAOKA^a, Yasuhiro USHIHARA^b, Akira UMEHARA^c,
Kazuhiko TAKEDA^d, Hiroshi SAKUGAWA^d and Shinjiro HAYAKAWA^e

^a *Research Center for Inland Seas, Kobe Univ. (5-1-1 Fukaeminami, Higashinada Kobe 658-0022 Japan)*

^b *Research Center for Inland Seas, Kobe Univ. (2746 Iwaya, Awaji 656-2401 Japan)*

^c *Environ. Res. Manage. Cent., Hiroshima Univ. (1-5-3, Kagamiyama, Higashihiroshima, 739-8513 Japan)*

^d *Grad. School of Biosph. Sci., Hiroshima Univ. (1-7-1 Kagamiyama, Higashi-Hiroshima 739-8521 Japan)*

^e *Grad. School of Eng., Hiroshima Univer. (1-4-1 Kagamiyama, Higashi-Hiroshima 739-8527 Japan)*

Keywords: eutrophication, enclosed water bodies, environmental remediation, hydrogen sulfide, sulfate

1. Introduction

Fisheries production in the Seto Inland Sea which is largest enclosed sea in Japan reduced by half in the last 30 years. One of the reasons for the decrease is thought to be the deterioration of marine sediments. Hydrogen sulfide in eutrophic marine sediments is highly toxic to benthic organisms and may cause foul odor and blue tide. The hydrogen sulfide distribution is controlled by biogenic and abiogenic reactions such as sulfide oxidation, sulfate reduction, metal sulfide precipitation and dissolution, nucleophilic additions to organic matter, and acid base equilibria. The purposes of this study were to (1) determine directly the hydrogen sulfide concentration in marine sediment pore water using a detection tube and (2) identify sulfur species in marine sediment using XAFS instead of the complicated sequential extraction method.

2. Materials and Methods

Sediment samples were collected from Seto Inland Sea (**Fig. 1**) using an undisturbed core sampler (ϕ 11 cm, 50 cm long: HR type; Rigo) or an Ekman-Birge bottom sampler (20 cm x 20 cm; Rigo) deployed from a training and research vessel, HIKARI, of the National Institute of Technology, Hiroshima College and ONOKORO, of the Research Center for Inland Seas, Kobe University and TOYOSHIO-Maru, of Faculty of Biological Science, Hiroshima University. The collected cores were cut at every 5 cm on board. The surface sediments collected by the Ekman-Birge bottom sampler were taken from the top layer (5 cm). The sediment pore water was collected by installing a soil moisture sampler (DIK-305A; Daiki Rika Kogyo) to the sediments and the concentration of hydrogen sulfide in the pore water was measured by the detection tube (200SA or 200SB; Komyo Rikagaku Kougyo). Oxidation and reduction potential (Eh) and pH were measured by inserting each electrode to the sediments (RM-30P; DKK-TOA, C-62; AS ONE). The collected sediments were vacuum-dried at 45°C and ground using an agate made mortar. The homogenized sediment samples were stored in vacuum packs to prevent oxidation before XAFS analyses. Vertical profiles such as temperature, pH, dissolved oxygen (DO) concentration and salinity of the water column at each sampling station were also measured using multi electrodes.

Sulfur K edge XAFS spectra (ranges 2460–2490 eV) of the sediments were measured using the BL11 in the Hiroshima Synchrotron Research Center, HiSOR. The synchrotron radiation from a bending magnet was monochromatized with a Si(111) double-crystal monochromator. The sample chamber was filled with He gas, and XAFS spectra were measured by the X-ray fluorescence yield (XFY) mode using a SDD detector (XR-100SDD; AMPTEK). The X-ray energy around K edges of sulfur was calibrated with the spectra of CuSO₄ obtained with the CEY mode. The K edge main peak of sulfate was set to 2481.6 eV. The sediment samples were mounted on a double stick tape (NW-K15; Nichiban) placed in the central hole (15 mm in diameter) of a copper plate. The surface of the sample was attached to that of the copper plate. The angle between the incident X-ray and the sample surface was adjusted at 20°, and the X-ray fluorescence was detected from the direction normal to the incident beam in the plane of electron orbit of the storage ring. Concentrations of each sulfur species were calculated from total sulfur concentration proportionally divided

by each sulfur species composition. Total sulfur concentration was determined by an ICP-AES or an elemental analyzer.

3. Results and Discussion

The concentrations of hydrogen sulfide in surface sediment pore water ranged from <0.1 to 4 mg-S L^{-1} , $<0.1 \text{ mg-S L}^{-1}$, $<0.1 \text{ mg-S L}^{-1}$, <0.1 to 15 g-S L^{-1} , <0.1 to 110 mg-S L^{-1} and $<0.1 \text{ mg-S L}^{-1}$ in Hiroshima Bay (Stns. HR) Aki-Nada (Stns. AK), Hiuchi-Nada (Stn. HU), Harima-Nada (Stns. HA), Osaka Bay (Stns. OS) and Kii-Channel (Stns. KI) respectively. Sulfur species in marine sediments collected from Seto Inland Sea mainly fitted with the combination of sulfate, thiosulfate, elemental sulfur, and pyrite. Examples of the sulfur species in surface sediments collected from Seto Inland Sea in Summer or Autumn are shown in Fig. 1.

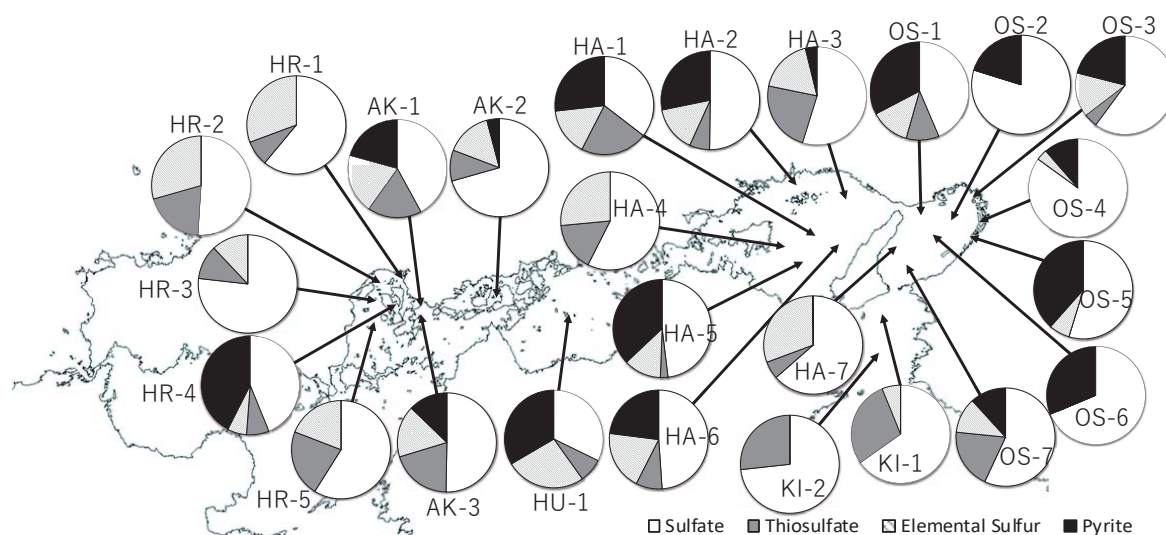


Fig. 1 Percent composition of sulfur species in surface sediments collected from Seto Inland Sea, Japan

The major sulfur species were (1) sulfate originating from seawater or oxidation of sulfur by sulfur bacteria, (2) sulfur formed by (bio) oxidation of hydrogen sulfide and (3) pyrite derived from (bio) mineralization. Pyrite was significantly identified at Osaka Bay (Stns. OS), Harima-Nada (Stns. HA-1, 2, 5 and 6), Hiuchi-Nada (Stn. 1) and Stn. HR-4 (Etajima Bay). Osaka Bay are adjacent to a big metropolitan area. The terrigenous loads from the Yodo River and Yamato River form halocline in the northern part of Osaka Bay. The Stns. HA-1, 5, 6 and HU-1 are located in the center of the Bay. The peaks of the sedimentation rate were observed at these stations due to the presence of the spiral point of the reverse flow transferring particle matter. Stn HR4 is located inside the enclosed bay called Etajima Bay where intensive oyster culture is conducted. These stations are affected by significant organic matter loads. Thus, the high flux of organic matter leads to the rapid depletion of oxygen in the sediments due to intense microbial activity. Under such anoxic conditions, sulfate-reducing bacteria (SRB) utilize sulfate as a terminal electron acceptor for the degradation of organic matter and generates hydrogen sulfide. The major pathway of pyrite formation is $\text{H}_2\text{S} \rightarrow \text{FeS} \rightarrow \text{FeS}_2$ [1]. Hence, pyrite in these stations was derived from hydrogen sulfide and iron contained in the sediments. In contrast, Sulfate and thiosulfate were dominant species near the mouth of rivers (Stns. OS-3, OS-4, HA-3, HR-1 and HR-2) because dissolved oxygen can be supplied with the estuarine circulation. Additionally, at oligotrophic areas (Stns KI and AK), sulfate and thiosulfate were also dominant species due to saturated oxygen seawater intrusion from the Pacific Ocean and Iyo-Nada, respectively.

Acknowledgements

This study was partially supported by the Environment Research and Technology Development Fund of the Ministry of the Environment, Japan (S-13) and Fund of the Hyogo Science and Technology Association in 2015. The authors show appreciation to Mr. Koji TAKEUCHI and Mr. Kazumitsu NAKAGUCHI, for piloting the research vessel.

REFERENCES

1. Rickard, D., Luther, G.W. *Chem. Rev.* **107**, 514-562 (2007).

Electrochemical desorption of stored iodide onto organo-MnO₂ and XAFS characterization

Misa KONDO^a, Masaharu NAKAYAMA^b, Alvaro MUNOZ-NOVAL^a,

Kenji KOMAGUCHI^a and Shinjiro HAYAKAWA^a

^a Graduate School of Engineering, Hiroshima University.

^b Materials Chemistry, Graduate School of Science and Engineering, Yamaguchi University

Keywords: Manganese dioxide, Hexadecylpyridinium, Iodide, insertion/desorption, XRF, XAFS

1. Introduction

Organo-MnO₂ film is a layered MnO₂ film that contains surfactants between the layers. The film can be utilized for the selective recovery of various ions. In particular, the HDPy/MnO₂ thin film that contains hexadecylpyridinium chloride (HDPy) can selectively recover iodide ions in the aqueous phase. Desorption of the stored iodide is achieved with the application of the appropriate potential, and iodine recovery cycle can be constructed¹. In this study, characterization of stored iodide was carried out with the HDPy/MnO₂ thin film. X-ray fluorescence (XRF) analysis and XAFS measurement of iodine were carried out, and the abundance of iodine in the film and the chemical state of the iodine were investigated. Information on the insertion mechanism of iodide will be utilized to optimize the capacity and efficiency of the iodine recovery cycle from seawater.

2. Materials and Methods

All electrochemical experiments were conducted using a potentiostat/galvanostat (HZ-5000, Hokuto Denko). Electrodeposition was performed in a standard three-electrode cell. A platinum mesh with a large surface area and a standard Ag/AgCl electrode (in saturated KCl) were served as the counter and reference electrodes, respectively. A commercial indium-doped tin oxide (ITO) film on the PET substrate (ITO thickness 0.1 μm) was utilized as the working electrode with the active area of 1.0 cm². A 2 mM MnSO₄ aqueous solution containing 50 mM HDPyCl was used as a deposition bath used without adding additional supporting electrolyte. To form HDPy/MnO₂ thin film a constant potential of +1.0 V was applied to the working electrode, and the thickness of the film was controlled to be 500 mC/cm². The pristine HDPy/MnO₂ thin films were immersed for 24 h in NaI solution, and the films were immersed in ultra clean water for 1 h to remove soluble impurities. Electrochemical desorption of stored iodide was carried out by applying the static potentials of +1.0 V, +1.15 V and the modulated potential around +1.15 (modulation amplitude ±0.05 V with the scan rate 100 mV/s) in 0.1 M Na₂SO₄ electrolyte.

X-ray fluorescence (XRF) analysis of iodide and iodide L₃ edge XAFS measurement (ranges 4570-4620 eV) were carried out using the BL-11 in the Hiroshima Synchrotron Research Center, HiSOR. The synchrotron radiation from a bending magnet was monochromatized with a Si(111) double-crystal monochromator. The sample chamber was filled with He gas, and XAFS spectra were measured by the X-ray fluorescence yield (XFY) mode using a SDD detector (XR-100SDD, AMPTEK). The angle between the incident X-ray and the sample surface was adjusted at 20°, and X-ray fluorescence (XRF) was detected from the direction normal to the incident beam in the plane of electron orbit of the storage ring. The amount of iodine in the HDPy/MnO₂ thin film was determined by iodine L_α intensity and a HDPy/MnO₂ thin film of known iodine abundance (0.0675 μmol/cm²) was used as a reference sample. The reference iodine compounds for XAFS analysis were I₂ pellet and KI pellet of BN matrix, KIO₃ powder and amylose-iodine complex of I₃⁻ or I₅⁻ developed by an iodine starch reaction was prepared. The incident X-ray energy was calibrated by tuning the absorption edge of the amylose-iodine complex to be 4598 eV.

3. Results and Discussion

FIGURE 1 shows the $i-t$ curve when the static potential of +1.0 V or +1.15 V vs. Ag/AgCl was applied to the thin film after iodine insertion. The integrated current for 120 s corresponded to 0.22 and 0.31 $\mu\text{mol}/\text{cm}^2$.

FIGURE 2 shows XRF spectra of iodine inserted HDPy/MnO₂ thin films before and after the application of +1.0 V or +1.15 V. The initial amount of iodine after the insertion was 0.44 and 0.65 $\mu\text{mol}/\text{cm}^2$, and they became 0.01 and 0.34 $\mu\text{mol}/\text{cm}^2$ after the potential application. The amount of iodine released was 0.43 and 0.31 $\mu\text{mol}/\text{cm}^2$.

The amounts of the iodine released and the integrated current were compared, and it was found that the two electron reaction might be took place with the application of 1.0 V while it was one electron reaction with the application of 1.15 V. This result suggests that the reaction of oxidation reaction from iodide ion to iodine molecule proceeds at +1.0 V.

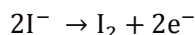


FIGURE 3 shows the iodine L₃ edge XAFS spectra of HDPy/MnO₂ thin films after iodine insertion and the application of the +1.0 V or +1.15±0.05 V. The spectral shapes were compared with those of reference iodine compounds. The inserted iodine was similar to those in amylose-iodine complex, and the iodine existed as I₃⁻ or I₅⁻. Remained iodine after the potential application showed difference depending on the applied potential. In case of applied potential of + 1.0 V, iodine remained as I₂. On the other hand, iodine existed as IO₃⁻ with the application of 1.15±0.05 V. This result suggests that the reaction of oxidation reaction from iodine molecule to iodate proceeds at +1.15 V.

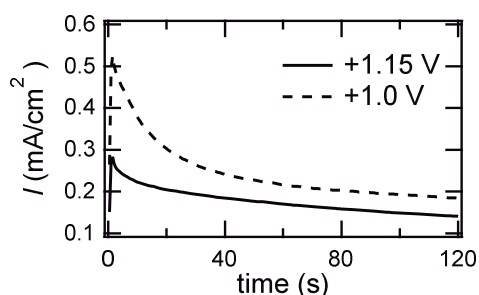


FIGURE 1. The $i-t$ curve at the time of application of potential of +1.0 V or +1.15 V.

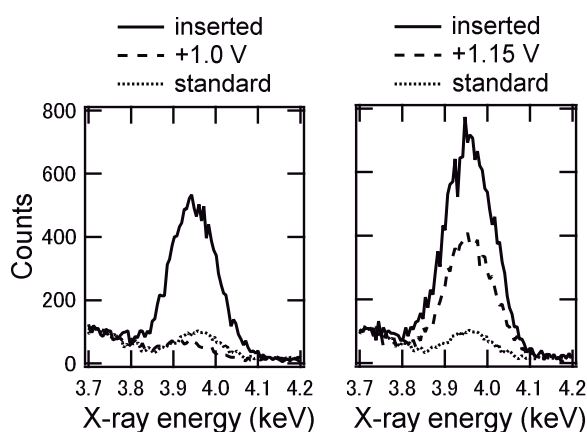


FIGURE 2. XRF spectra of HDPy/MnO₂ thin films after the application of the various potentials for desorption of the stored iodide. The incident X-ray energy was 4.62 keV, and the data acquisition time was 100 s.

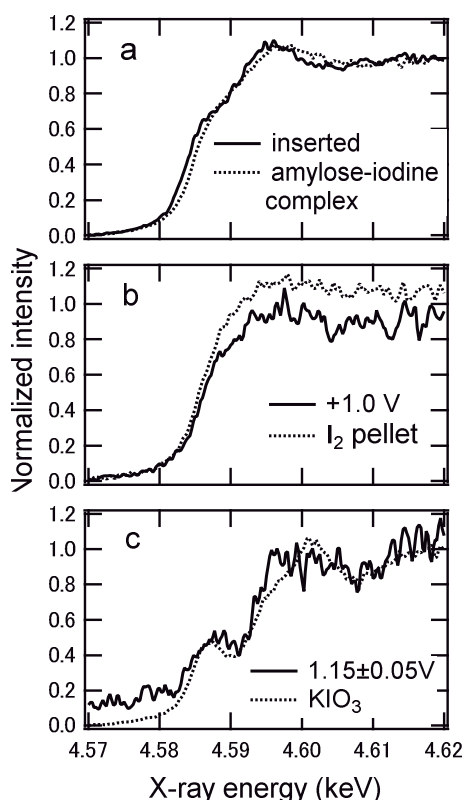


FIGURE 3. Iodide L₃ edge XAFS spectra. The residual iodide content relative to manganese is (a)60 %, (b, c)7 %.

REFERENCE

1. M. Nakayama *et al.*, *Analytica Chimica Acta*, **877**, 64-70 (2015)

Mechanism Phosphate Removal by Pyrolyzed Oyster Shell

Kyunghoi Kim^a and Shinjiro Hayakawa^b

^a*Department of Ocean Engineering, Pukyong National University, 45, Yongso-ro, Nam-Gu, Busan 48513, Republic of Korea*

^b*Graduate School of Engineering, Hiroshima University, 4-1, Kagamiyama 1 chome, Higashi-Hiroshima 739-8527, Japan*

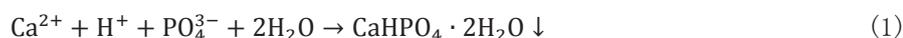
Keywords: Oyster shell, Phosphate removal, Pyrolysis

Phosphate is essential for all living things. It also plays a vital role in agricultural and industrial development. However, substantial quantities of phosphate in water bodies owing to the discharge of wastewater (as low as 0.02 mg/L) can trigger eutrophication (Conley et al., 2009; Li et al., 2016). Therefore, treatment of wastewater is required to control the concentration of phosphate before its discharge. Oyster shell is a byproduct of fisheries. Oyster shell has recently attracted interest for wastewater treatment because of its physical and chemical properties, such as calcium carbonate. Furthermore, application of a byproduct in wastewater treatment is highly desirable in terms of economic advantages. In this study, removal mechanism of phosphate with pyrolyzed oyster shell was analyzed using X-ray absorption fine structure (XAFS) analysis.

Pyrolysis is one of effective pretreatment method for recycling shells for removal of phosphate (Oladoja et al., 2015). In this study, we used oyster shells pyrolyzed at 600°C for 6 hours with diameter of 0.075-0.355 mm.

XAFS analysis (beamline BL-11 of the Hiroshima Synchrotron Research Center, HiSOR) of the *K*-edge of calcium was performed for the components contained in the initial and reacted pyrolyzed oyster shell in phosphate solution (Hayakawa et al., 2008). The standard spectra of CaHPO₄, CaO, and Ca(OH)₂ are shown in Figure 1, and curve fitting was carried out using analysis software REX2000.

The calcium *K*-edge curve of the initial pyrolyzed oyster shell has an inflection point at approximately 4050 eV, which corresponds to calcium hydroxide, which does not appear in the spectra of the reacted fly ash. This may imply that calcium hydroxide was decomposed in water to calcium ions. The curve fitting results clearly show that calcium hydrogen phosphate (CaHPO₄) formed on the surface of the reacted fly ash, whereas calcium oxide and hydroxide were hydrolyzed. The results of XAFS analysis proposed that formation of calcium hydrogen phosphate is mainly component for removal phosphate by pyrolyzed oyster shell (Xu et al., 2010).



REFERENCES

1. Conley, D.J., Paerl, H.W., Howarth, R.W., Boesch, D.F., Seitzinger, S.P., Havens, K.E., Lancelot, C., Likens, G.E., 2009. Controlling eutrophication: nitrogen and phosphorus, *Science* 323, 1014–1015.
2. Hayakawa, S., Y. Hanjima, S. Qiao, H. Namatame, T. Hirokawa(2008), Characterization of Calcium Carbonate Polymorphs with Ca K Edge X-ray Absorption Fine Structure Spectroscopy, *Analytical Science*, Vol. 24, pp. 835-837.
3. Li, R., Wang, J.J., Zhou, B., Awasthi, M.K., Ali, A., Zhang, Z., Lahori, A.H., Mahar, A., 2016. Recovery of phosphate from aqueous solution by magnesium oxide decorated magnetic biochar and its potential as phosphate-based fertilizer substitute, *Bioresour. Technol.* 215, 209–214.
4. Oladoja, N. A., R. O. A. Adelagun, A. L. Ahmad, I. A. Ololade(2015), Phosphorus recovery from aquaculture wastewater using thermally treated gastropod shell, *Process Safety and Environmental Protection*, Vol. 98, pp. 296-308.
5. Xu, D. et al., “Adsorption of Pb(II) from aqueous solution to MX-80 bentonite: effect of pH, ionic strength, foreign ions and temperature”, *Appl. Clay Sci.* 2008, 41, 37–46.

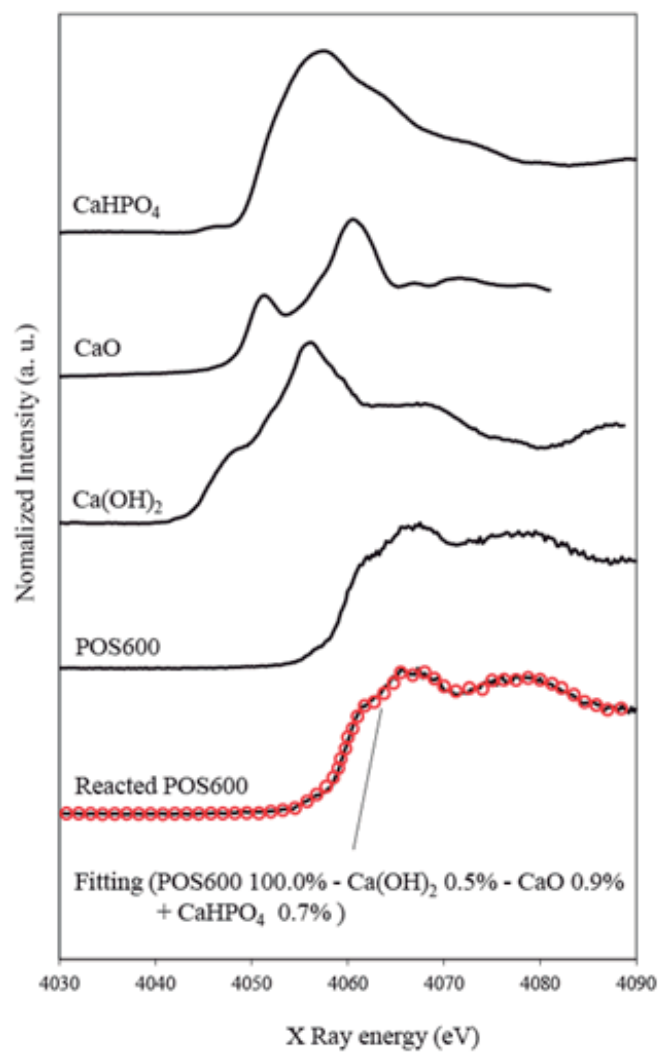


FIGURE 1. K edge XAFS spectra of pyrolyzed oyster shell with calcium standard.

Highly-Active Layered Titanosilicate Catalyst with High Surface Density of Isolated Titanium on the Accessible Interlayer Surface

Nao Tsunoji,^a Hidechika Nishida,^a Shinjiro Hayakawa,^a Masahiro Sadakane,^a and Tsuneji Sano^a

^a Department of Applied Chemistry Graduate School of Engineering, Hiroshima University,

Keywords: tianosilicate • layered silicate • olefin epoxidation • selective oxidation • titanium complex

Isolated metals or metal oxides having unusual coordination states on the solid phases often function as catalytically specific active sites.[1] Among them, tetrahedrally coordinated transition metals, especially Ti and V, covalently linked to frameworks of porous silicas (such as zeolites and mesoporous silicas) have attracted a great attention due to the specific nature of the active sites in the “metallo-silicate” catalyst showing high activity and selectivity in the partial oxidations of a wide variety of hydrocarbons using oxidants and/or photoirradiation.[2]

In contrast, because of the formation of the unusual tetrahedrally coordinated species arising from an isolation effect of the transition metals within the silica matrix, it has been difficult to obtain high surface densities of the respective isolated sites in existing solid materials. If the surface density is greatly increased, transition metal oxides with octahedral coordination are typically formed by self-condensation.

Herein, to overcome such limitations, we attempted to use a layered material based catalyst designed by using the crystalline surface of layered silicates. In this study, we immobilized Ti(IV) acetylacetonate ($\text{Ti}(\text{acac})_4$), a metal complex, onto the interlayer crystalline surface to afford a high surface density of tetrahedrally coordinated titanium species. The grafting of $\text{Ti}(\text{acac})_4$ was accomplished using the reaction of long-chain alkylammonium-exchanged layered silicate ($\text{C}_{16}\text{TMA HUS-7}$)[3] with $\text{Ti}(\text{acac})_4$, followed by the extraction of C_{16}TMA with an ethanol/hydrochloric acid solution to complete the immobilization, creating a layered titanosilicate with a relatively narrow interlayer space (HCl/Ti-HUS). However, in the previous reports[4, 5], it has been found that the narrow interlayer spaces of layered silicate catalyst limits their catalytic efficiency. Therefore, to prepare the catalyst providing larger interlayer reaction space and hence high mass-transport, grafting in low-polar solvent (toluene) containing dodecylbenzenesulfonic acid ($\text{C}_{12}\text{BSO}_3$) was also performed, yielding a catalyst with layers supported by the maintained C_{16}TMA ($\text{SO}_3/\text{Ti-HUS}$).

Figure 1 (d) shows the Ti K-edge X-ray absorption near edge structure (XANES) spectra of the titanium-incorporated layered silicates and reference compounds (anatase TiO_2 , and titanium-incorporated mesoporous silica (Ti-MCM-41)). Anatase TiO_2 exhibits broad pre-edge peaks from 4965 to 4975 eV. These peaks are assigned to the transitions from the 1s core level of the Ti atom to three different types of molecular orbitals ($1t_{1g}$, $2t_{2g}$, and $3e_g$) of TiO_2 with octahedral coordination.[6] In contrast, Ti-MCM-41 exhibits a sharp pre-edge peak at approximately 4968 eV attributed to the transition from the 1s to the 3d level of the isolated Ti atoms surrounded by four oxygen atoms.[7] Similarly, sharp pre-edge peaks were also observed in HCl/Ti-HUS and $\text{SO}_3/\text{Ti-HUS}$. These results strongly indicate that the HCl/Ti-HUS and $\text{SO}_3/\text{Ti-HUS}$ have grafted Ti species with a uniform tetrahedral coordination state. However, the Si/Ti ratios of HCl/Ti-HUS , $\text{SO}_3/\text{Ti-HUS}$, and Ti-MCM-41 were 5.8, 6.4 and 27.9, respectively, (Table 1), and the loaded amount (surface density) of titanium on the layered titanosilicates was much higher than that of Ti-MCM-41 . The contents of tetrahedrally coordinated titanium ($\text{Si/Ti} < 10$) were remarkably high compared to those ($\text{Si/Ti} = \text{ca. } 28\text{-}35$) of other zeolite and mesoporous silica based materials previously described in the literature.[8]

Tetrahedrally coordinated titanium within porous silica catalysts activates oxidants with peroxy groups that ensure efficient epoxidation of olefins. Therefore, the catalytic activities of HCl/Ti-HUS and $\text{SO}_3/\text{Ti-HUS}$ were evaluated for the oxidation of cyclohexene with tertbutyl hydroperoxide (TBHP) as an oxidant (Table 1). The reference commercial catalyst, Ti-MCM-41 , with tetrahedrally coordinated titanium yields an

epoxide product with a selectivity of 80%. In contrast, the layered titanosilicate catalyst showed higher selectivity to the epoxide products (above 90 %), confirming that the isolated and tetrahedrally coordinated Ti species act efficiently for the HCl/Ti-HUS exhibited an epoxide yield (10.4%) that was approximately two times higher than that exhibited by Ti-MCM-41 (5.7 %), although the layered titanosilicate has a remarkably low Brunauer–Emmett–Teller (BET) surface area ($14 \text{ m}^2\text{g}^{-1}$) compared to the porous Ti-MCM-41 catalyst ($544 \text{ m}^2\text{g}^{-1}$). The layered titanosilicate with a large interlayer space ($\text{SO}_3/\text{Ti-HUS}$) and also low surface area ($11 \text{ m}^2\text{g}^{-1}$) exhibited a much higher yield (16.7 %). These results reveal that effective epoxidation reactions over layered titanosilicate proceed in the interlayer space.

In conclusion, we prepared a highly active layered titanosilicate with high surface density of tetrahedrally coordinated titanium and tuned interlayer distance. In previous silica-based catalyst designs, the materials with open-pore structures and high specific surfaces have shown a potential. Here, we showed that the efficient catalytic reaction space can be related to the suitable special distribution and coordination environment of functional units that can be precisely tuned in the large interlayer space of layered silicate based material. Accordingly, the catalyst design route that we have developed has a high potential in the preparation of innovative catalysts with metal or metal oxide with unusual coordination state.

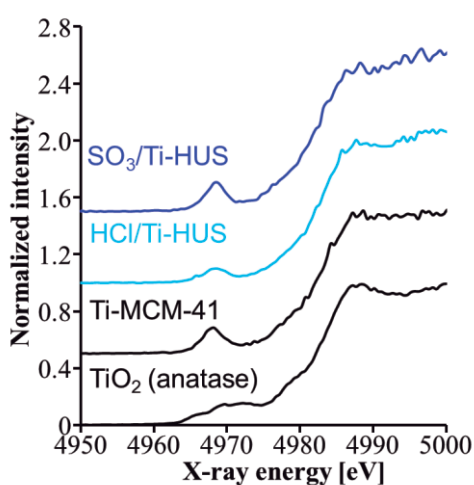


FIGURE 1. XANES spectra of layered silicate materials.

Table 1 Characteristics and catalytic performance of titanosilicate catalysts in the epoxidation of cyclohexene.

	Si/Ti ^[a]	BET area ^[b] [$\text{m}^2 \text{g}^{-1}$]	Catalytic performance ^[c]			
			Epoxide yield [%]	Epoxide selectivity [%]	Epoxide production rate [$\text{mmol g}^{-1} \text{h}^{-1}$]	TOF [$\text{mol}_{\text{cyclohexeneoxide}} \text{mol}_{\text{Ti}}^{-1} \text{h}^{-1}$]
HCl/Ti-HUS	5.8	25	10.4	97	52	32
$\text{SO}_3/\text{Ti-HUS}$	6.4	11	16.7	92	83	68
$\text{SO}_3/\text{Ti-HUS-A}^{[d]}$	6.3	26	62.9	90	314	230
Ti-MCM-41 ^[e]	27.9	544	5.7	80	29	54

^[a] Determined by ICP. ^[b] Determined by the BET method. ^[c] Reaction conditions: catalyst, 10 mg; acetonitrile, 10 mL; cyclohexene, 10 mmol; tert-butylhydroperoxide, 10 mmol; temp., 60 °C ; time, 2 h. ^[d] After three times reaction. ^[e] A reference catalyst prepared according to the previous report.^[4a]

REFERENCES

1. J. M. Thomas, R. Raja, D. W. Lewis, *Angew. Chem. Int. Ed.* **2005**, *44*, 6456-6482.
2. I. W. Arends, R. A. Sheldon, M. Wallau, U. Schuchardt, *Angew. Chem. Int. Ed.* **1997**, *36*, 1144-1163.
3. N. Tsunoji, T. Ikeda, M. Sadakane, T. Sano, *J. Mater. Chem. A* **2014**, *2*, 3372-3380.
4. N. Tsunoji, Y. Ide, Y. Yagenji, M. Sadakane, T. Sano, *ACS Appl. Mater. Interfaces* **2014**, *6*, 4616-4621.
5. N. Tsunoji, M. Bandyopadhyay, Y. Yagenji, H. Nishida, M. Sadakane, T. Sano, *Dalton Trans.* **2017**, *46*, 7441-7450.
6. Z. Liu, R. J. Davis, *J. Phys. Chem.* **1994**, *98*, 1253-1261.
7. J. M. Thomas, G. Sankar, *Acc. Chem. Res.* **2001**, *34*, 571-581.
8. W. Fan, R.-G. Duan, T. Yokoi, P. Wu, Y. Kubota, T. Tatsumi, *J. Am. Chem. Soc.* **2008**, *130*, 10150-10164.

XAFS characterization of thermal denaturation of sulfur crosslink in rubber

Takuya Mori^a, Susumu Mineoi^b, Takayuki Oshita^b, Hirotsuke Sumida^b,
Kenji Komaguchi^a and Shinjiro Hayakawa^a

^a *Department of Applied Chemistry, Graduate School of Engineering, Hiroshima University, Hiroshima, Japan*

^b *Technical Research Center, Mazda Motor Co., Hiroshima, Japan*

Keywords: rubber, thermal degradation, XAFS, sulfur K-edge

Introduction

Rubbers are used not only in tires but also in various parts of automobiles. However, functions of the rubbers and their thermal denaturation are still under investigation. X-ray absorption fine structure (XAFS) provides information on the local structure and chemical state of the element of interest, and the method is suitable for analysis of sulfur in the rubbers. S K edge XAFS spectra show peaks corresponding to the functional groups in the sample including sulfides, sulfoxides and sulfonates [1]. In this study, XAFS measurements were performed on rubbers before and after the heat treatments, and the denaturation of sulfur in the rubber would be discussed.

Experimental

Two types of isoprene rubbers were investigated. One was utilized in a series of tests for heat treatments, and the other was specially synthesized as reference rubbers of known fraction of different crosslinking length. Less components were included in the rubbers utilized in this experiment to simplify factors affecting denature of sulfur in the rubber. A typical filler (carbon black) was not used, and the sulfur species added to the rubber was sulfur powder of the vulcanizing agent and the vulcanization accelerator. Fractions of mono-sulfide, disulfide and poly-sulfides in the synthesized rubber were determined by the thiol-amine tests.

An initial series of heat treatments was conducted with the heating time of 80 h and heating temperatures of 60 °C, 80 °C, and 100 °C. The second series of tests was conducted with the heating temperature of 100 °C and the heating time of 4 h, 24 h, 48 h, and 80 h. The heat treatment for the reference rubbers were conducted with the heating temperature of 100 °C and the heating time of 24 h, 48 h and 80 h.

XAFS measurements were performed on the BL11 using a He chamber. The beamline is equipped with a Si(111) double crystal monochromator. The XAFS measurement was performed with X-ray fluorescence yield (XFY) mode using a silicon drift detector (SDD). A rubber sheet of 2 mm thick was cut into 10×10 mm² and fixed onto adhesive tape.

Spectral deconvolution of obtained XAFS spectra was performed by Gaussian curve fitting (GCF) method using ATHENA. For each S species, one Gaussian function (width setting:0.7), fixing in the energy position representing S species specific white line, and two arctangent function (width setting:0.3), fixing in the region of sulfur bridge on the low energy side and the region of the oxidized sulfur on the high energy side were fitted.

Results and Discussions

Figure 1 shows S K-edge XAFS spectra of isoprene rubbers before and after the heat treatment. The peak of sulfoxides and sulfonates were observed due to thermal denaturation when heated at 100 °C. It was found that the thermal denaturation of sulfur has critical temperature of around 100 °C, and the spectral changes of sulfoxide and sulfonate were proportion to the heating time. Beside the appearance of sulfoxides and sulfonates peaks, the decrease of the main peak intensity and higher energy shift of the peak

were also observed. They were attributed to the cleavage of the crosslinking, and the terminal of the broken bond might be oxidized to sulfonates.

Figure 2 shows XAFS spectra of reference rubbers of known fraction of different crosslinking length before the heat treatment. The clear shift of the main peak was observed, and the result was consistent with the previous report [1]. The heat treatments of these rubbers showed similar changes in Figure 1. The heated mono-sulfide rich rubber showed a decrease of the sulfide peak and an increase in the sulfonate peak.

Effects of the heat treatment to the rubber was analyzed with the GCF of the XAFS spectra. In the unheated rubber sample, only one arctangent function of the low energy side was sufficient while the additional arctangent function of high energy side was necessary for obtaining better fitting result.

Details of the fitting results and spectral determination of the fractions of different crosslinking length will be discussed.

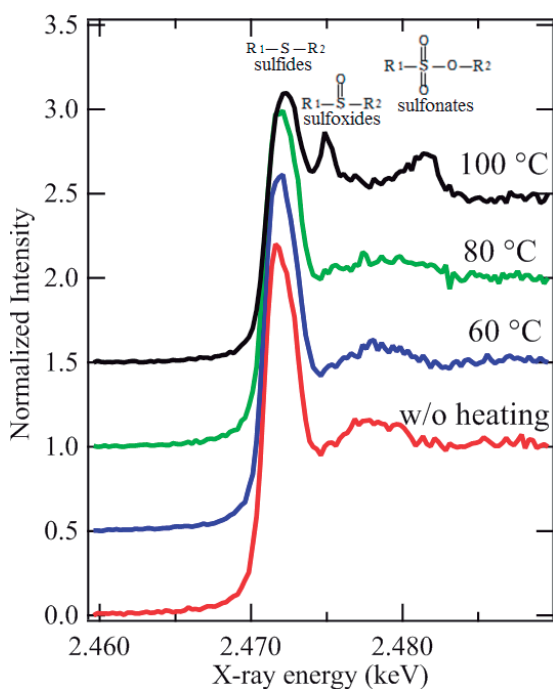


Figure 1 S K-edge XAFS spectra of isoprene rubbers treated with different heating temperatures.

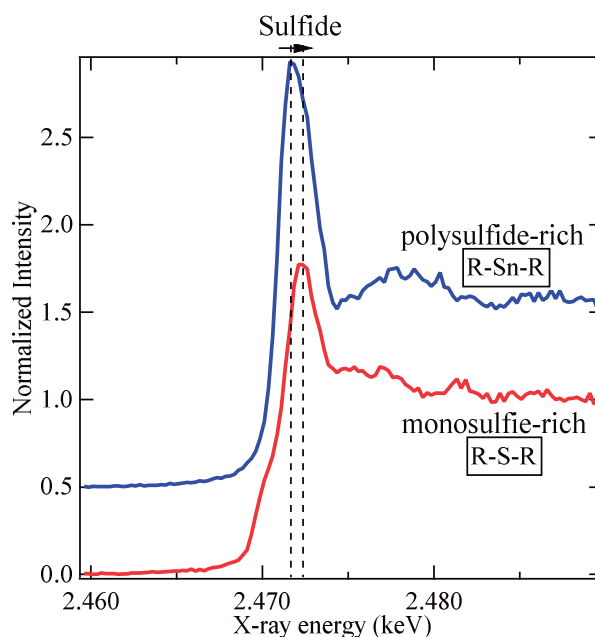


Figure 2 S K-edge XAFS spectra of mono-sulfide and polysulfide rich rubber samples

Reference

1. H. Modrow *et al.*, *Rubber Chem. Technol.*, **74**, 281-294(2001)

Depth selective and polarization dependence measurements of sulfur K edge XAFS spectra from polythiophene film under total reflection condition

Yuta Hamashima^a, Takeshi Kai^a, Kenji Komaguchi^a, Joji Ohshita^a,
and Shinjiro Hayakawa^a

a Department of Applied Chemistry, Graduate School of Engineering, Hiroshima University, Hiroshima, Japan

Keywords: XAFS, polythiophene, total reflection

Introduction

Polythiophene is one of popular conductive polymers, and the films of polythiophene and its derivatives are utilized for organic solar cells and electroluminescence (EL) devices. It is known that the orientation of a conductive polymer greatly contributes to the performance of the device, and the modification of the orientation by a substrate treatment [1] or introduction of a side chain [2] have been conducted.

Grazing incidence X-ray diffraction method is widely used to evaluate the orientation of the thin film. However, it requires a powerful and highly collimated light source. We focused on the method of evaluating the orientation of the thin film from the polarization dependence of the X-ray absorption fine structure (XAFS). Moreover, simultaneous detection of X-ray fluorescence yield (XFY) and conversion electron yield (CEY) has enabled us XAFS measurements of bulk and near surface region [3], and the significant damage to the film caused by the annealing was observed around the near surface region.

In this study, orientation and oxidation state of poly (3-hexylthiophene-2,5-diyl) thin films prepared by spin-coating and drop-casting on Si substrates were evaluated from sulfur K edge XAFS spectra.

Experimental

A 5 mg / mL solution of P3HT in o-dichlorobenzene was dropped on a Si (100) wafer, and a thin film was formed by a spin-coating (1st: 600 rpm for 3 s, 2nd: 3000 rpm for 30 s) and drop-casting. Thermal annealing (100°C, 20 min) was applied to the samples prepared by each method in air, and in a nitrogen atmosphere. In addition, the samples without annealing were also prepared.

XAFS measurement was performed at BL-11 of Hiroshima Synchrotron Radiation Center (HiSOR). At BL-11, monochromatized X-rays from 2.1 keV to 5.9 keV including S K edge energy can be used by Si (111) double crystal monochromator.

XFY and CEY can be measured simultaneously from a sample in a He filled chamber. The probing depth with the CEY method is supposed to be less than 10 nm. In order to observe the polarization dependence, ordinary arrangement [Figure 1(a)] that the angle between the electric field vector and the sample surface is 70 ° ($E \perp$ surface), and grazing incidence arrangement [Figure 1(b)] including total reflection condition were utilized. In the latter, the electric field vector and the sample surface are in the horizontal plane ($E \parallel$ surface).

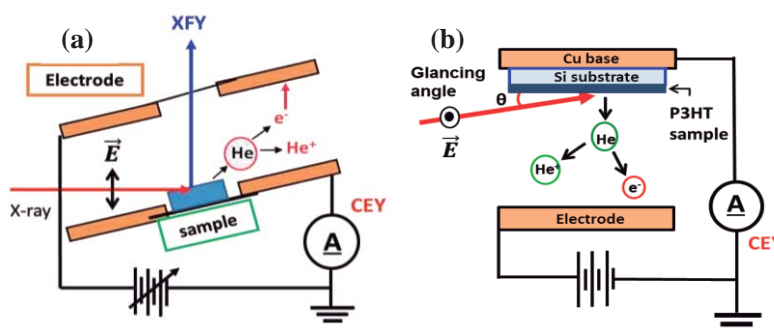


FIGURE 1. (a) conventional, (b) grazing incidence arrangements

Results and Discussion

Glancing angle of 0.7° was employed for grazing incidence arrangement. The angle is corresponding to the critical angle of total reflection for X-rays of 2490 eV on the Si surface. The critical angle was experimentally confirmed from the angle dependence of CEY from the spin-coated sample.

Polarization dependence of S K edge XAFS spectra obtained by CEY method from P3HT thin film prepared by the spin-coat and the drop-cast are shown in Figure 2. Each sample was annealed in air. According to a reference XAFS spectra of monolayer thiophene adsorbed on a substrate [4], the main peak at 2473.3 eV in the spectra obtained in the grazing incidence geometry could be assigned to the transition from S 1s to σ^*_{s-c} , and the shoulder peak that appears lower energy side of the main peak was the transition to π^* . In the spectra of the spin-coated sample, the σ^*_{s-c} peak appeared strongly in the grazing incidence arrangement. In the ordinary arrangement, the σ^*_{s-c} peak decreased, and the contribution of the π^* peak appearing in the shoulder increased. This result shows that the thiophene ring of P3HT is oriented parallel to the substrate in the spin-coated sample. XAFS spectra from drop-cast sample shows the smaller anisotropy than that of spin-coated sample owing the lower ordering of the film.

Figure 3 shows the effect of thermal annealing on the peaks ① and ② on the higher energy side of the main peak in the spectra. These peaks showed strong polarization dependence, and the dipole transition moment of those were normal to the substrate (or thiophene plane). All XAFS spectra were obtained in the conventional arrangement. Peaks ① and ② corresponded to sulfoxide and sulfonate, respectively. The drop-cast samples showed no difference around peak ① with and without the annealing While the peak ② significantly increased in sample annealed in air. For the spin-coated samples, no significant difference was observed in the XAFS spectra. It was supposed that the near surface region of the film was originally oxidized, and the oxidized region covered entire region of the spin coated film.

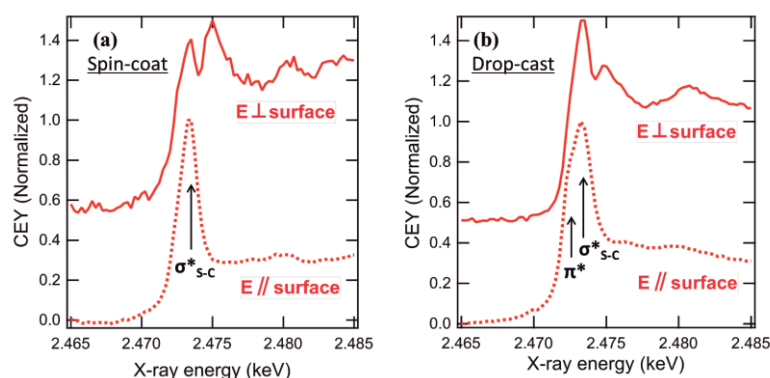


FIGURE 2. Polarization dependence of S K edge XAFS spectra from P3HT prepared by (a) spin-coating (b) drop-casting.

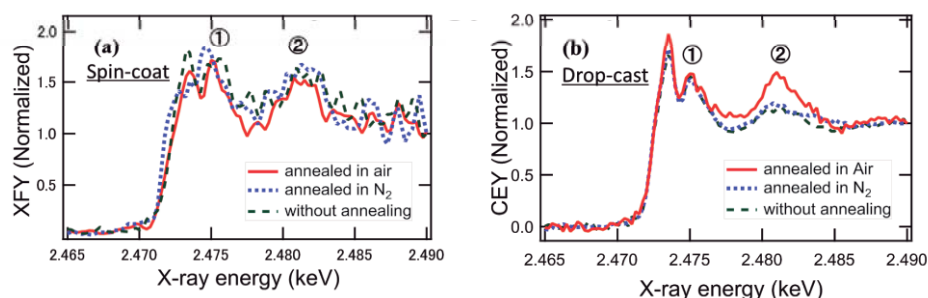


FIGURE 3. Thermal annealing condition dependence of S K edge XAFS spectra obtained from P3HT prepared in the conventional arrangement (a) spin-coating (b) drop-cast

References

1. M. Imanishi, D. Kajiya, T. Koganezawa, K. Saitow: *Sci.Rep.* **7**,5141 (2017).
2. I. Osaka, M. Saito, T. Koganezawa, K. Takimiya: *Adv. Mater.* **26**,331(2014).
3. S. Hayakawa, A. Tanaka, T. Hirokawa, *Anal Sci.* **26**,233(2010)
4. S. Terada, T. Yokoyama, M. Sakano, A. Imanishi, Y. Kitajima, M. Kiguchi, Y. Okamoto, T. Ohta, *Surf. Sci.* **414**,107(1998)

Structural Analysis of Lysine-4 Methylated Histone H3 Using VUV-CD Spectroscopy

Yudai Izumi and Koichi Matsuo

Hiroshima Synchrotron Radiation Center, Hiroshima University, Japan

Keywords: Post-translational modification, epigenetics

Enzymatic methylation and demethylation of histone H3 proteins have been reported to play substantial roles in cellular functions [1]. For example, methylation of H3 on the lysine-4 (K4) residue is considered to be associated with transcriptional activation [1]. On the other hand, since the absence of K4-methylated H3 is required for DNA methylation, defects of which are linked to serious human diseases, such as cancer [2], demethylation of methylated H3 is also essential. Since the conformation of protein closely relates to its biological function, it is important to determine the structures of (un)methylated H3 proteins in order to understand the cellular functions of (un)methylated H3 proteins more precisely. In this work, we measured circular dichroism (CD) spectra of lysine-4 (K4) mono-, di-, and trimethylated H3 and unmodified H3 proteins and predicted the secondary-structure contents and sequences.

Recombinant *Xenopus laevis* unmodified and K4 methylated H3 proteins were purchased from Merck Millipore and Active Motif, respectively. Each reagent was dissolved with 25 mM sodium phosphate buffer supplemented with 250 mM sodium fluoride (pH 8.6 at 25°C). Final concentration of each histone solution was 1 mg/ml. CD spectroscopy was carried out in the BL12 beamline at the Hiroshima Synchrotron Radiation Center in Japan. Secondary structure contents of the samples were analyzed using CD spectra and SELCON3 program [3,4]. The secondary-structure sequences were predicted using neural-network method based on CD spectroscopic results [5].

Figure 1 shows the CD spectra of K4 methylated H3. The CD spectrum of unmodified H3 reproduced from Ref. [6] is also shown in this figure. All spectra show a positive peak around 190 nm and negative peaks around 200-230 nm. CD spectral shapes reflect the secondary structure contents of proteins, which means that methylation of K4 residue induced the structural alterations of H3.

Figure 2 shows predicted secondary structure sequence of (un)methylated H3. It was predicted that the structural alterations were not limited to the regions around methylation sites. For example, α -helix formations were predicted at the 65th–69th, 80th–83rd, and 85th–86th residues in K4 mono- and dimethylated H3, although these α -helices reverted to coil structures in trimethylated H3. These global structural alterations induced by K4 methylation would contribute to epigenetic regulation *in vivo*.

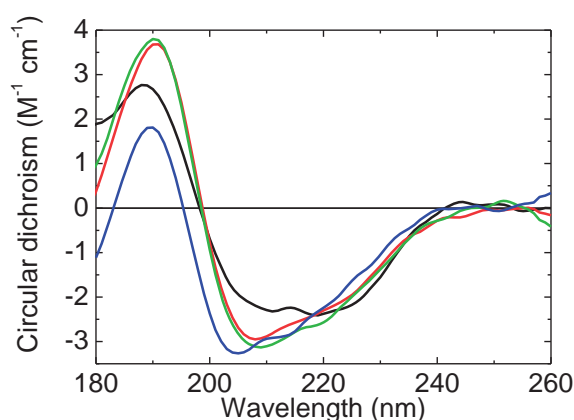


Fig. 1. CD spectra of unmodified H3 [6] (black), K4 mono- (red), di- (green), and trimethylated H3 (blue).

References

- [1] N. Mosammaparast and Y. Shi, *Annu. Rev. Biochem.* **79**, 155-179 (2010), [2] E. N. Gal-Yam *et al.*, *Annu. Rev. Med.* **59**, 267-280 (2008), [3] N. Sreerama *et al.*, *Protein Sci.* **8**, 370-380 (1999), [4] N. Sreerama and R. W. Woody, *Anal. Biochem.* **287**, 252-260 (2000), [5] K. Matsuo *et al.*, *Proteins* **73**, 104-112 (2008), [6] Y. Izumi *et al.*, *J. Radiat. Res. in press.*

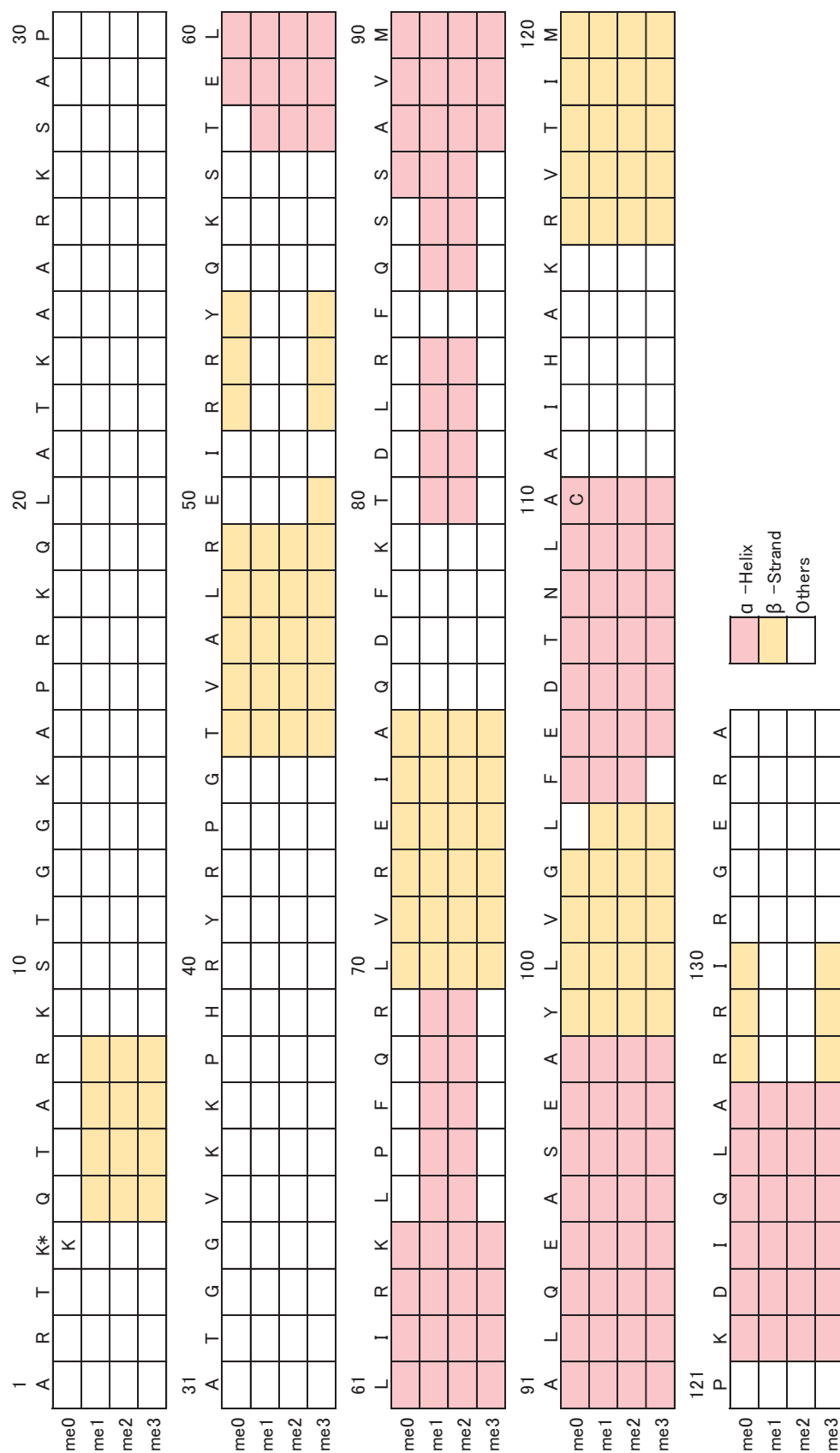


Fig. 2. Sequence-based secondary structures of unmodified (me0), mono- (me1), di- (me2), and trimethylated H3 (me3). The positions predicted formation of α -helix, β -strand/extended, and other structures are colored in pink, yellow, and white, respectively. The symbol K* in the sequence represents methylated site. The data of me0 was reproduced from Ref. [6]. The 4th and 110th residues of me0 are lysine (K) and cysteine (C), respectively, which are different from those of methylated H3 samples.

Structural Analysis of Wheat Gliadins by Vacuum Ultraviolet Circular Dichroism Spectroscopy

Reiko Urade^{a,b}, Yuki Higashino^a, Fumio Arisaka^c, Kunihiko Gekko^d,
and Koichi Matsuo^d

^aGraduate School of Agriculture, Kyoto University
Gokasho, Uji, Kyoto 611-0011 JAPAN

^bInstitute for Integrated Radiation and Nuclear Science, Kyoto University
Kumatori, Sennan-gun, Osaka 590-0405 JAPAN

^cCollege of Bioresource Sciences, Nihon University
Kamino, Fujisawa, Kanagawa 252-0880 JAPAN

^dHiroshima Synchrotron Radiation Center, Hiroshima University
Kagamiyama, Higashihiroshima Hiroshima 739-0046 JAPAN

Keywords: Wheat, Gliadin.

Wheat gluten formed from gliadin and glutenin, two major types of protein, plays a critical role in breadmaking [1-3]. Gliadin contributes to the viscosity among the rheological properties of bread dough. Gliadin is a typical monomeric prolamin protein that is soluble in 60–90% aqueous alcohol and have been believed to be insoluble in water at neutral pH. Therefore, most studies have been performed with gliadins extracted with conventional methods, which use aqueous alcohol or diluted hydrochloride solution. Recently, gliadins have been shown to be soluble in pure water, and a novel extraction method into pure water has been established [4, 5]. This has made it possible to analyze gliadins in pure water at neutral pH, and permitted the characterization of native gliadins.

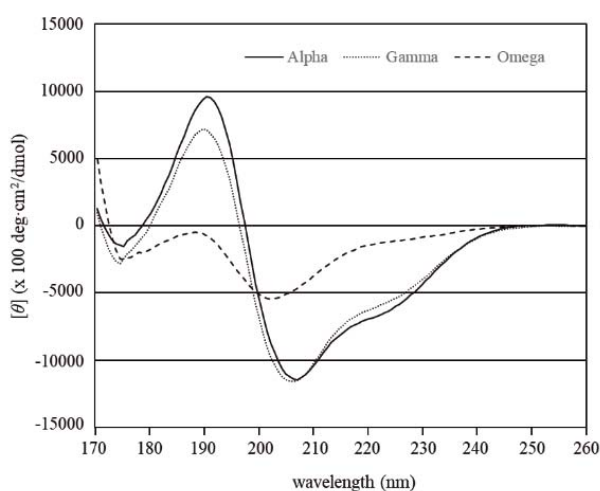


FIGURE 1. VUVCD spectra of gliadins. VUVCD experiments were performed at beamline #15 of HiSOR using a high photon flux of 1010 photon/s. CD spectra were measured using a polarization modulation technique over the wavelength range of 170–255 nm with a resolution of 1 nm.

The gliadins are large families of proteins with similar amino acid sequences. They are classified as α -, γ -, ω -gliadins, based on their amino acid sequences deduced from DNA sequences. In this study, we performed VUVCD spectroscopy analysis of α -, γ - and ω -gliadins and calculated contents of second structures of each gliadin. Alpha-, γ - and ω -gliadin were separated by ion-exchange chromatography with SP Sephadex C-50 followed by gel-filtration chromatography with SPS-C50.

Figure 1 shows the VUVCD spectra of gliadins in pure H₂O. The spectra of α -gliadin and γ -gliadin were consistent with approximately 30% and 25% of the protein being in a helical conformation, respectively. There were more β -sheet and random coil structure in the γ -gliadins (20 and 34%) than in the α -gliadins (18 and 30%). Based on structural studies with a Raman optical activity spectrum of α -gliadin, it has been predicted that the repetitive domains of the α -gliadins consist of a mixture of poly-L-proline II and β -reverse-turn structures and that the non-repetitive domains are rich in α -helical structure [6]. We studied recombinant α -gliadin synthesized in an *E. coli* system. This protein has no disulfide bonds, and had a only very small amount of α -helical structure and more random coiling (unpublished data), suggesting that the disulfide bonds formed in the C-terminal region stabilize the α -helix. The CD spectra of ω -gliadin was quite different from those of the α - and γ -gliadins. The secondary structure of the ω -gliadin was rich in β -strand and random coil structure (45 and 32%) but it apparently have little α -helix (6%).

REFERENCES

1. R. J. Hamer, F. MacRitchie, P. L. Weegels, "Structure and Functional Properties of Gluten," In *Wheat: Chemistry and Technology*, 4th ed. edited by K. Khan and P. R. Schewry, St. Paul, Minnesota, AACC International Press, 2009, pp. 153–178.
2. P. R. Schewry, R. D'Ovidio, D. Lafiandra, J. A. Jenkins, E. N. C. Mills, F. Békés, "Wheat Grain Proteins," In *Wheat: Chemistry and Technology*, 4th ed. edited by K. Khan and P. R. Schewry, St. Paul, Minnesota, AACC International Press, 2009, pp. 223–298.
3. M. Cornec, Y. Popineau, J. Lefebvre, *J Cereal Sci* **19**, 131–139 (1994).
4. T. Ukai, Y. Matsumura, R. Urade, *J Agric Food Chem* **56**, 1122–1130 (2008).
5. N. Sato, A. Matsumiya, Y. Higashino, S. Funaki, Y. Kitao, Y. Oba, R. Inoue, F. Arisaka, M. Sugiyama, R. Urade, *J Agric Food Chem* **63**, 8715–8721 (2015).
6. E. W. Blanch, D. D. Kasarda, L. Hecht, K. Nielsen, L. D. Barron, *Biochemistry* **42**, 5665–5673 (2003).

Conformations of Myelin Basic Protein Interacted with Membrane Revealed by Vacuum-Ultraviolet Circular-Dichroism Spectroscopy

Munehiro Kumashiro^a, Yudai Izumi^b, and Koichi Matsuo^b

^a*Department of Physical Science, Graduate School of Science, Hiroshima University, 1-3-1 Kagamiyama, Higashi-Hiroshima, Hiroshima 739-8526, Japan*

^b*Hiroshima Synchrotron Radiation Center, Hiroshima University, 2-313 Kagamiyama, Higashi-Hiroshima, Hiroshima 739-0046, Japan*

Keywords: liposome; myelin basic protein; protein-membrane interaction; synchrotron-radiation circular-dichroism.

Myelin basic protein (MBP) is the second most abundant protein in the myelin sheath of central nervous system which is a unique multilayered membrane surrounding the axon of neuron cell [1]. It is believed that MBP is located between the membrane layers and physically interacts with them, leading to the compactness of the multilayered structure [2]. However, the MBP conformation interacting with membrane and its interaction mechanism remain unclear. In this study, to characterize the conformation of membrane-bound MBP, we measured the vacuum-ultraviolet circular-dichroism (VUVCD) spectra of MBP in the presence of various types of phospholipid liposomes related to myelin membrane (phosphatidylethanolamine: PE, phosphatidylcholine: PC, sphingomyelin: SM, phosphatidylserine: PS, phosphatidylinositol: PI, phosphatidylinositol 4-phosphate: PIP, phosphatidylinositol 4,5-bisphosphate: PIP₂) and discussed the mechanism of MBP-membrane interactions.

Native MBP exhibited a large negative CD peak around 200 nm, which is a characteristic peak of the unordered structure. This spectrum did not change when adding PE, PC, and SM liposomes, meaning that there are no structural changes due to the interaction with these liposomes. On the other hand, the spectra of MBP in the presence of PS, PI, PIP, and PIP₂ liposomes showed two negative peaks around 208 and 222 nm, and a positive peak around 193 nm, suggesting that these liposomes induce the helical structures of MBP. The VUVCD analyses [3, 4] and Eisenberg plot analyses [5] showed that MBP with these liposomes formed positively charged helix regions on the amino-acid sequence, which were mostly assigned to the coil, namely turn and unordered, structures in the native state. Since the net charges of head groups in the PS, PI, PIP, and PIP₂ phospholipid molecules are negative while those in PE, PC, and SM phospholipid molecules are neutral, MBP could interact with membrane mainly via the electrostatic interaction. The interactions would induce the formation of helical structures in the MBP. Further, MBP with PIP₂ liposome formed hydrophobic helix regions on the amino-acid sequence, which were mostly assigned to the β -strands in the native state. These results suggest that MBP could interact with PIP₂ liposome not only via the electrostatic interaction but also via hydrophobic interaction and the phosphorylation of PI phospholipid molecules may enhance stable membrane binding of MBP.

REFERENCES

1. J. M. Boggs., *Cell. Mol. Life Sci.*, **63**, 2006, pp. 1945-1961
2. P. Riccio, A. Fasano, N. Borenshtein, T. Bleve -Zacheo, and D.A. Kirschner, *J Neurosci. Res.*, **59**, 2000, pp. 513-5213.
3. K. Matsuo, R. Yonehara, and K. Gekko, *J. Biochem.*, **138**, 2005, pp. 79-88
4. K. Matsuo, H. Watanabe, and K. Gekko, *Proteins*, **73**, 2008, pp. 104-112
5. R. Gautier, D. Douguet, B. Antonny, and G. Drin., *Bioinformatics*, **24**, 2008, pp. 2101-2102

A Preliminary Study of Vacuum-Ultraviolet Circular Dichroism of Hydroxypropyl Cellulose

Yasuyuki Maki^a and Koichi Matsuo^b

^a*Department of Chemistry, Faculty of Science, Kyushu University, Fukuoka 819-0395*

^b*Hiroshima Synchrotron Radiation Center, Hiroshima University, Higashi-Hiroshima 739-8526*

Keywords: Polysaccharide, Cellulose derivative, Vacuum-ultraviolet circular dichroism.

Hydroxypropyl cellulose (HPC) is a water-soluble, non-toxic cellulose derivative, which is allowed for use in pharmaceutical products and food additives. In the production of HPC, the three available hydroxyl groups on a D-glucosyl residue of native cellulose are substituted by side chains containing a variable number of hydroxypropoxy groups [1]. Rheological properties and phase behaviors of aqueous HPC solutions are associated with conformation of HPC chains. Vacuum-ultraviolet circular dichroism (VUVCD) spectroscopy is an effective tool for analyzing saccharide structure in aqueous solution because they contain high-energy chromophores such as hydroxyl groups and acetal bonds whose electronic transitions are only detectable in the vacuum-ultraviolet (VUV) region below 190 nm [2]. In this preliminary study, a VUVCD spectrum of HPC in aqueous solution was measured using a VUVCD spectrophotometer with a synchrotron radiation light source.

In this experiment, commercially available HPC (Wako Pure Chemical Industries, Catalog number 082-07925) was used without further purification. The sample solutions were prepared by dissolving HPC in de-ionized water at concentrations of 5.0 and 10 wt%. The VUVCD spectra were measured from 220 to 167 nm at 25 °C under a nitrogen atmosphere using the SR-VUVCD spectrophotometer of Hiroshima Synchrotron Radiation Center (BL-12) [3,4]. The path length l of the CaF₂ optical cell was adjusted using a Teflon spacer of 10 μm or 50 μm. The measurements without spacers were also performed in order to reduce the absorption of light by water at low wavelengths. The spectra obtained without the spacers were calibrated by normalizing the ellipticities θ to the spectra measured using the spacers in the overlapping wavelength region.

The degree of polymerization (DP) of the HPC sample was not given by the manufacturer, so it was roughly estimated as follows. According to the manufacturer, viscosity of 2 wt% aqueous solution of the HPC sample at 20 °C ranges from 2.0 to 2.9 mPa s. If we tentatively use a “universal” relationship between viscosity and concentration for non-entangled solutions of random coil polysaccharides [5], $\eta \approx \eta_s \{1.5(c[\eta])^{1.4} + 1\}$, where η , η_s , $[\eta]$, c are the viscosity of the polymer solution, the viscosity of the solvent, the intrinsic viscosity, and the polymer concentration, respectively, $[\eta]$ of the HPC sample was estimated to be $(4\text{--}6) \times 10^1 \text{ cm}^3/\text{g}$. Using the Mark-Houwink equation for HPC in water [6], $[\eta] = (4.2 \times 10^{-2})M^{0.68}$, where M is the molecular weight of HPC, M is calculated to be $(2\text{--}4) \times 10^4$. A molar substitution (MS), the average number of hydroxypropyl substituent per anhydroglucose residue, depends on the conditions of hydroxypropylation, and is larger than 4 for typical commercial samples [1]. If we assume MS = 4 as the most probable value [7], the molecular weight M_0 of the structural unit was calculated to be 394. Thus, the DP of the HPC sample was estimated to be between 6×10^1 and 1×10^2 .

Figure 1(a) shows the VUVCD spectra of aqueous HPC solutions at 5.0 and 10 wt%. The CD spectra were observed only in the VUV region below 190 nm, exhibiting a positive peak around 177 nm.

In Figure 1(b), the VUVCD spectra in Fig. 1 were re-expressed in the form of molar ellipticity $[\theta]$ calculated using the estimated value $M_0 = 394$ of the structure unit. The spectra of different concentrations coincide well within experimental error, indicating no concentration dependence on the HPC structure.

It is interesting to compare the VUVCD spectrum of HPC with that of unsubstituted cellulose. However, cellulose, a polysaccharide consisting of β -(1,4)-linked D-glucose units, is relatively insoluble in aqueous solution. In a recent study [2], the VUVCD spectra of oligo-(1,4)- β -D-glucan of DP = 2 (cellobiose), 3

(cellotriase), and 4 (cellotetraose) in aqueous solutions were measured, although the cello-oligosaccharides above DP = 5 were insoluble. The VUVCD spectra of the cello-oligosaccharide had one positive peak around 174 nm and the peak intensity decreased as the DP increased [2]. Figure 2 compares the VUVCD spectra of HPC with those of cello-oligosaccharides [2], indicating that a positive peak in HPC was red-shifted by around 3 nm with respect to that in cello-oligosaccharides and that the peak intensity of HPC (DP is between 6×10^1 and 1×10^2) was much smaller than those of cello-oligosaccharides. The deviation in the spectra between HPC and the unsubstituted oligo-(1,4)- β -glucan is attributed to the effect of hydroxypropoxy groups on HPC. Another possible reason for the deviation is the large difference in the chain length, because the VUVCD spectra of oligosaccharides such as oligo-(1,4)- α -glucan (malto-oligosaccharide) and oligo-(1,3)- β -glucan (laminari-oligosaccharide) varied with the chain length [2].

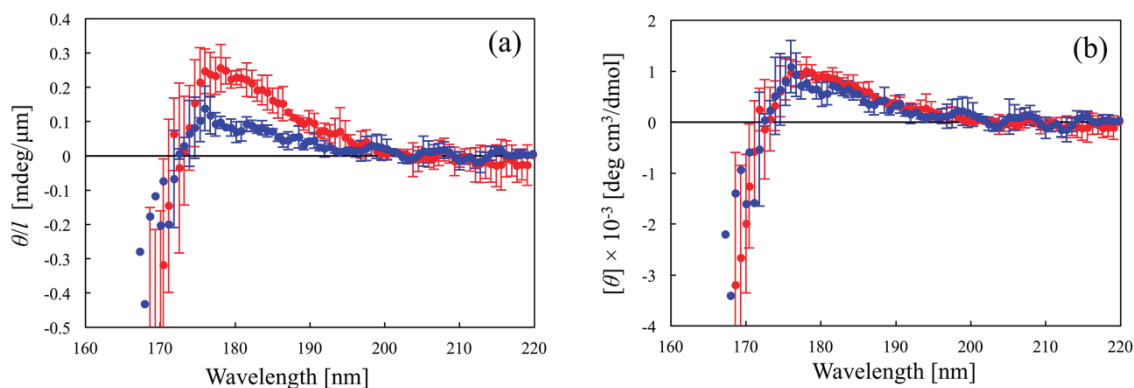


FIGURE 1. VUVCD spectra of HPC in aqueous solutions at concentrations of 5.0 wt% (●) and 10 wt% (●) at 25 °C.

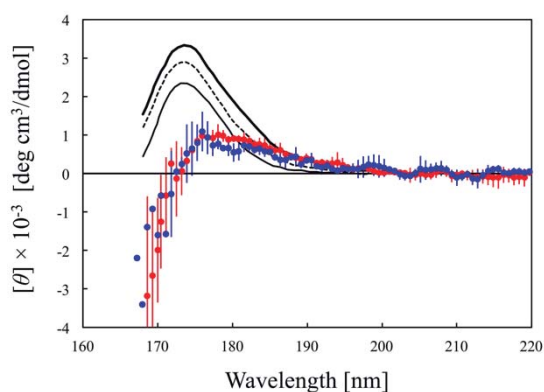


FIGURE 2. VUVCD spectra of HPC in aqueous solutions at concentrations of 5.0 wt% (●) and 10 wt% (●) at 25 °C. Thick solid, dashed, and thin solid lines represent the VUVCD spectra of cello-oligosaccharides of DP = 2 (cellobiose), 3 (cellotriase) and 4 (cellotetraose), respectively [2].

REFERENCES

1. S. Fortin and G. Charlet, *Macromolecules* **22**, 2286-2292 (1989).
2. K. Matsuo, *Biomed. Spectrosc. Imaging* **6**, 111-121 (2017).
3. K. Matsuo, K. Sakai, Y. Matsushima, T. Fukuyama and K. Gekko, *Anal. Sci.* **19**, 129-132 (2003).
4. N. Ojima, K. Sakai, K. Matsuo, T. Matsui, T. Fukazawa, H. Namatame, M. Taniguchi and K. Gekko, *Chem. Lett.* **30**, 522-523 (2001).
5. E. R. Morris, A. N. Cutler, S. B. Ross-Murphy, D. A. Rees and J. Price, *Carbohydr. Polym.* **1**, 5-21 (1981).
6. W. M. Kulicke, C. Clasen and C. Lohman, *Macromol. Symp.* **223**, 151-174 (2005).
7. D. G. Coffey, D. A. Bell and A. Henderson, "Cellulose and Cellulose Derivatives," in *Food Polysaccharides and Their Applications*, by A. M. Stephen, G. O. Phillips and P. A. Williams, Boca Raton: CRC Press, 2006, pp. 147-180.

Characterizations of Structural Dynamics and Hydration Structures of D-Glucose using Vacuum-Ultraviolet Circular-Dichroism Spectroscopy

Koichi Matsuo, H. Namatame, M. Taniguchi

Hiroshima Synchrotron Radiation Center, Hiroshima University, Higashi-Hiroshima, 739-0046, Japan

Keywords: Molecular dynamics, Solution structure, Time-dependent density functional theory

Structural dynamics and hydration structures of saccharides are crucial for understanding their biological functions such as the molecular recognition and stabilization of biomolecule structures. However, saccharides take complicated equilibrium conformations among the gauche-trans (GT), GG, and TG rotamers of hydroxymethyl group at C-5 and between the α - and β -anomer configurations of hydroxy group at C-1 in aqueous solution, which impedes the characterizations of their structures. Vacuum-ultraviolet circular dichroism (VUVCD) using a synchrotron radiation is very sensitive to the saccharide structures because it can detect the high-energy chromophores such as hydroxy group and acetal bond. Recently the analytical techniques of the monosaccharide spectra have been largely developed by the combination with theoretical analysis such as molecular dynamics (MD) simulation and time-dependent density functional theory (TDDFT), which allowed us to obtain their complicated structures such as the structural dynamics and hydration structures [1-3]. In this study, the VUVCD spectrum of D-glucose experimentally measured down to 163 nm was theoretically calculated to characterize its complicated structures in solution.

The VUVCD spectrum of D-glucose exhibited one positive peak around 170 nm, reflecting the equilibrium structures (α -GT, α -GG, α -TG, β -GT, β -GG, and β -TG conformers) [4]. The structures of these conformers were simulated by the MD method in solution and their theoretical spectra were calculated from the respective simulated structures by TDDFT method. A linear combination of the CD spectra of the six conformers, produced a D-glucose spectrum similar to that observed experimentally, disclosing that the GT and GG rotamers show negative and positive CD around 170 nm, respectively, and that the α - and β -anomers exhibit negative and positive CD around 160 nm, respectively. These pairwise relationships between CD and structures were very consistent with those obtained in methyl α - and β -D-glucopyranosides [2, 3]. Further, the structural dynamics of six conformers in solutions were largely different each other, depending on their unique configurations of hydroxymethyl group at C-5 (GT, GG, and TG rotamers) and hydroxy group at C-1 (α - and β -anomers). We also found that the differences in the structural dynamics of six conformers affected the intramolecular hydrogen bonds around the ring oxygen and the hydroxy oxygen at C-1, and that the numbers of water molecules exhibiting intermolecular hydrogen bonds (the degree of hydration) with solutes were larger in β -anomer configuration than in α -anomer one. These results indicate that the intra- and intermolecular hydrogen bonds play important roles for determining the solution structures of monosaccharides, affecting their CD spectra.

References

1. Kanematsu, Y.; Kamiya, Y.; Matsuo, K.; Gekko, K.; Kato, K.; Tachikawa, M. *Sci. Rep.*, **2016**, *5*, 17900.
2. Matsuo, K.; Namatame, H.; Taniguchi, M.; Gekko, K. *Biomedical Spectroscopy and Imaging*, **2015**, *4*, 269.
3. Matsuo, K.; Namatame, H.; Taniguchi, M.; Gekko, K. *J. Phys. Chem. A*, **2012**, *40*, 9996.
4. Matsuo, K.; Gekko, K. *Carbohydr. Res.*, **2004**, *339*, 591.

Secondary structural analysis of XRCC4 protein using HiSOR-VUVCD

Kai Nishikubo^{a,b}, Yudai Izumi^c, Kentaro Fujii^b, Koichi Matsuo^c,
Yoshihisa Matsumoto^d, Akinari Yokoya^b

^a*Graduate School of Science and Engineering, Ibaraki University, Japan*

^b*Quantum Beam Science Research Directorate, National Institutes for Quantum and
Radiological Science and Technology (QST), Japan*

^c*Hiroshima Synchrotron Radiation Center, Hiroshima University, Japan*

^d*Tokyo Institute of Technology*

Keywords: XRCC4, vacuum ultraviolet circular dichroism

Activation or inactivation of proteins is regulated by undergoing phosphorylation of certain amino acid residues. XRCC4 also undergoes phosphorylation of its several sites by DNA-PK in the DNA double strand break repair pathway (NHEJ) (1). The phosphorylation might cause a change of static electric charge at the amino acid residues, resulting conformational alteration of the whole protein structure to permit the protein accessibility to the strand break terminus through the charge re-distribution in the protein. In order to understand the role of XRCC4 properly, it will be necessary to understand the mutual relationship between its structural change and activity change. So far, crystal structure analysis of XRCC4 has been performed, but there is no data on the full-length of XRCC4 because of difficulty of crystallization of about 100 residues in the C-terminal which includes several targets of phosphorylation. Instead of crystallography, we have applied circular dichroism (CD) spectral analysis in a vacuum UV region at HiSOR. CD spectral analysis allows us to analyze the full-length of the protein structure because we can measure in an aqueous solution. For the first step, we performed CD spectral analysis of unmodified full-length XRCC4. CD spectral data suggests that the relative fraction of the turn structure is significantly larger than that reported by the crystallography. The evidence shows that structural aspects of the full length of the proteins are important to understand the conformational changes of the phosphorylation and their roles in DNA repair processes.

Figure 1 shows VUV-CD spectra of full-length XRCC4. A positive peak at 190 nm and negative peak at around 208 nm are the characteristic CD peaks of α -helix structures (2).

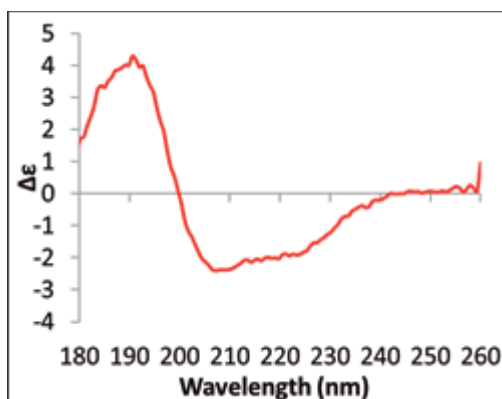


FIGURE 1. VUV-CD spectra of full-length XRCC4 in an aqueous solution.

TABLE 1. Secondary structural contents of XRCC4

Structure Content (%)	1FU1 ⁽³⁾	HiSOR
α -Helix	38	37
β -Strand	26	15
Turn	8	22
Unordered	28	26
Length (residues)	203	336

In table 1, 1FU1 is previously reported from crystallography (3), and HiSOR is the result of CD measurement at HiSOR.

REFERENCES

1. Kamdar, R.P. and Matsumoto, Y. Radiation-induced XRCC4 Association with Chromatin DNA Analyzed by Biochemical Fractionation. *J. Radiat. Res* 2010; 51, 303-313.
2. Matsuo, K. Structural analysis of protein using synchrotron radiation vacuum-ultraviolet circular dichroism. *The Journal of Biochemistry* 2004 135, 3, p. 405-411.
3. Junop, M.S., Modesti, M., Guarne, A., Ghirlando, R., Gellert, M., Yang, W. Crystal structure of the Xrcc4 DNA repair protein and implications for end joining. *EMBO J* 2010. 19: 5962-5970.

Structural Analysis of Lysozyme by using VUVCD Spectroscopy

Takayasu Kawasaki^a, Yudai Izumi^b, Koichi Tsukiyama^a, and Koichi Matsuo^b

^a*Infrared Free Electron Laser Research Center, Tokyo University of Science,
2641 Yamazaki, Noda, Chiba 278-8510, Japan*

^b*Hiroshima Synchrotron Radiation Center, Hiroshima University, 2-313 Kagamiyama, Higashi-Hiroshima,
Hiroshima 739-0046, Japan*

Keywords: Infrared free electron laser, lysozyme, VUVCD, amyloid.

Mid-infrared free-electron laser (FEL) is a synchrotron-radiation based coherent laser light that is generated by an accelerated electron beam as a light source [1]. Its oscillation wavelengths are tunable within the mid-infrared region from 5 to 10 μm , and various resonant wavelengths for stretch vibrational modes of C=O, C-O, C=C, and C-N bonds, and bending vibrational modes of N-H, C-H, and O-H bonds are contained in this region. We previously found that the FEL tuned to wavelengths 6.1-6.2 μm (1666-1639 cm^{-1}) that correspond to the amide I band ($\nu_{\text{C=O}}$) can dissociate amyloid-like aggregate of hen egg white lysozyme (HEWL) to the non-aggregate form in aqueous solution [2]. Amyloid-like aggregate of HEWL is string-like fibrils that have a width of several nano-meters and a length of several micro-meters, and many hydrogen bonds are formed in the stacking cavity of the fibril state. Interestingly, the peptide bonds are not hydrolyzed by the irradiation to the amide bonds as shown by gel electrophoresis, and the renatured lysozyme after the laser irradiation did not possess full enzymatic activity against the bacterial cell wall extract.

In this study, we employed a vacuum-ultraviolet circular-dichroism (VUV-CD) spectroscopy for analysis of the protein conformational change after the FEL irradiation. The secondary structure analysis using SELCON program [3, 4] estimated that contents (%) of protein secondary structures were changed by the irradiation as follows: 38.3 \pm 5.0 (native) \rightarrow 33.5 \pm 1.4 (after irradiation) in α -helices; 10.5 \pm 3.4 (native) \rightarrow 16.8 \pm 1.8 (after irradiation) in β -strands; 24.5 \pm 3.9 (native) \rightarrow 22.9 \pm 1.6 (after irradiation) in turns; 25.3 \pm 3.7 (native) \rightarrow 26.8 \pm 1.2 (after irradiation) in random structures. Among these changes in secondary structure contents, remarkable differences between the native HEWL and the irradiated one are the decrease of α -helix content and the increase of β -strand content.

Figure 1 shows a secondary structure map of α -helix (dark gray), β -strand (light gray), and other structures (white) upon amino acid sequence (based on the literature [5]) of non-treated lysozyme (4-b-1) and that after irradiation at amid I band (4-b-2), which were estimated by a neural-network method. Focusing on the amino acid sequences around catalytic residues (E35 and D52), the secondary structural changes are as follows: α -helix was changed to β -strand with other structures in the segment L25-F34, the other structures were changed to α -helix in the segment S36-T40, and α -helix was changed to β -strand with other structures in the segment Y53-I58.

We evaluated these secondary structural changes in the active site as follows:

- 1) The two carboxyl groups on catalytic residues (E35 and D52) have important roles in hydrolysis reaction of a glycoside bond of the substrate. Therefore, it can be estimated that the peptide chains around those catalytic residues are exposed to the surrounding space to bind the substrate and can be easily affected by the intense infrared radiation.
- 2) Another noteworthy result is the structural change of the core region containing W62 for fibrillation: β -strand consisted by W63 and C64 was changed to other structures by the irradiation. In the enzyme-ligand complex structure [6], two tryptophan residues (W62 and W63) are located close to the ligand via hydrophobic interactions between the indole rings and carbohydrate rings. W62 also acts as a contact surface in the fibril formation. The amyloid fibrillation and β -sheet formation is triggered by

Optical Activity Emergence in Amino-Acid Thin Films by Circularly-polarized Light Irradiation

Jun-ichi Takahashi^a, Yudai Izumi^b, Koichi Matsuo^b, Masaki Fujimoto^c,
Masahiro Katoh^c, Yoko Kebukawa^a, Kensei Kobayashi^a

^a*Faculty of Engineering, Yokohama National University, 79-5, Tokiwadai, Hodogaya,
Yokohama 250-8501, Japan*

^b*Hiroshima Synchrotron Radiation Center, Hiroshima University, 2-313 Kagamiyama,
Higashi-Hiroshima 739-0046, Japan*

^c*UVSOR Facility, Institute for Molecular Science, 38 Nishigo-Naka, Myodaiji,
Okazaki 444-8585, Japan*

Keywords: Homochirality, Amino Acid, Optical Activity, Circularly-polarized Light, Circular Dichroism.

The origin of homochirality in terrestrial bioorganic compounds (L-amino acid and D-sugar dominant) remains one of the unresolved problems in the research for the origins of life. Because organic compounds synthesized in abiotic circumstances are intrinsically achiral racemic mixtures (equal amounts of L- and D-bodies), it is hypothesized that chiral products were originated from asymmetric reactions on surfaces of interstellar dusts or meteorites. These types of asymmetric reactions could have been derived from physically asymmetric excitation sources, that is “chiral radiation”, in space. The chiral space products would have been transformed into the complex organic materials (including amino-acid precursor molecules) and transported to primitive Earth resulting in terrestrial biological homochirality (Cosmic Scenario) [1].

Eventually, circularly-polarized light (CPL) in space originated by light scattering from interstellar dust clouds in star formation regions have been observed as one of the potential candidates for “chiral radiation” sustaining the relevance of Cosmic Scenario [2].

Several ground experiments to validate this scenario have been investigated asymmetric photochemical reactions in simple biochemical molecules using CPL radiation from high-energy accelerators. We have reported optical activity emergence in solid-phase films of racemic mixtures of amino acids by CPL irradiation of 215 nm in wavelength from free electron laser (FEL) of UVSOR-II [3]. By use of circular dichroism (CD) spectrometer, it has been suggested that the left- and right-handed CPL (LCPL and RCPL) caused the preferential conformational changes between the two enantiomers in racemic amino acid films.

CD spectroscopy can easily detect the emergence of optical anisotropy due to the asymmetric reaction because it sensitively reflects the steric structures of chiral molecules such as amino acids. The theoretical calculation of CD spectrum of L-alanine molecule revealed that the chromophores such as carboxyl and amino groups had many characteristic electronic transitions ($n-\pi^*$, $\pi-\pi^*$, and $n-\sigma^*$) below 230 nm [4], suggesting that the photochemical reaction might depend on the irradiation photon energy. Recently, we carried out the measurement of CPL wavelength dependence of optical activity emergence at undulator beam line BL1U of UVSOR-III by tuning undulator gap conditions. As for the sample, we formed thin solid films of racemic DL-alanine on quartz substrates from crystal powders of DL-alanine (L/D = 50/50) as a sublimation source by using a thermal-crucible vacuum-evaporation system in Hiroshima Synchrotron Radiation Center (HiSOR). Sublimation temperature was controlled in the range of 150~200°C and pressure of the vacuum chamber was approximately 5×10^{-2} Pa throughout the evaporation process. The CD spectra of thin solid films just after the deposition were measured from 260 to 170 nm in wavelength using a vacuum-ultraviolet (VUV) CD instrument at beam line BL-12 of HiSOR and confirmed to be mostly zero before the irradiation, showing that the spurious CD due to the contamination of film surface were negligible.

In this study, three wavelengths of LCPL and RCPL (230, 215, and 202 nm) introduced from the undulator beam line BL1U and measured the CD spectra to clarify the optical activity of the films after the CPL irradiation

at beam line BL-12 of HiSOR. In order to delete the effects of linear dichroism (LD) and/or linear birefringence (LB) components, dependence on sample rotation angle (0, 45, 90, and 135 degrees) of the CD spectra was measured. The wavelength dependence of optical activity emergence by CPL irradiation of 230, 215, and 202 nm in wavelength has been reported [5,6]. The LCPL and RCPL irradiation exhibited symmetrically inverted spectra in the irradiation wavelengths (230, 215, and 202 nm), indicating the emergence of optical activity at the irradiation wavelengths. Further, the spectral shapes observed were largely different from each other suggesting that the asymmetric reactions of DL-alanine film depend on the irradiation wavelength.

To further validate these results, we are presently trying to introduce optical activity by VUV-CPL irradiation in shorter wavelength than 200 nm. The DL-alanine samples were set in a vacuum sample chamber preventing VUV-CPL attenuation by air absorption in shorter wavelength than 200 nm (Fig.1). On the beam entrance side of the vacuum sample chamber, a gate valve with a vacuum-sealed MgF₂ window was mounted. The irradiated CPL wavelengths were 180, 155, and 120 nm corresponding to photon absorption bands of alanine molecule [7]. The irradiated photon number was measured with photoelectron current of a silicon photodiode (International Radiation Detectors, Inc.) settled at the sample position. The typical energy dose calibrated by using quantum efficiency data of the silicon photodiode was approximately 50 mWh. Detailed analysis of SR-CD spectra at BL-12 of HiSOR, we are aiming to clarify full mechanism of the optical activity emergence, which potentially has relevance to the origin of terrestrial biological homochirality stimulated by “chiral radiation”.

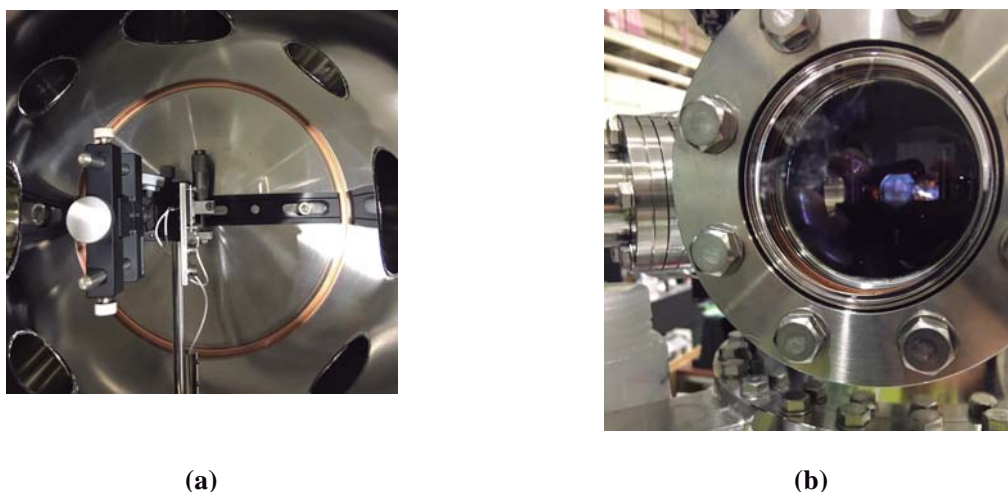


FIGURE 1. Photos of VUV-CPL irradiation experiment on BL1U using a vacuum chamber.
(a) Top view of the inside of the chamber. Sample folder fixed on the VUV CPL beam pass (left) and photon flux monitor mounted on a feed-through terminal (center).
(b) Snap shot of VUV CPL irradiation on the sample (amino-acid film on a quartz substrate).

REFERENCES

1. W. A. Bonner, *Orig. Life Evol. Biosph.* **21**, 407 (1991).
2. T. Fukue et al., *Orig. Life Evol. Biosph.* **40**, 335 (2010).
3. J. Takahashi et al., *Int. J. Mol. Sci.* **10**, 3044 (2009).
4. T. Fukuyama et al., *J Phys. Chem.* **A109**, 6928 (2005).
5. K. Matsuo et al., *UVSOR Activity Report 2016* **44**, 157 (2017).
6. J. Takahashi et al., *UVSOR Activity Report 2017* **45**, (2018).
7. F. Kaneko et al., *J. Phys. Soc. Jpn.* **78** 013001 (2009).

Investigation of the Structural Change during the Enzymatic Activation of a Prophenoloxidase by Vacuum-ultraviolet Electronic Circular-Dichroism Spectroscopy

Taro Masuda^a and Koichi Matsuo^b

^a *Laboratory of Food Quality Design and Development, Division of Agronomy and Horticultural Science, Graduate School of Agriculture, Kyoto University, Gokasho, Uji, Kyoto 611-0011, Japan*

Tel./Fax: +81 774 38 3765

E-mail: masutaro@kais.kyoto-u.ac.jp

^b *Hiroshima Synchrotron Radiation Center, Hiroshima University, 2-313 Kagamiyama, Higashi-Hiroshima 739-0046, Japan.*

Tel.: +81 82 424 6293; Fax: +81 82 424 6294; E-mail:

pika@hiroshima-u.ac.jp

Keywords: prophenoloxidase, copper protein, activation

Phenoloxidases (POs) play a crucial role in melanization of crustaceans. This class of enzymes catalyzes the hydroxylation of monophenols to o-diphenols (monophenolase activity; E.C. 1.14.18.1) and the subsequent oxidation to corresponding quinones (diphenolase activity; E.C. 1.10.3.1). Both POs and tyrosinases are classified as members of the "type 3 copper protein" family that is characterized by a reaction center containing two copper atoms, each of which is coordinated by side chains of three coordinated histidine ligands. Because PO produces a harmful intermediate in its catalytic reaction, the activation of PO must be tightly regulated [1]. Actually, PO is synthesized as an inactive pro-enzyme (prophenoloxidase, proPO) that is activated by some process [2]. ProPO also can be activated in vitro by adding low concentration of detergents or proteases. However, the structural basis of the activation process is unknown. In order to investigate the structural change during the activation, we compared the CD spectra of inactive proPO (woSDS) and activated PO (wSDS), which was activated by low concentration of SDS.

ProPO was purified from the homolymph of the kuruma prawn [3]. The active form of PO was obtained by the treatment with 0.01% SDS. The concentrations of inactive and active form of PO were adjusted to 50 μ M, before being scanned by vacuum-ultraviolet electronic circular-dichroism spectroscopy at BL12 in HiSOR.

The CD spectra of inactive proPO (woSDS) and activated PO (wPO) are shown in Fig. 1. These spectra were basically very similar each other. Fig. 2 shows the deduced secondary structure of these proteins from the CD spectra. These results suggest that partial structural changes were observed in some places, though the overall structure was not basically affected by the SDS treatment. We have a high-resolution X-ray crystal structure of this protein [4]. Accordingly, we are investigating the effects of the transition of the secondary structure on the structure of proPO, especially the structure adjacent to the active site.

Structural Changes of Histone Core Proteins by Chromatin Remodeling in DNA Damage Response of *Arabidopsis thaliana*

Jin-Hong Kim^{a,*}, Tae Ho Ryu^a, and Yudai Izumi^b

^aAdvanced Radiation Technology Institute, Korea Atomic Energy Research Institute, 29 Geumgu-gil, Jeongeup-si, Jeollabuk-do 56212, Republic of Korea

^bHiroshima Synchrotron Radiation Center, Hiroshima University, 2-313 Kagamiyama, Higashi-Hiroshima, Hiroshima 739-0046, Japan

Keywords: histone structure, chromatin remodeling, DNA damage response, *Arabidopsis thaliana*, circular dichroism.

Switch/sucrose non-fermenting (SWI/SNF) chromatin remodeling proteins play essential roles in diverse biological processes including DNA repair and apoptosis [1]. The Defective in RNA-directed DNA methylation (DRD) 1 is a plant-specific SWI2/SNF2-like chromatin-remodeling protein, which is necessary for DNA methylation and heterochromatin maintenance in *Arabidopsis thaliana* [2, 3]. We found that the *drd1-6* mutant, which has a defect in the helicase domain of DRD1, is more sensitive than the wild-type in response to gamma radiation. However, this phenomenon was not observed in the *drd1-p* mutant, a DRD1 knockdown mutant. Therefore, the structural analysis of chromatin in the *drd1-6* and *drd1-p* mutants will be important in elucidating the putative roles of DRD1-mediated chromatin remodeling in response to ionizing radiation. In this study, we aimed to elucidate the structural changes of core histone proteins in chromatin after gamma irradiation, which can be associated with the differential DNA damage responses in the wild-type, *drd1-p*, *drd1-6* and *DRD1 overexpression in drd1-6 (DRD1-OX/drd1-6)* lines.

The sterilized *A. thaliana* seeds were stratified at 4°C for 2 days and germinated in 1/2 MS medium supplied with 1% sucrose and 0.65% agar. The 14-day-old seedlings were exposed to gamma radiation with a dose of 200 Gy (50 Gy/hr) using a ⁶⁰Co source (42.6 TBq, AECL, Canada) at Korea Atomic Energy Research Institute) at room temperature. Core histone proteins were extracted using the Histone Purification Kit (Active Motif Inc., Carlsbad, CA) as described by Izumi *et al.* [4] with some modifications. The extracted proteins were lyophilized using a freeze dryer (FreezeMobile 25EL, SP Scientific, Warminster, PA) and stored at room temperature until use. For VUVCD analysis, the lyophilized samples were dissolved with 10 mM Tris-HCl and 250 mM NaF to induce higher-order structures of histone proteins.

The circular dichroism (CD) intensities obtained as ellipticity θ in millidegrees were converted to molar CD $\Delta\epsilon$ ($M^{-1} cm^{-1}$) to compare them. Molar CD is approximately described as

$$\Delta\epsilon = \frac{\theta MRW}{32980 c L}$$

where MRW, c , and L are residue weight, concentration of the sample (mg/ml), and path length (0.0050 cm), respectively. In this analysis, we defined MRW as follows.

$$MRW = \frac{2 * (14000 + 13900 + 15400 + 11400)}{2 * (129 + 125 + 135 + 102)} = 111.4.$$

In the WT, CD intensities of the positive peaks around 190 nm were higher in the irradiated (IR) sample than those of the unirradiated control one (Fig. 1a). However, such a difference in the CD spectra was not observed between the control and IR samples in the *drd1-p* and *drd1-6* mutants (Fig. 1b and c). In addition, the *drd1-6* and *DRD1-OX/drd1-6* mutants displayed a noticeable difference in the negative peaks between the control and IR samples (Fig. 1c and d).

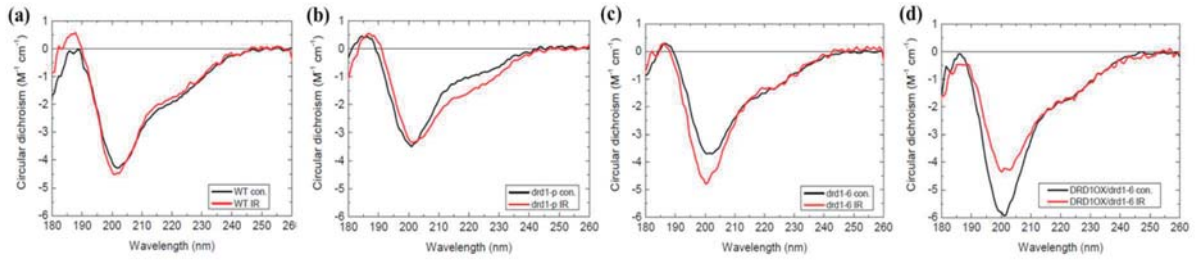


FIGURE 1. CD spectra of (a) WT, (b) *drd1-p*, (c) *drd1-6*, and (d) *DRD1-OX/drd1-6* in unirradiated control (black) and gamma-irradiated (red) plants.

The contents of secondary structures are listed in Table 1. The total α -helix and turn contents of core histone proteins in the irradiated samples were higher than those in the control ones. However, the total β -strand contents were not higher in the former than in the latter. In addition, the contents of unordered structures were different each other.

TABLE 1. Contents of secondary structures as obtained using the SELCON3 program. H(r), α -helix contents in regular region; H(d), α -helix contents in distorted region; S(r), β -strand contents in regular region; S(d), β -strand contents in distorted region; T, turn contents; U, unordered contents; and RMSD, RMSD between experimental and calculated CD. Unit: % without RMSD.

	H(r)	H(d)	S(r)	S(d)	T	U	SUM	RMSD
WT con	5.3	9.8	15.1	11.8	20.0	35.4	97.4	0.510
WT IR	7.6	10.8	11.4	10.4	22.7	36.5	99.5	0.547
<i>drd1-p</i> con	1.9	7.1	18.2	12.8	20.9	38.0	98.9	0.286
<i>drd1-p</i> IR	4.9	8.8	16.0	12.0	22.8	37.7	102.3	0.462
<i>drd1-6</i> con	3.8	10.1	17.0	12.2	21.2	36.7	101.1	0.348
<i>drd1-6</i> IR	4.9	9.2	11.4	11.4	22.6	43.2	102.6	0.434
<i>DRD-OX/drd1-6</i> con	3.6	9.1	13.9	12.6	20.6	39.7	99.5	0.335
<i>DRD-OX/drd1-6</i> IR	3.3	10.7	13.6	12.9	22.6	36.5	99.6	0.537

In conclusion, this study demonstrate that that gamma irradiation induces structural changes of core histone proteins in plants, partly depending on the presence of a SWI/SNF chromatin remodeling protein, DRD1. In the further study, the functional roles of IR-induced structural changes of core histone proteins will be explored in association with DNA damage response.

REFERENCES

1. J-H. Park, E-J. Park, S-K. Hur, S. Kim and J. Kwon, *DNA Repair*, Mammalian SWI/SNF chromatin remodeling complexes are required to prevent apoptosis after DNA damage, 2009, pp. 29-39.
2. T. Kanno, M. F. Mette, D. P. Kreil, W. Aufsatz, M. Matzke and A. J. Matzke, *Current biology*, Involvement of putative SNF2 chromatin remodeling protein DRD1 in RNA-directed DNA methylation, 2004, pp. 801-805.
3. T. Kanno, W. Aufsatz, E. Jalignot, M. F. Mette, M. Matzke and A. J. Matzke, *EMBO reports*, A SNF2-like protein facilitates dynamic control of DNA methylation, 2005, pp. 649–655.
4. Y. Izumi, K. Fujii, F. Wien, C. Hou  -L  vin, S. Lacombe, D. Salado-Leza, E. Porcel, R. Masoud, S. Yamamoto, M. R  fr  giers, M-A. H. du Penhoat and A. Yokoya, *Biophysical Journal*, Structure change from β -strand and turn to α -helix in histone H2A–H2B induced by DNA damage response, 2016, pp. 69-78.

Secondary Structural Analysis of Hyaluronan Synthase Interacted with Membrane by Vacuum-Ultraviolet Circular Dichroism Spectroscopy

Shoma Suenaga^a, Munehiro Kumashiro^a, Yudai Izumi^b, and Koichi Matsuo^b

^aDepartment of Physical Science, Graduate School of Science, Hiroshima University, 1-3-1 Kagamiyama, Higashi-Hiroshima, Hiroshima 739-8526, Japan

^bHiroshima Synchrotron Radiation Center, Hiroshima University, 2-313 Kagamiyama, Higashi-Hiroshima, Hiroshima 739-0046, Japan

Keywords: liposome, micelle, protein-membrane interaction, synchrotron-radiation circular-dichroism

The interaction between protein and bio-membrane is of great interest since such interactions occur in various biological events such as the drug delivery into cell and formation of amyloid fibrils. In the protein-membrane interaction studies, the phosphate lipids are widely used as the compositions of model membrane and these lipids can form liposome (lipid bilayer) and micelle (lipid monolayer) depending on the types of fatty acids (or tail groups). However, the contributions to the protein conformation due to the differences between bi- and mono-layers remain unclear. In this study, we measured the VUVCD spectra of hyaluronan synthase (HAS) from *Pasteurella multocida* [1] that is known as membrane-bound protein, under the presence of liposome and micelle, to characterize the conformations of the protein in the two types of membranes.

The VUVCD spectra of HAS at pH 6.8 and pH 4.5 from 260 to 175 nm are shown in Fig.1. The spectrum at pH6.8 exhibited two negative peaks around 210 and 220 nm, and a positive peak around 190 nm, suggesting that HAS forms helical rich structure at native state. The spectrum at pH 4.5 showed large decrement in the intensity but its shape was similar to that at pH 6.8. Liposome and micelle were produced from phosphatidylglycerol (PG) and lyso-phosphatidylglycerol (LPG), respectively. As shown in Fig.1, when adding PG to HAS solution at pH 4.5 (green line), the spectrum had a negative peak around 220 nm and a positive peak around 195 nm, which were similar characteristic peaks with those of β -strand-rich protein. When adding LPG (orange line), the spectrum showed two negative peaks around 220 and 208 nm and a positive peak around 190 nm, as observed at pH 6.8.

The secondary-structure contents were analyzed by SELCON3 program. The helical content of HAS slightly decreased under the PG liposome compared to that at pH 4.5 but it largely increased under the LPG micelle. To characterize the membrane-binding site of proteins, the secondary structure sequences and the transmembrane regions were predicted by VUVCD-NN method [2] and TMpred [3], respectively. As a result, it was expected that HAS had no interaction region in the liposome but two transmembrane regions in the micelle. These results show that the shapes of membrane largely affect the conformations of HAS. We will show the results of other proteins in the presentation.

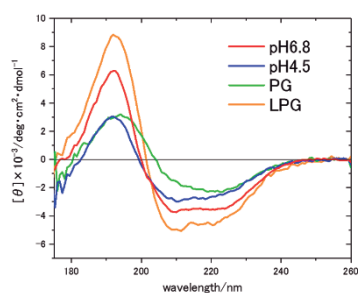


FIGURE 1. VUVCD spectra of HAS with and without membrane.

REFERENCES

1. W. Jing, P. L.DeAngelis, *Glycobiology*, **10**, 883 (2000).
2. K. Matsuo, K. Gekko, *Bull. Chem. Soc. Jpn.*, **6**, 675 (2012).
3. K. Hofmann, W. Stoffel *Biol. Chem.*, **374**, 166 (1993).

Vacuum-ultraviolet circular dichroism (VUVCD) for absolute configuration determination of chiral allenes

Tatsuo Nehira^a, Yugo Tokunaga^a, Taiki Umezawa^b, and Koichi Matsuo^c

^aGraduate School of Integrated Arts and Sciences, Hiroshima University,
1-7-1 Kagamiyama, Higashi-Hiroshima 739-8521, Japan

^bGraduate School of Environmental Science, Hokkaido University,
N10W5 Kita-ku Sapporo 060-0810, Japan

^cHiroshima Synchrotron Radiation Center Hiroshima University,
2-313 Kagamiyama, Higashi-Hiroshima 739-0046, Japan

Keywords: vacuum-ultraviolet electronic circular dichroism, ECD analysis, chiral allenes

Umezawa et al. achieved the total synthesis of a marine natural chiral allene “omaezallene” that shows an antifouling activity, establishing its absolute configuration [1]. The structure analysis required a lot of synthetic efforts and careful chirality assignments using appropriate empirical methods [2].

Based on the absorption bands of allenes, we expected that circular dichroism at the vacuum-ultraviolet region would be helpful for structure analysis of chiral allenes. In fact, vacuum-ultraviolet circular dichroism (VUVCD) [3] has afforded CD spectra down to 175 nm, where we observed characteristic Cotton bands of allenes, allowing clear-cut chirality assignment with the help of quantum mechanics CD calculation [4]. As is represented with **FIGURE 1**, VUVCD spectra from an enantiomeric pair of synthetic intermediates that satisfy the empirical methods were unambiguously predictable by theoretical calculations. This method of ours was valid for all the synthetic intermediates of omaezallene.

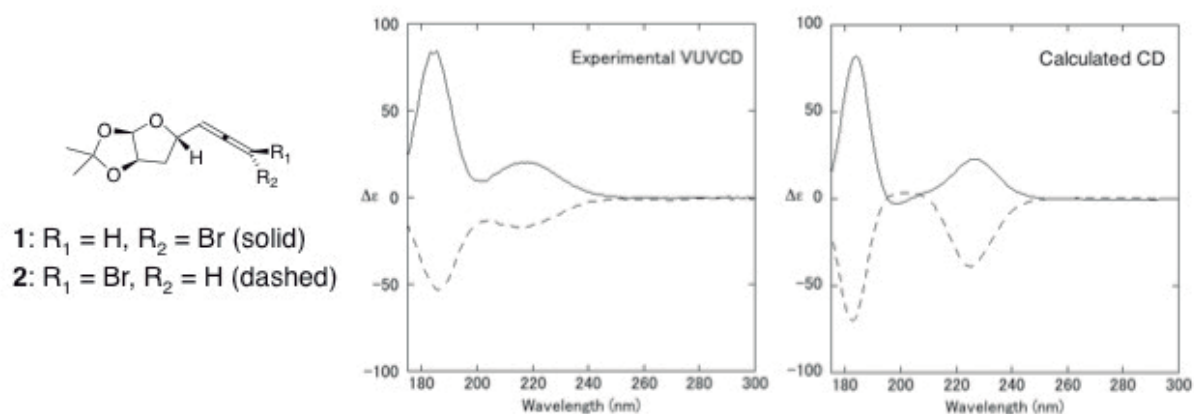


FIGURE 1. Synthetic intermediates **1** and **2**, structures (left), VUVCD (center), and calculated CD (right).

Therefore, absolute configurations of chiral allenes can be determined by combining experimental observation and theoretical prediction of VUVCD spectra. In order to generalize our approach, evaluation with a broader range of compounds is underway.

REFERENCES

1. T. Umezawa, Y. Oguri, H. Matsuura, S. Yamazaki, M. Suzuki, E. Yoshimura, T. Furuta, Y. Nogata, Y. Serisawa, K. Matsuyama-Serisawa, T. Abe, F. Matsuda, M. Suzuki, and T. Okino, *Angew. Chem. Int. Ed.* **53**, 3909-3912 (2014).
2. G. Lowe, *J. Chem. Soc. Chem. Commun.* 411-413 (1965).
3. K. Gekko and K. Matsuo, *Chirality* **18**, 329-334 (2006).
4. T. Nehira, Y. Tokunaga, T. Umezawa, and K. Matsuo, *HiSOR Activity Report*, 117 (2016).

Soft X-Ray Absorption Measurements for Thin Organic Materials by Means of Partial Electron and Fluorescence Detections at BL13

Shin-ichi Wada^{a,b}, Yoshitaka Taguchi^a, Yoshiki Iyobe^a, and Atsunari Hiraya^{a,b}

^aDepartment of Physical Science, Hiroshima University

^bHiroshima Synchrotron Radiation Center, Hiroshima University

Keywords: X-ray absorption spectroscopy (XAS), Total electron yield (TEY), Partial electron yield (PEY), Total fluorescence yield (TFY), Self-assembled monolayers (SAMs)

BL-13 is a soft X-ray beamline in HiSOR with a Dragon-type spherical grating monochromator [1]. The beamline has been devoted to investigate soft X-ray surface photochemistry and has kept a potential to measure X-ray absorption and photoelectron spectra especially for organic thin materials. X-ray absorption spectroscopy (XAS) is a great tool to investigate element-specific electronic states of samples. So far, XAS measurements at the end station of BL-13 has been provided with the total electron yield (TEY) mode simply by measuring sample drain current I_s . But in this method, the beamline need to be kept at organic contamination-free conditions of beamline optics and to prepare a clean I_0 monitor by deposition of fresh gold onto it. On the other hand, another convenient method to measure XAS is partial electron yield (PEY) detection, which has a great advantage to reduce huge background signal coming from sample substrates [2]. This detection method need to detect emitted electrons at a grazing emission direction from the surface. In this study, we prepared a newly built partial yield detector for organic thin materials at the end station of BL-13 and evaluated the detection system by using organic thin films and self-assembled monolayers (SAMs).

The detector was set just under a sample (a sample holder) and was also perpendicular to the X-ray propagation direction at the BL-13 end station. The partial yield detector is assembled using two high transmission metal grids and a microchannel plate (MCP) of large aperture. The first grid is kept at ground potential ($V_1 = 0$ V) and a negative voltage was operated to the second grid as a retardation voltage (V_2) to prevent detection of low-kinetic energy electrons. Typical retardation voltages V_2 were ~ -200 V for carbon and ~ -400 V for oxygen. The voltage of the front side of MCP (V_{MCP}) was 0 V in order to efficiently collect electrons. Samples used in this study are PMMA ($[-CH_2C(CH_3)(COOCH_3)-]_n$) polymer thin films (thickness ~ 500 Å) and methyl-ester terminated SAMs ($Au-S(CH_2)_{15}COOCH_3$, ~ 20 Å). SAMs were prepared by immersing Au substrates into 1.0 mM ethanol solutions of MHDA ($HS(CH_2)_{15}COOCH_3$).

Fig. 1 shows typical results of XAS spectra measured for O1s region of MHDA SAM by TEY and PEY detection modes. The PEY spectrum indicates clear improvement in spectral profile, as the TEY spectrum depicts depletion of intensity around first π^* peak and direct ionization region (above 545 eV) due to huge background signal of TEY detection method and therefore, reflecting contamination of the I_0 monitor. In order to simply

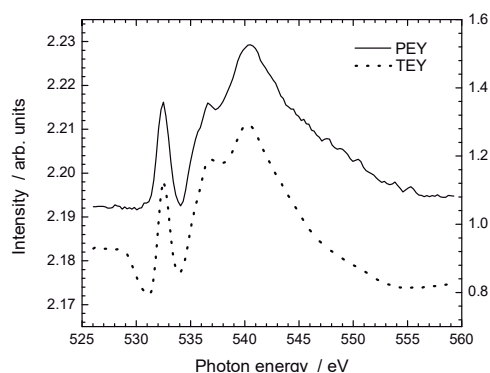


FIGURE 1. O1s XAS spectra of MHDA SAM measured by PEY (solid line) and TEY (dotted line) detection modes.

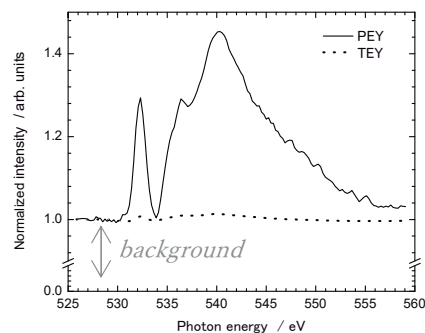


FIGURE 2. Simple comparison of S/B ratios on the O1s XAS spectra between PEY (solid line) and TEY (dotted line) detection modes measured for SAM.

compare the reduction of background signal by PEY mode, spectra are compared by normalizing each pre-edge intensity as shown in Fig. 2. In this situation, intensity from 0 to 1.0 is due to background components mainly coming from substrate gold and the intensity over 1.0 is XAS signal of the samples. It is clearly seen that the huge background measured for monolayer sample of MHDA by TEY mode is strongly reduced in the PEY mode, resulting in achieving the sample-sensitive detection. In order to clarify the retarding voltage dependence of such sample sensitivity, XAS spectra of MHDA SAM in PEY mode were measured by changing the retardation voltage V_2 from 0 to -600 V as shown in Fig. 3(a). Fig. 3(b) indicates signal to background (S/B) ratio at 541 eV depending on V_2 . The plot shows maximum ration at $V_2 = -400$ V, indicating that the retardation voltage around -400 V is suitable for high sample-sensitive measurement for oxygen region because of effective detection of oxygen Auger electrons.

The other potential of this partial yield detector for X-ray spectroscopy is also evaluated as show in Figs. 4 and 5. The dotted line in Fig. 4 is the plot of intensity at 541 eV depending on V_2 , and its differential intensity is also depicted as the solid line, corresponding to a convenient photoelectron spectroscopy (PES) spectrum which reflects inelastic low-energy electrons and carbon (~200 eV) and oxygen (~400 eV) KLL Auger components. On the other hand, by changing voltage setting to $V_2 = +100$ V and $V_{MCP} = -2$ kV to prevent ion (V_2) and electron (V_{MCP}) detection, the partial yield detector can detect (X-ray) fluorescence from the sample. Fig. 5 shows the typical result measured for PMMA in this voltage setting and therefore, indicates total fluorescence yield (TFY) spectrum of PMMA in O1s region. This measurement is also sensitive to thin sample as shown in improvement of S/B ratio.

REFERENCES

1. Homepage of Hiroshima Synchrotron Radiation Center, http://www.hsrc.hiroshima-u.ac.jp/english/storagering_beamlines/beamlines.html
2. J. Stöhr, *NEXAFS spectroscopy*, Berlin: Springer, 1992, pp. 118-133.

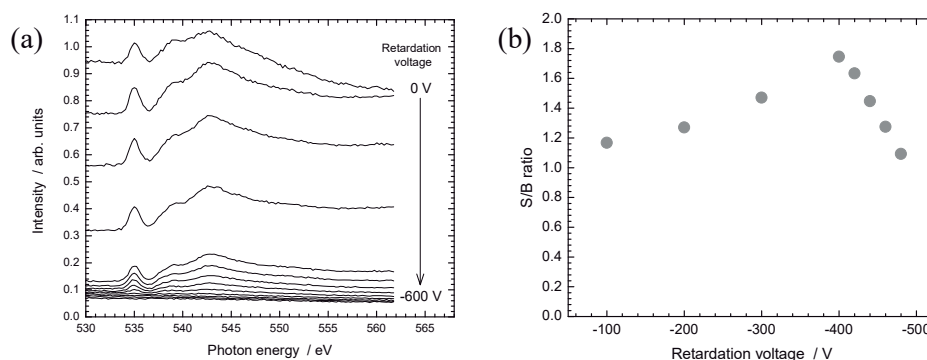


FIGURE 3. (a) Retardation voltage dependence of XAS spectra of SAM in PEY mode and (b) derived S/B ratio depending on the retardation voltage.

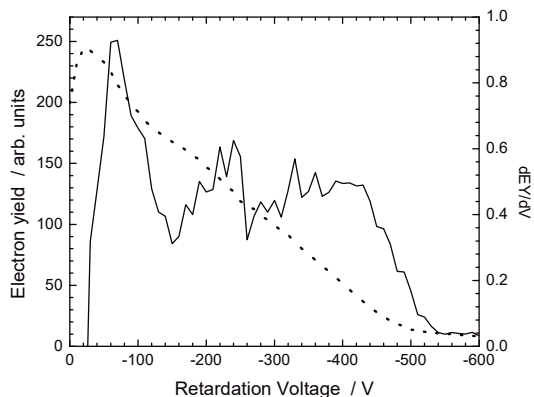


FIGURE 4. (dotted line) Retardation voltage dependence of PEY intensity for SAM and (solid line) its differential intensity, corresponding to convenient PES spectrum.

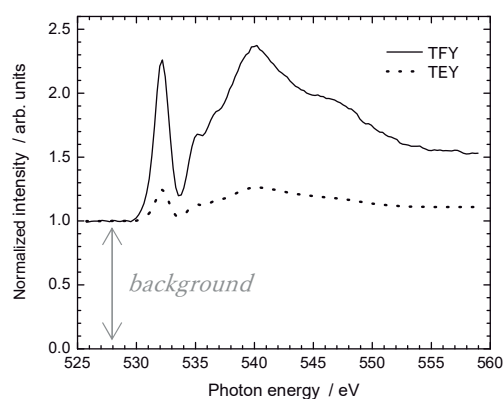


FIGURE 5. O1s XAS spectra of PMMA thin film measured by TFY (solid line) and TEY (dotted line) detection modes.

Magnetic state of Co layers intercalated into h-BN/Ni(111) studied by soft X-ray magnetic circular dichroism

Yuka Ohashi^a, Norikazu Ichikawa^b, Masahiro Sawada^c

^a*Department of Physical Science, Faculty of Science, Hiroshima University,
1-3-1 Kagamiyama, Higashi-Hiroshima, 739-8526, Japan*

^b*Department of Physical Science, Graduate school of science, Hiroshima University,
1-3-1 Kagamiyama, Higashi-Hiroshima, 739-8526, Japan*

^c*Hiroshima Synchrotron Radiation Center, Hiroshima University,
2-313 Kagamiyama, Higashi-Hiroshima, 739-0046, Japan*

Keywords: h-BN, cobalt, nickel ; X-ray magnetic circular dichroism

Tunnel magnetoresistance (TMR) effect is appeared on TMR structures which is composed of a nonmagnetic insulator layer inserted in two ferromagnetic metal layers. TMR effect has been used for developing devices such as magnetic random access memory, magnetic head for hard disk drives and high sensitive magnetic field sensor. MR ratio, one of important performance factors of a TMR device, is principally determined by spin polarization of the ferromagnetic layer at the interface. In order to develop high performance TMR devices, it is essentially important to examine magnetic state at an interface between a nonmagnetic insulator layer and a ferromagnetic metal layer. Atomically flat interfaces is also required to avoid coherence loss of a spin polarized electron wave transmitted through the insulating barrier layer. Hexagonal boron nitride (h-BN) is one of good candidates as insulating barrier layer, whose flat monolayer can be fabricated on some of fcc(111) metal surfaces. Intercalation effect of metallic atoms under the monolayer h-BN is also reported, which may enable us to obtain an ideal interface of h-BN/ferromagnet for TMR devices.

In this study, we made efforts to fabricate a layered sample of h-BN/Co/Ni(111) with a high quality interface of h-BN/Co under ultra-high vacuum condition. The intercalation of Co underneath h-BN was completed by post-annealing treatment after deposition of 0.5-7.2 ML Co onto h-BN/Ni(111), which was fabricated by thermal cracking of Borazine on the clean surface of Ni(111). We found out a proper condition of post-annealing to obtain h-BN/Co/Ni(111) with atomically flat interface, which was checked by means of Auger electron spectroscopy and low energy electron diffraction.

We examined magnetic state of h-BN/Co/Ni(111) and Co thickness dependence of local magnetic moments by soft X-ray magnetic circular dichroism experiments at Co $L_{2,3}$ and Ni $L_{2,3}$ absorption edges. Spin magnetic moment of Co was estimated from analysis of the XMCD spectra with magneto optical sum rule, and its thickness dependence was clearly observed. We have found that spins in the Co layer is antiferromagnetically aligned opposite to external magnetic field and magnetization of the Ni substrate in the thinnest region, whose spin direction turns to the field direction as Co thickness increases. The averaged magnetization is ferromagnetically saturated above 5 ML. The saturated value of spin-magnetic moment is estimated at $1.75 \pm 0.17 \mu_B$. This value is bigger than bulk value, $1.62 \mu_B$ [1]. From this result, the intercalated interface of h-BN/Co with 5 ML Co is concluded to be advantageous for TMR device application.

REFERENCES

1. C. T. Chen, Y. U. Idzerda, H.-J. Lin, N. V. Smith, G. Meigs, E. Chaban, G. H. Ho, E. Pellegrin, and F. Sette Phys. Rev. Lett., **75**, 152 (1995).

Antiferromagnetic Interlayer Coupling of Co/h-BN/Ni(111) Studied by Soft X-ray Magnetic Circular Dichroism

Norikazu Ichikawa^a, Yuka Ohashi^b, Masahiro Sawada^c,
Akio Kimura^a

^aDepartment of Physical Sciences, Graduate School of Science, Hiroshima University,
1-3-1 Kagamiyama, Higashi-Hiroshima, 739-8526, Japan

^bDepartment of Physical Sciences, Faculty of Science, Hiroshima University,
1-3-1 Kagamiyama, Higashi-Hiroshima, 739-8526, Japan

^cHiroshima Synchrotron Radiation Center, Hiroshima University,
2-313 Kagamiyama, Higashi-Hiroshima, 739-0046, Japan

Keywords: boron nitride, cobalt, nickel; X-ray magnetic circular dichroism

Tunnel magnetoresistance (TMR) is crucial for reading magnetic head in hard disk. Monolayer hexagonal boron nitride is an insulating layered material with stable honeycomb structure. It is expected to serve an ideal barrier layer in magnetic tunnel junction (MTJ). Spin-dependent transport studies with the MTJ incorporating a monolayer h-BN have shown the MR ratio up to 150% at room temperature [1, 2]. So far, magnetic state at the interface between a magnetic layer and a monolayer h-BN has not been sufficiently clarified, although it takes an essential role in a mechanism of TMR. We have previously reported antiferromagnetic coupling between the Co layer and Ni substrate via h-BN spacer layer [3]. As a next step, we have attempted to estimate the antiferromagnetic coupling energy and its Co thickness dependence from the element specific magnetization *v.s.* external magnetic field acquired by soft X-ray magnetic circular dichroism (XMCD).

We fabricated Co wedge film on h-BN/Ni(111) films for this purpose. High-quality h-BN was prepared on Ni(111) surface by cracking of vaporized borazine ($B_3N_3H_6$) [4]. The samples of Co/h-BN/Ni(111) are obtained by MBE evaporation of Co at room temperature. The XMCD experiments were *in-situ* performed at HiSOR-BL14 [5, 6]. Figure 1 shows the XMCD spectrum measured at room temperature at Co and Ni $L_{2,3}$ edges in normal incidence geometry under the external magnetic field of 1.1 T along sample normal direction. The Co magnetic moment is antiferromagnetically saturated below 2.3 ML whose direction is opposite to Ni spin and external magnetic field. As the Co film thickness is increased, the antiferromagnetic coupling is gradually released by increasing energy gain of ferromagnetic alignment parallel to the field. We estimated a quantitative value of the antiferromagnetic coupling energy between Ni and Co layers by analyzing Co thickness dependence of $M-H$ curves derived from field dependent XMCD signals.

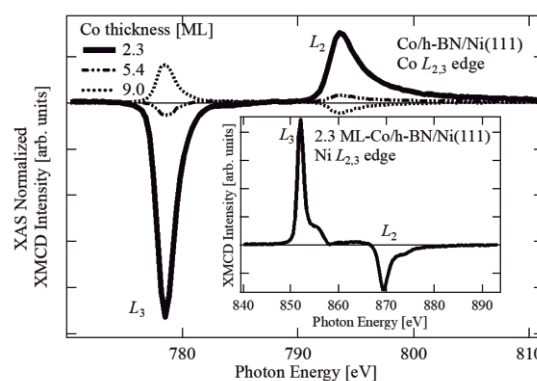


FIGURE 1. XMCD spectrum at Co $L_{2,3}$ edge and Ni $L_{2,3}$ edge in normal incidence geometry with magnetic field of 1.1 T along sample normal

REFERENCES

1. A. Dankert, M. V. Kamalakar, A. Wajid, R. S. Patel, and S. P. Dash, *Nano. Res.* **8**, 1357 (2015).
2. M. Piquemal-Banci, R. Galceran, S. Caneva, M. -B. Martin, R. S. Weatherup, P. R. Kidambi, K. Bouzehouane, S. Xavier, A. Anane, F. Petroff, A. Fert, J. Robertson, S. Hofmann, B. Dlubak, and P. Seneor, *Appl. Phys. Lett.* **108**, 102404 (2016).
3. N. Ichikawa, M. Sawada, K. Ishii, A. Kimura, *JPS. 2017 23pPAS-22*
4. C. Oshima and A. Nagashima, *J. Phys.: Condens. Matter* **9**, 1 (1997).
5. M. Sawada, K. Yaji, M. Nagira, A. Kimura, H. Namatame, M. Taniguchi, *AIP Conf. Proc.* **879**, 551 (2007).
6. M. Sawada, T. Ueno, T. Tagashira, H. Namatame, M. Taniguchi, *AIP Conf. Proc.* **1234**, 939 (2010).

X-ray magnetic circular dichroism study of $\text{Eu}_2\text{Ti}_2\text{O}_7$ and hybrid $\text{Eu}_{2-x}\text{TM}_x\text{Ti}_2\text{O}_7$ Pyrochlore

Arkadeb Pal^a, Shiv Kumar^b, Eike F. Schwier^b, Masahiro Sawada^b, Kenya Shimada^b, Anup K. Ghosh^c and Sandip Chatterjee^a

^aDepartment of Physics, Indian Institute of Technology (BHU), Varanasi-221005, India

^bHiroshima Synchrotron Radiation Center, Hiroshima University, Higashi-Hiroshima 739-0046, Japan

^cDepartment of Physics, Banaras Hindu University, Varanasi-221005, India

Keywords: Pyrochlore oxide, electronic structure, spin relaxation, XMCD.

The study of geometrically frustrated pyrochlore materials has received much attention due to its variety of low-temperature ground states which is associated to the geometry of the spin-lattice leading to frustration among the local spin interactions [1-3]. However, the geometrical spin frustration occurs when the spatial positions of the magnetic spins in a material and its local near neighbour spin-spin interactions hinders the formation of an ordered collinear ground state at very low temperatures. As a consequence of frustration, the spins cannot attain a long-range order at low temperature but freeze in a random manner or remain dynamic down to lowest possible temperatures giving rise to exotic ground states. These special low-temperature states include spin liquid states [4-6], apparent spin-glass-like states [7], spin ice state [8] and a state known as order by disorder [9] etc.

High quality polycrystalline $\text{Eu}_{2-x}\text{Fe}_x\text{Ti}_2\text{O}_7$ (with $x=0.0$, $x=0.1$ and 0.2) samples were synthesized using conventional solid-state reaction techniques. X-ray powder diffraction measurements confirm the prepared samples are of single phase with no chemical phase impurity. We have carried out XAS and XMCD measurements with polarized X-rays at the BL-14 beamline.

Figure 1(a) shows Fe $2p$ XAS spectrum corresponding to the photo-absorption from Fe $2p$ core level to the Fe $3d$ unoccupied states. The Fe $2p$ XAS spectrum consists of two peaks $\text{Fe}L_3(2p_{3/2})$ and $\text{Fe}L_2(2p_{1/2})$ at ~ 710 eV and ~ 724 eV, respectively, which is separated due to the spin-orbit interaction ($\Delta E \sim 14$ eV). We have observed a small but distinct crystal field splitting in the t_{2g} peaks of both $\text{Fe}L_3$ and $\text{Fe}L_2$ are discernible which indicates localized nature of Fe $3d$ electrons. Figure 2(b) shows the XMCD spectra at $\text{Fe}L_{2,3}$ absorption edge which is obtained by taking the difference between XAS spectra under $+1$ T and -1 T magnetic fields. We could not observe the XMCD signals at room temperature, indicating the absence of magnetic ordering at room temperature.

Figure 2(c) shows the Eu $3d$ XAS spectrum at Eu $M_{4,5}$ edges at 300 K, which corresponds to the dipole transition from Eu $3d$ core level to unoccupied Eu $4f$ state. Two peaks exist corresponding to the Eu $M_5(3d_{5/2} \rightarrow 4f)$ at ~ 1131.2 eV and Eu $M_4(3d_{3/2} \rightarrow 4f)$ at ~ 1158.9 eV, which are separated by the spin-orbit interaction (energy $\Delta E \sim 27.7$ eV). The Eu $3d$ XAS spectra is similar to that of Eu_2O_3 , but different from that of EuO, confirming nominal valency of $3+$ for Eu ions in our sample. Note that while Eu^{3+} is non-magnetic in its 7F_0 ground state, its subsequent excited states ${}^7F_{1,2,3}$ are magnetic [10], leading to appreciable magnetic behaviour.

Figure 2(d) depicts the Ti $2p$ XAS spectrum of EFTO at Ti $L_{2,3}$ edges at 300 K. The Ti $2p$ XAS spectrum is associated to the transition of electrons from Ti $2p$ to Ti $3d$ states. By comparing the line shape and energy separation between the obtained peaks of Ti $2p$ XAS spectra in EFTO with previously reported Ti $2p$ XAS spectra for TiO_2 , Ti_2O_3 , BaTiO_3 , SrTiO_3 the observed spectrum for EFTO accords with those of TiO_2 , SrTiO_3 , BaTiO_3 suggesting nominal oxidation state is Ti^{4+} [11]. The four-peak structure of the observed spectra is a common feature for all tetravalent Ti-based compounds with TiO_6 coordination, e.g. TiO_2 , SrTiO_3 , and BaTiO_3 . It is relevant to mention here that the L_3-e_g splitting into $d_{x^2-y^2}$ and d_{z^2} doublet for EFTO similar to that of TiO_2 , unlike SrTiO_3 or BaTiO_3 in which Ti is in perfect O_h symmetry [11]. The L_3-e_g splitting is about $\Delta E \sim 0.85$ eV for EFTO while it is ~ 1.2 eV for TiO_2 . It is in turn suggesting a smaller distortion from

the perfect O_h symmetry for EFTO. However, this explanation of e_g splitting still remains under debate because the distortion effect is too weak to produce significant e_g splitting. Later, P. Krüger claimed the e_g splitting is not due to a local structure effects, but rather arises due to a long-range band structure effect [12].

In summary, we have synthesized and characterized the pyrochlore compound of $\text{Eu}_{2-x}\text{Fe}_x\text{Ti}_2\text{O}_7$ with partial substitution of Fe on Eu site. Electronic structure of $\text{Eu}_{2-x}\text{Fe}_x\text{Ti}_2\text{O}_7$ has been investigated using XAS measurements. The analysis confirmed nominal oxidation states to be Eu^{3+} , Fe^{3+} and Ti^{4+} . Clear splitting of $L3-e_g$ peak of Ti 2p XAS spectra can be attributed to the deviation from pure O_h symmetry in Ti octahedral coordination in EFTO which was also evident from the X-ray diffraction analysis as it showed sizeable distortion present in the TiO_6 octahedra.

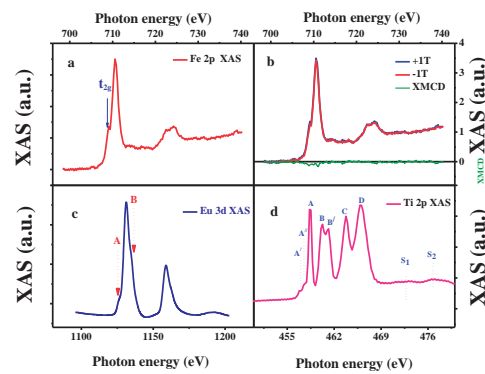


FIGURE 1: (a) Fe 2p XAS spectra at $L_{2,3}$ edges recorded at 300K. (b) Fe 2p XAS under ± 1 T fields and the corresponding XMCD is shown in bottom panel. (c) Eu 3d XAS spectra at M4-5 edges at 300K. (d) Ti 2p XAS spectra at $L_{2,3}$ edges at 300 K.

REFERENCES

1. J. S. Gardner, M. J. P. Gingras and J. E. Greedan, *Rev. Mod. Phys.* **82**, 53 (2010).
2. C. Castelnovo, R. Moessner and S L Sondhi, *Nature* **451**, 42 (2008).
3. S. T. Bramwell, M. J. P. Gingras, *Science* **294**, 1495 (2001).
4. Y. K. Tsui, C. A. Burns, J. Snyder and P. Schiffer, *Phys. Rev. Lett.* **82**, 3532 (1999).
5. L. Balents, *Nature* **464**, 199 (2010).
6. T. Taniguchi, H. Kadowaki, H. Takatsu, B. Fak, J. Ollivier, T. Yamazaki, T. J. Sato, H. Yoshizawa, Y. Shimura and T. Sakakibara, T. Hong, K. Goto, L. R. Yaraskavitch, and J. B. Kycia, *Phys. Rev. B* **87**, 060408 (2013).
7. G. Ehlers, J. E. Greedan, J. R. Stewart, K. C. Rule, P. Fouquet, A. L. Cornelius, C. Adriano, G. Pagliuso, Y. Qiu and J. S. Gardner, *Phys. Rev. B* **81**, 224405 (2010).
8. A. P. Ramirez, A. Hayashi, R. J. Cava, R. Siddharthan and B. S. Shastry, *Nature* **399**, 333 (1999).
9. J. Oitmaa, R. R. P. Singh, B. Javanparast, A. G. R. Day, B. V. Bagheri, and M. J. P. Gingras, *Phys. Rev. B* **88**, 220404 (2013).
10. V. Kachkanov, M. J. Wallace, G. van der Laan, S. S. Dhesi, S. A. Cavill, Y. Fujiwara and K. P. O'Donnell, *Sci. Rep.* **2**, 969 (2012).
11. D. H. Kim, H. J. Lee, G. Kim, Y. S. Koo, J. H. Jung, H. J. Shin, J.-Y. Kim, and J.-S. Kang, *Phys. Rev. B* **79**, 033402 (2009).
12. P. Krüger, *Phys. Rev. B* **81**, 125121 (2010).

XAS, XMCD and ARPES Studies of Co and Co₄₀Fe₄₀B₂₀ Ultrathin Films on Bi₂Te₃ for Spintronic Applications

Andrey K. Kaveev^a, Nikita S. Zhiltsov^a and Masahiro Sawada^b

^a*Toffe Institute, 194021, 26 Polytechnicheskaya str., Saint-Petersburg, Russia*

^b*Hiroshima University, 739-8527, Higashi Hiroshima, Japan*

Keywords: CoFeB, Laser Molecular Beam Epitaxy, Spin, Orbital magnetic moment, Magnetic hysteresis, Topological insulator

For the last years pronounced interest in spintronics area is related to the interesting class of the materials – topological insulators. These materials possess insulating properties in a bulk, having their surface conductive, owing to a strong spin-orbital interaction. Spin-orbital interaction leads to spin splitting of the surface states. These states form Dirac cone near Γ point [1].

Studies of the interface properties of a ferromagnetic metal grown on a ferromagnetic insulator are winning owing to the magnetic proximity effect, which breaks symmetry of the system relative to the time inversion of topological states. This effect is related to the ferromagnetic exchange field influence on the surface states of topological insulator. One may observe the reciprocal effect. The effect is related to the causing the magnetic order in ferromagnets by spin-polarized current flow through the topological states of a topological insulator. An idea of the mutual tunable influence of the topological interfacial states and magnetization on each other is attractive for the development of a novel spintronic devices based on the magneto-resistive systems and spin transistors [2, 3].

We have grown and studied Co and Co₄₀Fe₄₀B₂₀ (CoFeB in text) nanofilms using the Bi₂Te₃(0001) substrates. These films were grown with use of laser MBE system (produced by Surface, GmbH.) based on KrF₆ excimer laser. The film thickness was in the 1-20 nm range. Clear surface of Bi₂Te₃ substrates was obtained using adhesive tape to eliminate top layer of the material. To dehydrate the surface, Bi₂Te₃ substrates were annealed under 10⁻⁸ mBar pressure at 200°C during 30 minutes. The Co and CoFeB layers were grown on the Bi₂Te₃ substrate in 200-400°C temperature range. RHEED analysis was performed in-situ with use of built-in diffractometer at 30 kV. We have carried out an image analysis via special software developed in our group [4]. The software allows one to plot 3D projections of RHEED patterns in the reciprocal space for concrete zone axis. AFM measurements were realized with the microscope produced by NT-MDT (Zelenograd, Russia).

The results of XAS and XMCD measurements (BL14 beamline at HiSOR) of CoFeB/Bi₂Te₃ heterostructures are shown in Fig. 1. Shown in this figure is the Co 2p (a) and Fe 2p (b) $L_{3,2}$ fine structure of 5 nm thick CoFeB/Bi₂Te₃ grown at RT. The shapes of the spectra correspond to the metallic Co state in these layers [18]. The Fe state represents the superposition of metallic and oxidized Fe (Fe₂O₃ - type). For the case of CoFeB/Bi₂Te₃ the angular dependence of the XMCD signal was measured. In Fig. 2 the dependence of the XMCD signals normalized to the L_3 peak height on the photon energy for different beam incident angles θ is shown for Co (left) and Fe (right). It is seen that the value of the area of XMCD L_2 peak ΔA_{L_2} increases with θ increase. This fact confirms that the values of calculated experimental effective spin and orbital moment values definitely depend on the θ value. The values of m_s and m_{orb} were calculated using original software for Co and Fe in both Co/Bi₂Te₃ and CoFeB/Bi₂Te₃ cases (the results for the CoFeB films are summarized in Table 1). The software was developed by the authors of the work. Characteristic values of m_s and m_{orb} are relatively close to that for bulk (1.98 and 0.07 for Fe, and 1.55 and 0.15 for Co, resp.) [5]. Small deviation may be attributed to the oxidation of the samples and dimensional effects. It is seen that the directions of m_{orb} of Co and Fe are almost

perpendicular to each other.

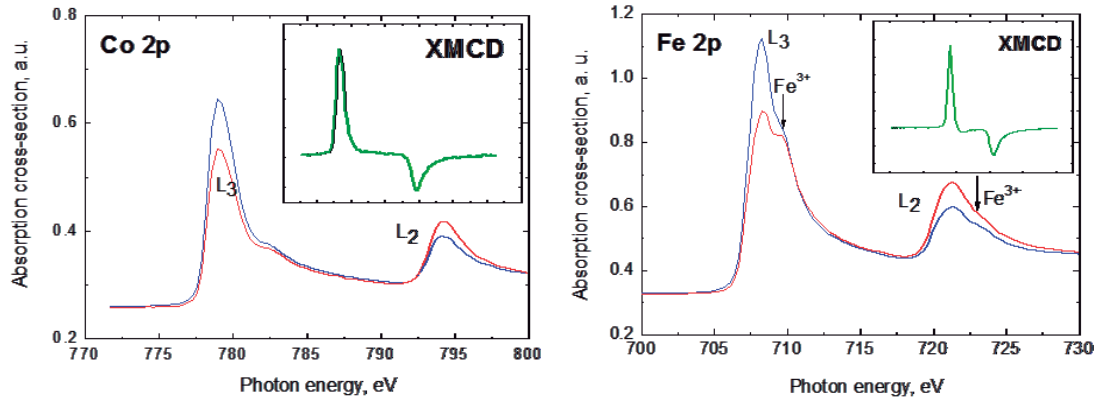


FIGURE 1. Co 2p (left) and Fe 2p (right) $L_{3,2}$ fine structures of 5 nm thick CoFeB/Bi₂Te₃ for the opposite external field directions. XMCD signals are shown in the insets.

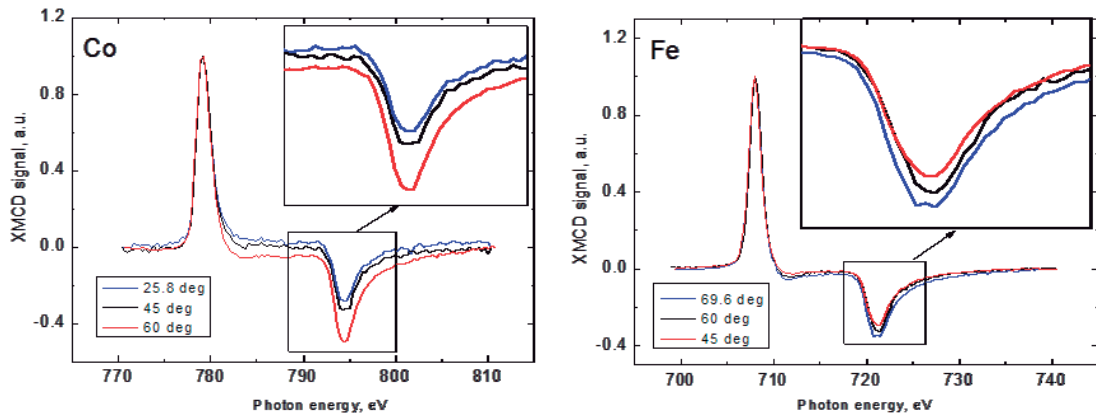


FIGURE 2. The dependence of the XMCD signal of Co (left) and Fe (right) on the θ angle in CoFeB/Bi₂Te₃ nanostructure. The spectra are normalized to L_3 peak height.

TABLE 1. Calculated values of spin and orbital moments (including the in- plane and out-of-plane components of m_{orb}) of Co and Fe in CoFeB for CoFeB/Bi₂Te₃.

CoFeB/Bi ₂ Te ₃		
	Fe	Co
m_s	1.88±0.10	1.22±0.05
m_{orb}	0.17±0.03	0.20±0.03
$ m_{orb }$	0.05	0.17
$ m_{orb}\perp $	0.13	0.05

Some preliminary ARPES measurements of Co grown on Bi₂Te₃ were carried out using Laser ARPES setup. It was shown that optimal thickness of Co to see dispersion is about 0.1-0.2 Å. These experiments are planned to continue in next beamtime. This work has been supported by Russian Foundation for Basic Research (grant № 17-02-00729). Part of the work was carried out using Hiroshima Synchrotron radiation center.

REFERENCES

1. J. Sanchez-Barriga, et al., *Nature Comm.*, **7**, 10559, (2016).
2. M. Vergniory et al., *JETP Lett.*, **95**, 4, 213, (2012).
3. P. Hai et al., *Nature Lett.*, **458**, 489, (2009).
4. S. Sutorin et al., *J. Appl. Cryst.*, **49**, 5, 1532, (2016).
5. J. Meyer et al., *J. Chem. Phys.*, **143**, 104302, (2015).

XMCD Study of Mn-doped Topological Insulators

A.V. Koroleva^a, D. Estyunin^a, A.M. Shikin^a,

M. Sawada^b, A. Kimura^{b,c}

^a*Saint Petersburg State University, 198504 Saint Petersburg, Russia*

^b*Hiroshima Synchrotron Radiation Center, University of Hiroshima, Higashi-Hiroshima 739-0047, Japan*

^c*Graduate School of Science, Hiroshima University, Higashi-Hiroshima 739-8526, Japan*

Keywords: Topological Insulators, XMCD, Magnetic properties.

It is well known that magnetically-doped topological insulators are characterized by unique electronic and magnetic properties allowing a realization of the quantum anomalous Hall effect (QAHE) [1,2]. For expanding the QAHE on higher temperature region a detailed study of magnetic coupling, its temperature dependence and relation to the features of electronic structure is demanded.

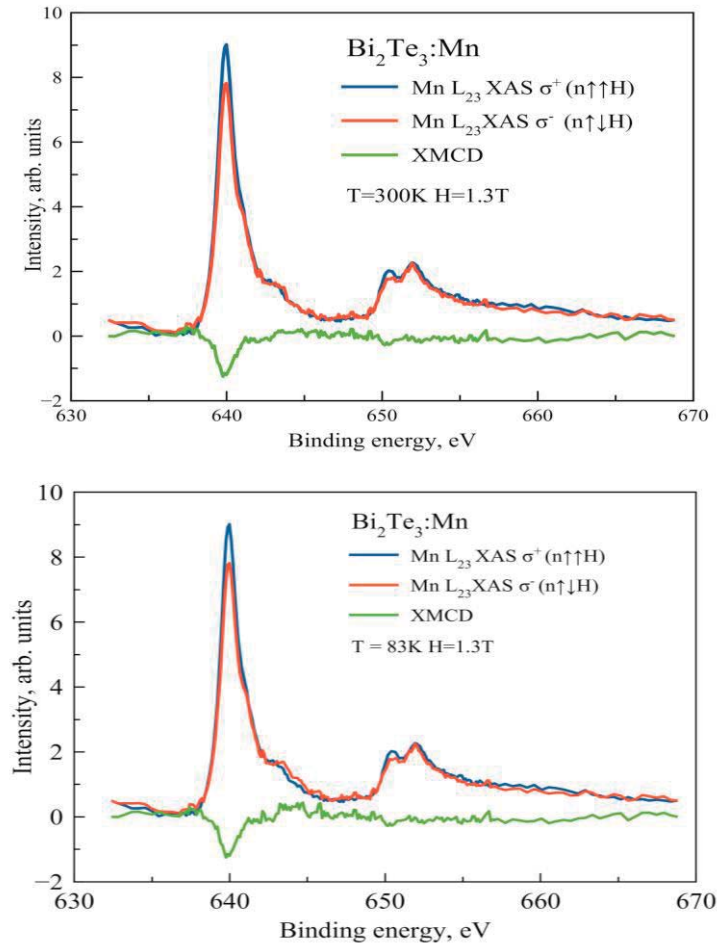


Fig.1 XAS spectra measured for Mn-doped Bi_2Te_3 at Mn $L_{2,3}$ edge at 83K – (a) and room temperature – (b) under photoexcitation by circularly polarized SR with magnetic field of opposite orientation applied perpendicular to the surface (red and black lines) and corresponding difference XMCD signal (green lines).

It is interesting that measurements of ARPES dispersion maps for Mn-doped TIs show often a splitting of the Dirac cone states at the Dirac point at temperatures above than the bulk Curie temperature that can be related to higher surface Curie temperature [3] and corresponding surface ferromagnetism. The surface-sensitive XMCD measurement for magnetically-doped TIs (see, for instance, Refs [4-6]) confirms an availability of a weak, but distinguishable surface magnetic moment up to temperatures 200-250K. It is assumed [6,7] that the coupling between ferromagnetic impurity atoms takes place via spin-dependent hybridization with the Te(p) states. Because chemical bonding and corresponding hybridization is not significantly influenced by temperature, this kind of the surface magnetic ordering is assumed be maintained up to higher temperatures

The current work is devoted to study of magnetic properties of Mn-doped Bi₂Te₃ measured at liquid nitrogen and room temperature by analysis of the XMCD signal at Mn L_{2,3} edge by XAS at BL-14.

Fig. 1 shows the results of measurements of magnetic moments developed at the Mn-ions in Mn-doped Bi₂Te₃ at liquid nitrogen (83K) and room temperatures, i.e. significantly above the bulk Curie temperature expected for such kind compounds. The magnetic moments were measured by XAS at Mn L_{2,3} edge under photoexcitation by circularly polarized SR with magnetic field of opposite orientation applied perpendicular to the surface that is an analog of corresponding XMCD measurements under photoexcitation by SR of opposite chirality

Our results show a visible XMCD signal at Mn L_{2,3} edge developed in Mn-doped Bi₂Te₃ both at 83K and room temperature testifying to the out-of-plane magnetization of Mn-ions even at room temperature than can be related to the spin-dependent d-p hybridization and its weak dependence on temperature.

REFERENCES

1. C.-Z. Chang et al., *Science* 340, 167-1702 (2013)
2. S. Qi et al., *Phys. Rev. Lett.* 117, 056804 (2016)
3. G. Rosenberg and M. Franz, *Phys. Rev. B* 85, 195119 (2012)
4. A.I. Figueroa et al., *Phys. Status Solidi RRL* 10, 467 (2016)
5. S.E. Harrison et al., *J. of Appl Phys* 115, 023904 (2014)
6. M.D. Watson et al., *New J Phys* 15, 103016 (2013)
7. M.F. Islam et al., *PRB* 87, 155429 (2018)

X-ray magnetic circular dichroism study of 0.7(BiFeO₃)-0.3(TbMnO₃) composite

Prince Gupta^a, Arkadeb Pal^a, Rahul Singh^a, Abhishek Singh^a, Shiv Kumar^b, Eike F. Schwier^b, Masahiro Sawada^b, Takeshi Matsumura^c Kenya Shimada^b, Anup K. Ghosh^d and Sandip Chatterjee^a

^aDepartment of Physics, Indian Institute of Technology (BHU), Varanasi-221005, India

^bHiroshima Synchrotron Radiation Center, Hiroshima University, Higashi-Hiroshima 739-0046, Japan

^cDepartment of Quantum Matter, Hiroshima University, Higashi-hiroshima, Hiroshima 739-8530, Japan

^dDepartment of Physics, Banaras Hindu University, Varanasi-221005, India

Keywords: Multiferroic, Exchange bias, XMCD.

In recent years BiFeO₃ (BFO) has emerged as one of the most significant materials for investigating the exchange bias phenomenon as well as multiferroicity. It is the only perovskite material (with $R3c$ space group) which shows multiferroic behavior at room temperature ($T_N \approx 643$ K and ferroelectric $T_C \approx 1100$ K). We have incorporated TbMnO₃ to synthesize a composite with BiFeO₃. As TbMnO₃ (TMO) is very promising material to induce strain in the system as it shows very strong magneto-electric coupling. Although TbMnO₃ possesses perovskite structure with a very close space group (space group $Pbnm$), the lattice mismatch between the two materials in the composite system is sufficient to create a strain the structure.

In this work, we have synthesized the hard and soft antiferromagnetic composite system of BiFeO₃ (70%) and TbMnO₃ (30%) using conventional solid-state reaction technique. X-ray powder diffraction measurements confirm the prepared samples are of single phase with no chemical phase impurity. We have carried out XAS and XMCD measurements with polarized X-rays at the BL-14 beamline. We have observed a large value of spontaneous exchange bias at room temperature and below room temperature. The origin of exchange bias in BiFeO₃ based systems has been an argued mechanism in recent years. In some BiFeO₃ based systems the exchange bias can only be found at lower temperatures and the EB phenomena has been linked with the super spin glass (SSG) moments. In order to understand this large value of the spontaneous exchange bias as well as the origin of ferromagnetism at low temperature we have done XMCD measurement to study the element specific magnetization of the sample.

In summary, we have synthesized and characterized the hard and soft antiferromagnetic composite system of BiFeO₃ (70%) and TbMnO₃ (30%). The role of interfacial exchange coupling in getting exchange bias in the system has been also confirmed by the training effect of the exchange bias and XMCD spectra of Fe and Mn L_{2,3} edge.

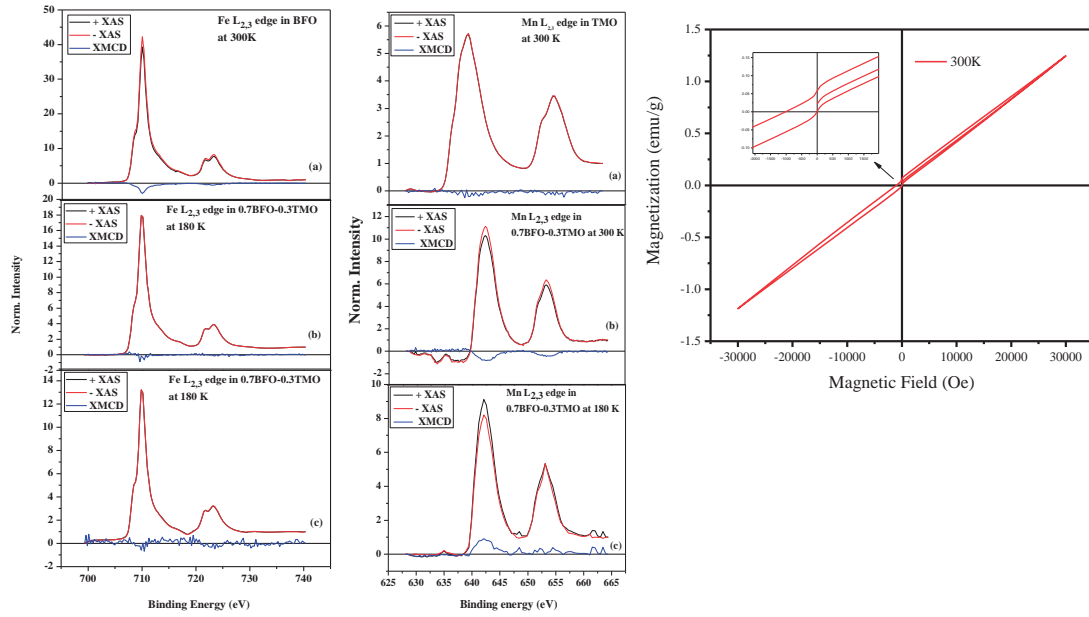


FIGURE 1: fig (A): XAS and XMCD spectra of Fe L_{2,3} edge in (a) BFO (b) 0.7BFO-0.3TMO at 300 K (c) 0.7BFO-0.3TMO at 180 K. Fig(B): XAS and XMCD spectra of Mn L_{2,3} edge in (a) TMO at 300 K (b) 0.7BFO-0.3TMO at 300 K (c) 0.7BFO-0.3TMO at 180 K. Fig (C) The hysteresis loop shift of 0.7BFO-0.3TMO composite measured at 300K.

REFERENCES

1. W. H. Meiklejohn and C. P. Bean, *Phys. Rev.* **102**, 1413 (1956)
2. J. Nogues and I. K. Schuller, *J. Magn. Magn. Mater.* **192**, 203 (1999).
3. J. Nogues, J. Sort, V. Langlais, V. Skumryev, S. Surinach, J. S. Munoz, and M. D. Baro, *Phys. Rep.* **422**, 65 (2005).
4. F. Radu and H. Zabel, in *Magnetic Heterostructures: Advances and Perspectives in Spin structures and Spin transport*, Ed. H. Zabel and S. D. Bader, Springer Tracts in Modern Physics (Springer-Verlag, Berlin, 2008), vol. 227, pp. 97–184.
5. S. Giri, M. Patra, and S. Majumdar, *J. Phys.: Condens. Matter.* **23**, 073201 (2011).

